



JÖNKÖPING UNIVERSITY
School of Engineering

INFLUENCE OF CARBON CONTENT AND COOLING CONDITIONS ON THE THERMAL CONDUCTIVITY AND TENSILE STRENGTH OF HIGH SILICON LAMELLAR GRAPHITE IRON

PAPER WITHIN: MATERIALS AND MANUFACTURING ENGINEERING

AUTHOR: GOKUL RAM AND VISHNU HARIKRISHNAN

TUTOR: BJÖRN DOMEIJ

JÖNKÖPING 2020

This master thesis work has been carried out at the School of Engineering in Jönköping in the subject area Materials and Manufacturing - Foundry Technology. This thesis work is a part of research project "Lean Cast" a collaboration between Jönköping University, Swedish Knowledge, Scania AB, Volvo Group Trucks technology AB, SinterCast AB, SKF Mekan AB

Examiner: Vasilios Fourlakidis

Supervisor: Björn Domeij

Scope: 30 Credits

Date: 2020-12-04

Abstract

Much study has been carried out to determine the properties of Lamellar Graphite Iron (LGI) or grey iron and their relations to factors such as the cooling rate, the dendrite morphology, the pouring temperature, and so on. However, there hasn't been much comprehensive study on the properties of LGI outside the generally used and accepted composition, with 1 to 3% Silicon. The scope of this study is to measure and evaluate the thermal conductivity and tensile strength of LGI, for a higher concentration of Si and different carbon contents. The concentration of Si aimed for was 4% but the concentration obtained after spectroscopy was between 4.1% to 4.15%. There are two hypereutectic, one near-eutectic and three hypoeutectic samples considered and these six chemical compositions were cast under different cooling conditions. The cooling time has been varied by providing different molds of 30mm, 55mm, and 80mm diameter cylinders respectively, for all the six sample compositions. The microstructure analysis carried out studies the segregation of Si, the graphite morphology, primary austenite morphology. These factors are then compared to the thermal and tensile behavior measured in this study. It can be observed that the thermal conductivity studied in the present work has a direct correlation for a higher Si content and tends to be greater than the thermal conductivity values observed from other studies with lower content of Si. However, the conductivity shows an inverse relation with the cooling rate and is maximum for the samples with the lowest cooling rate. The tensile strength, on the other hand, seems to have a lower value than that observed in previous studies for LGI with 1 to 3% Si, but shows a direct correlation with the cooling rate. The mean area fraction of dendrites obtained and the mean interdendritic hydraulic diameter is also measured and their influence on the properties are also studied. The addition of more Si has greatly favored the thermal behavior positively but has also reduced the tensile strength.

Summary

The report presented here is a part of the Master program in Product Development and Materials Engineering and is conducted at the Department of Materials and Manufacturing of Jönköping University, from January 2020 till November 2020. This work is also conducted within the research project “Lean Cast” a collaboration between Jönköping University, Swedish Knowledge Foundation, Scania CV AB, Volvo Group Trucks Technology AB, SinterCast AB and SKF Mekan AB.

The purpose of this research is to get a wider understanding of the thermal and tensile behavior of lamellar grey cast iron when the Si composition is increased from the usual concentration of 1 to 3% to a higher proportion of nearly 4%. But, the Si content in the present work was found to be between 4.1% to 4.15%. The study has been conducted over six sets of samples, each subjected to three different cooling conditions. The carbon contents for the six samples have been distributed over two hypereutectic, one near-eutectic, and three hypoeutectic compositions. As the Si content has been increased to 4%, the carbon content has been altered accordingly to achieve the desired carbon equivalent for each chemical composition. The effect of thermal conductivity and tensile strength on the Si content, the cooling rate, and the varied carbon contents have been broadly studied and discussed in this report.

To achieve this purpose, the samples have been cast at Jönköping University and were cooled at room temperature. Three different cooling conditions were achieved using 3D printed Silica sand molds of 30mm, 55mm, and 80mm inner diameter. The castings were then cut and machined to the desired specifications and dimensions required to carry out the thermophysical and tensile tests.

The tensile samples after fracture were subjected to color etching with a reagent based on picric acid for the microstructure analysis. A wide range of graphite morphologies was observed depending on the carbon content and the precipitation of the free graphite due to the increased carbon content. The hypereutectic samples had type A and type C flakes. The hypoeutectic ones had type D and type E morphologies. The Si segregation in the microstructure and its effect on the metal matrix and the graphite flakes has been studied. Moreover, the fraction of primary dendrites and the mean hydraulic diameter has been calculated after observing the micrographs for each chemical composition. The effect of cooling rate on the microstructure obtained and the behavior of the samples have also been observed.

The results show that the thermal conductivity has a direct relation with the Si content. The higher amount of Si ensured more precipitation of free graphite flakes in the melt, leading to enhanced thermal conductivity. Moreover, Si promoted ferritic growth, which also promotes thermal conductivity. The cooling rate, however, had an inverse effect on the thermal conductivity. Higher cooling rates ensured the presence of pearlite colonies which reduced the thermal behavior. The tensile properties were seen to improve with higher cooling rates and they have an inverse relation with higher Si.

Keywords

Lamellar cast iron; hypereutectic; eutectic; hypoeutectic; carbon; silicon; carbon equivalent; cooling rate; dendrites; graphite flakes; specific heat capacity; thermal expansion coefficient; thermal diffusivity; thermal conductivity; tensile strength; hydraulic diameter.

Contents

I	Introduction	11
1.1	BACKGROUND	11
1.2	PURPOSE AND RESEARCH QUESTIONS.....	11
1.3	DELIMITATIONS	12
1.4	OUTLINE	12
2	Theoretical background	13
2.1	INTRODUCTION TO CAST IRON.....	13
2.1.1	Allotropes of Pure Iron	13
2.1.2	Iron-Carbon Phase Diagram.....	14
2.1.3	Stable and Metastable System	15
2.1.4	Different phases in the Cast Iron Solidification	16
2.1.5	Carbon Equivalent	17
2.2	CLASSIFICATION OF CAST IRON.....	18
2.2.1	Classification Based on the Carbon equivalent.....	18
2.2.2	Classification Based on Graphite Morphology	18
2.3	SOLIDIFICATION OF CAST IRON.....	20
2.3.1	Solidification of Hypoeutectic Cast Iron	20
2.3.2	Solidification of Hypereutectic Cast Iron:	22
2.3.3	Factors Affecting Solidification	23
2.4	HEAT TRANSMISSION IN LAMELLAR CAST IRON	25
2.4.1	Thermal Conduction	25
2.4.2	Thermal Properties:	26
2.4.3	Influence of Microstructure on the Heat Conduction:	28
2.5	STATIC MECHANICAL PROPERTIES OF LAMELLAR GRAPHITE IRON	30
2.5.1	Tensile Strength.....	30
2.5.2	Hydraulic Diameter	32
3	Method and implementation	34
3.1	CASTING THE SAMPLES:	34
3.2	CUTTING OF THE SAMPLES:	38
3.3	MACHINED THERMAL SAMPLES:	40
3.4	THERMAL ANALYSIS:	41
3.4.1	Differential scanning calorimetry (DSC):	41

3.4.2 Dilatometer:	43
3.4.3 Laser Flash	45
3.5 MACHINED TENSILE SAMPLES:.....	47
3.6 TENSILE TESTS:	48
3.7 SAMPLE ETCHING:	50
3.7.1 Sample Mounting:	50
3.7.2 Grinding and Polishing:.....	51
3.7.3 The etchant used and Procedure for Etching:	53
3.8 MICROSTRUCTURAL ANALYSIS:	53
4 Findings and Analysis.....	55
4.1 THERMOPHYSICAL PROPERTIES	55
4.1.1 Specific Heat Capacity:	55
4.1.2 Thermal Expansion Coefficient:	57
4.1.3 Thermal Diffusivity:	58
4.1.4 Thermal Conductivity:	60
4.2 ULTIMATE TENSILE STRENGTH:	61
4.2.1 Tensile strength as a function of Carbon Equivalent:	62
4.2.2 Correlation between Tensile Strength and Hydraulic Diameter	63
4.3 COLOR ETCHED MICROGRAPH ANALYSIS.....	66
5 Discussion and conclusions	68
5.1 DISCUSSION OF THE METHOD:.....	68
5.2 DISCUSSION OF FINDINGS:.....	69
5.3 CONCLUSIONS AND FUTURE WORK.....	73
6 References	75
7 Appendices	79

List of Figures

Figure 1 Allotropes of pure iron [12]..... 14

Figure 2 Iron carbon phase diagram [13]..... 15

Figure 3: Graphite structure and growth direction [1] 17

Figure 4:(a) Lamellar Graphite Iron(LGI) and (b) Different orientations of graphite in LGI [15] 19

Figure 5: Compacted Graphite Iron (CGI) morphology [1] 19

Figure 6: Spheroidal Graphite Iron (SGI) morphology [15]..... 20

Figure 7:Solidification mechanism of hypoeutectic cast iron [23]..... 21

Figure 8: Curve showing the relation between Pouring temperature and the Eutectic cells formed [30]..... 24

Figure 9: Curve showing the thermal conductivity v/s temperature for Lamellar graphite iron, Compacted graphite iron, and Spheroidal graphite iron. [41] 29

Figure 10: thermal conductivity trends in cast irons..... 30

Figure 11 : Heat transmission in LGI and..... 30

Figure 12: Influence of graphite in tensile strength [46] 31

Figure 13: Effect of carbon equivalent on tensile strength [46] 32

Figure 14: Random distribution of dendrites in cubic domain [44]..... 33

Figure 15: Flowchart showing the method implemented in steps 34

Figure 16:(a) 30mm Silica sand mold drawing and (b) 30mm mold with the implemented pouring cup in the middle. 36

Figure 17: 55mm Silica sand mold drawing 37

Figure 18: 80mm Silica sand mold drawing 37

Figure 19: Casted samples for 4% by weight of Silicon..... 38

Figure 20: Cracks Generated in Molds 38

Figure 21: Harrison Model M390 Gap Bed Lathe used 39

Figure 22: Proline 320.280H semiautomatic bandsaw used to cut the cylinders for the thermal and tensile tests 39

Figure 23: separated cut parts of the same cylinder for the different tests 39

Figure 24: Porosities seen on the top section of the cylinder 40

Figure 25: Machined thermal sample 40

Figure 26: DSC, Dilatometer, and LF Samples For Thermal Test 41

Figure 27: DSc Netzch 404 C pegasus [49]..... 42

Figure 28: Differential Scanning Calorimetry set up to hold the sample [49]..... 42

Figure 29: General trend of the Specific heat curve of the samples, considering only the heating part of the curve. The curve observed here is of Si₄C₁, for 30mm diameter. The reference standard is sapphire with a weight of 42.5mg. 43

Figure 30: Principle of the Dilatometry [53] 44

Figure 31: Dilatometer 402 C 44

Figure 32: General trend of elongation v/s temperature of the samples. The scale of alpha (CTE) values is on the right axis. The curve observed here is of Si₄C₁, for 30mm diameter. The reference standard is Al₂O₃ with a length of 12.5mm. 45

Figure 33: Netzsch LFA 427 [15] 46

Figure 34: The Laser flash system and procedure [15]..... 47

Figure 35: Specifications of the Tensile sample 48

Figure 36: Machined Tensile sample 48

Figure 37: Nomenclature for an I shaped tensile sample..... 48

Figure 38: the Zwick/Roell Z100 Ultimate Tensile rig and the hydraulic grips to hold the sample 49

Figure 39: Sample after tensile testing..... 49

Figure 40: The groove wedge used to hold the samples in grip 50

Figure 41: Struers Citopress used to embed the specimen [61]..... 51

Figure 42: Mecapol P 310 VV apparatus used for the wet grinding 51

Figure 43: Struers Tegramin-30 used for the fine polishing [63] 52

Figure 44: steps used for the automated polishing in Struers Tegramin-30 52

Figure 45: The graphite flakes as seen after the grinding and polishing of the sample. The flakes are very visible and no cavities were seen because the flakes were not ripped off..... 53

Figure 46: The broken tensile sample after mounting, polishing, and etching. This is well etched as the hue of the film on top of the surface is blue. 53

Figure 47: (a) Micrograph obtained after color etching and (b) its corresponding binary image. The sample considered is Si₄C₆, for the 55mm diameter cast. 54

Figure 48: Specific heat capacity v/s temperature for highest cooling rate (30mm). Si₄C₁ follows the same trend as Si₄C₂ and is hidden behind the curve for Si₄C₂. ... 55

Figure 49: Specific heat capacity v/s temperature for moderate cooling rate (55mm). Si4C2, Si4C3 and Si4C4 follows the same trend and hence they overlap.56

Figure 50: Specific heat capacity v/s temperature for slow cooling rate (80mm). Si4C2, Si4C3, Si4C4, Si4C5 and Si4C6 seems to overlap each other.56

Figure 51: Thermal expansion coefficient v/s temperature for high cooling rate (30mm). All the curves are observed to be very close to each other or overlap, making it difficult to differentiate between each trend.57

Figure 52: Thermal expansion coefficient v/s temperature for medium cooling rate (55mm). All the curves are observed to be very close to each other or overlap, making it difficult to differentiate between each trend.57

Figure 53: Thermal expansion coefficient v/s temperature for slow cooling rate (80mm). All the curves are observed to be very close to each other or overlap, making it difficult to differentiate between each trend.58

Figure 54: Thermal diffusivity v/s Temperature for high cooling rate (30mm)58

Figure 55: Thermal diffusivity v/s Temperature for medium cooling rate (55mm)59

Figure 56: Thermal diffusivity v/s Temperature for slow cooling rate (80mm).....59

Figure 57: Thermal conductivity v/s temperature curve for high cooling rate (30mm)60

Figure 58: Thermal conductivity v/s temperature curve for medium cooling rate (55mm).....60

Figure 59: Thermal conductivity v/s temperature curve for slow cooling rate (80mm)61

Figure 60: Influence of carbon equivalent on tensile strength.....63

Figure 61: Hypereutectic composition of 30mm diameter (high cooling rate) with no dendrites observed64

Figure 62: Influence of Hydraulic diameter on tensile strength65

Figure 63: Color etched microstructure images of 30mm diameter (high cooling condition)66

Figure 64: Color etched microstructure images of 55mm diameter (Moderate cooling condition)67

Figure 65: Color etched microstructure images of 80mm diameter (lowest cooling condition)67

Figure 66: Graphite Lumps are seen in the melt during the casting68

Figure 67: the supports used in the UTS rig. (a) shows the aluminum sheet employed within the grips and (b) shows the 20kN load cell with the supportive grip employed to break the samples of low carbon contents.69

List of Tables

Table 1: The expected chemical compositions with different levels of carbon..... 35

Table 2: The observed chemical compositions after casting, with different levels of carbon..... 35

Table 3: Weights of each DSC sample for different cooling rates. All weights are in mg 43

Table 4: Lengths of each Dilatometer sample for different cooling rates. All lengths are in mm. 45

Table 5: Thickness of each Laser Flash sample for different cooling rates. All thicknesses are in mm 46

Table 6: The measured value of tensile strength for six different C.E and three different cooling conditions 62

Table 7: Measured hydraulic diameter and mean area fraction of dendrites for all six compositions at three different cooling conditions 64

Table 8: Measured values of hydraulic diameter and tensile strength for varying C.E at three different cooling conditions 65

Table 9: Comparison of tensile strengths obtained from the MTS and UTS for Si4C1 and Si4C5..... 69

1 Introduction

The present thesis work is carried out at the Department of Materials and Manufacturing in Jönköping University within the research project “Lean Cast” a collaboration between Jönköping University, Swedish Knowledge Foundation, Scania CV AB, Volvo Group Trucks Technology AB, SinterCast AB and SKF Mekan AB.

As part of the research project, the goal of this thesis is to understand the influence of carbon content and cooling conditions on the thermal conductivity, tensile strength and microstructure of a high silicon (4%) gray iron.

1.1 Background

Cast iron is one of the oldest metallic material that has been used by humans for over 2500 years [1], and it has numerous technological applications owing to its wide range of mechanical and thermal properties. One such industry which largely favors the use of cast iron in its component is the automotive industry where cast iron is used in the manufacturing of cylinder heads of engine blocks or piston rings, amongst many others [2].

All these components are subjected to high temperatures during its life cycle. These high temperatures can produce deformations in the material, which if critical could cause fractures. The most common component used for this purpose is Lamellar Grey Iron (LGI), which has been studied in this report. LGI has superior thermal conductivity compared to all other iron castings, owing to the flaky morphology of the graphite chunks present in the microstructure. Nonetheless, they have very poor tensile strength compared to Spheroidal graphite iron, where the graphite is more nodular. Compacted graphite Iron, however, is the best alternative as it has intermediate properties and structure [2].

This thesis work studies the thermal conductivity and tensile strength of lamellar grey iron for a higher percentage of Si, in context with previous literature which studies these properties for a general concentration of 1-3% Si [3], for a range of different carbon values. the usually observed thermal conductivity of LGI is between 40 W/(mK) and 52 W/(mK) [4] and the tensile strength is usually between 350 to 400 Mpa [5]. This work focuses on the influence of these different compositions on the microstructure and graphite morphologies obtained over three different cooling conditions.

1.2 Purpose and research questions

The main purpose of this thesis work is to explore the behavior of gray iron outside the conventional range of silicon concentration. In particular, the influence of a higher percentage of Silicon content (4%) on the Thermal conductivity, Tensile strength, and Microstructure under varying carbon content and cooling rates. With this purpose in mind, a few research questions can be formulated:

- What is the effect of a higher content of silicon on the microstructure of the studied alloy ?
- What is the effect of carbon content and microstructure on the thermal conductivity and the tensile strength of the studied alloy ?

- How does the high silicon content affect the thermal conductivity and the tensile strength of the lamellar cast iron ?
- What is the effect of cooling condition on the thermal conductivity and the tensile strength of the lamellar cast iron ?

1.3 Delimitations

There is a lot to study on this topic and delimitations are necessary to make feasible for a MSc thesis work. A few delimitations are mentioned below:

- The influence of Si could be clarified by systematically varying the Si concentration, but in the present work, we have focused only on 4% of Si. However, the results can be compared to earlier studies on lower concentrations of Si.
- The evaluation of tensile tests are focused on the ultimate tensile strength.
- Many microstructural features are valuable to study, but this work focuses on the dendritic austenite structure and graphite flake morphology.
- The influence of alloying elements other than C and Si on microstructure, thermal, and mechanical properties is investigated.
- Cooling curves were not recorded for the castings.

1.4 Outline

To make our work more understandable to the readers, we have divided our work of study into four parts.

- The first part contains the theoretical background, where it gives general information about the cast iron, its different types, solidification process, the type of matrix formed, influence of cooling rate, and compositions, mechanical and thermal properties of LGI.
- In the second part, the method and implementation are explained, here the reader will get to know about the method and the machines we used to carry out the different experiments.
- The third part discusses our findings and analysis of the experiments we have gone through
- Finally, the fourth part gives brief conclusions about the findings discussed in the findings and analysis.

2 Theoretical background

2.1 Introduction to Cast Iron

Cast iron refers to a family of ferrous alloys, which usually contain more than 2% carbon (C). The most important alloying element added is Silicon (Si), usually ranging from 1 to 3% [6]. The content of carbon differentiates cast iron from steel and the higher carbon leads to a more carbon-rich phase in cast irons [7]. Moreover, cast irons can achieve good fluidity, and prevent the development of any surface films while pouring, owing to the higher carbon and silicon contents [8]. The following properties make cast iron a better engineering material:

- It is produced by making simple improvisations in the chemical composition of the alloying elements added with the pig iron.
- Has good mechanical strength under compression.
- Easy machining when a suited chemical composition is selected.
- Has a good fluidity in the molten state, leading to a casting with less porosity and shrinkage.
- Special properties could be obtained by altering the chemical composition and heat treatment, e.g. spheroidal graphite irons are strong and the lamellar graphite irons have better thermal conductivity [9].

Cast iron can be classified into four types, depending upon the morphology of the graphite present in them:

- Grey or Lamellar Cast Iron (flaky graphite formation)
- Ductile or Spheroidal or Nodular cast iron (graphite forms spheres)
- Compacted Graphite Iron (coral-like formations of graphite, with both spheres and vermicular graphite)
- White Cast Iron (where carbon solidifies as metastable cementite and not graphite) [10].

2.1.1 Allotropes of Pure Iron

Depending upon the temperature, at the atmospheric pressure, metals can exist in numerous crystallographic forms, a phenomenon named as Allotropy [11]. Cast iron has three allotropes, formed under equilibrium cooling conditions, which are as follows:

- The solidification of pure, liquid iron starts at the temperature of 1540 °C forming Delta iron (δ_{Fe}), which has a bcc structure. This allotrope is quite unstable but its presence can be seen down to a temperature of 1395⁰C [11].
- At this temperature (1395⁰C), δ_{Fe} transforms an fcc structured crystal lattice. This allotrope of iron is the gamma iron, also called Austenite(γ_{Fe}) [11].

- On further cooling to a temperature of 900°C, the γ_{Fe} undergoes yet another transformation to ferrite iron, also called alpha iron (α_{Fe}). The crystal lattice transforms back to a bcc structure [11].

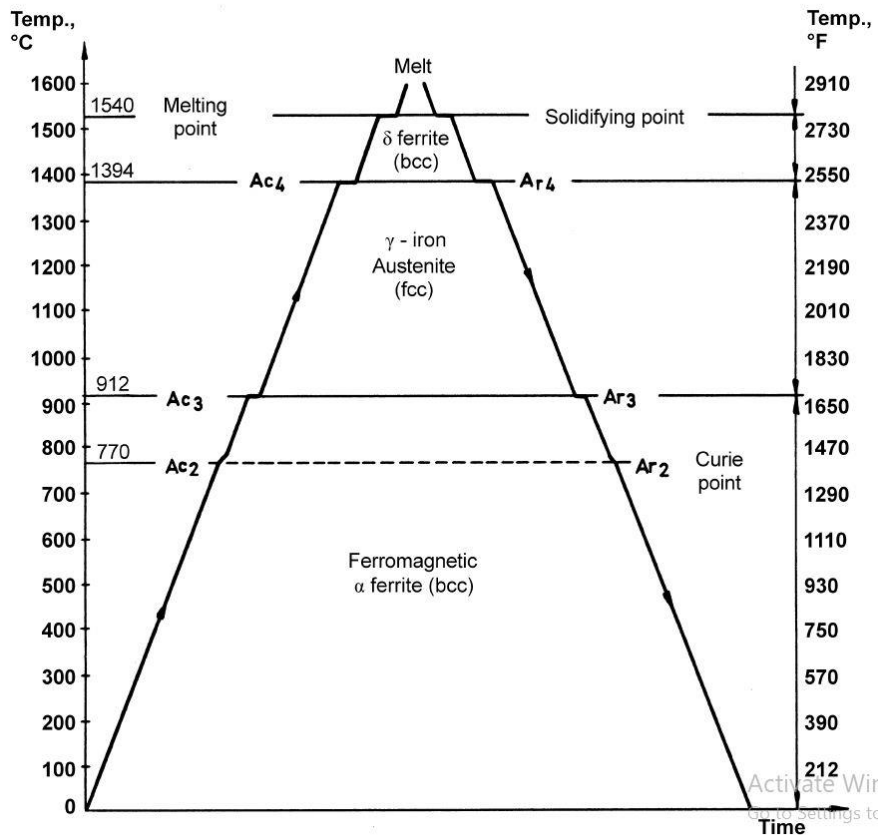


Figure 1 Allotropes of pure iron [12]

Ferrite dissolves a low concentration of carbon (0.021 wt% at 723°C, which is the eutectoid temperature). Austenite is found to dissolve a considerably larger amount of carbon than ferrite, owing to its lattice structure (2.04 wt% at 1147°C, which is the eutectic temperature). Delta iron dissolves 0.09 wt% C, at 1493°C. [2]

2.1.2 Iron-Carbon Phase Diagram

The most appropriate method to study Fe-C alloys is with the binary Iron-Carbon (Fe-C) phase diagram. This diagram gives an overview of the possible trends of iron alloys that can be formed depending on the amount of carbon added or the temperature at which the melt cools down. Based on the amount of carbon content added, the Fe-C alloys could be classified as follows:

- Steels: refers to those alloys with carbon less than 2.14% by weight. They have wrought alloys which can be distinguished by their high tensile strengths, good ductility, and their low costs. [2]
- Cast Iron refers to the ferrous alloys with carbon greater than 2.14% by weight. They usually contain other alloying elements such as Silicon (often 1 to 3% by weight) and they cannot be forged owing to their hard-micro-constituents. They are usually distinguished by their good wear resistance, hardness, and easy manufacturing process. [2]

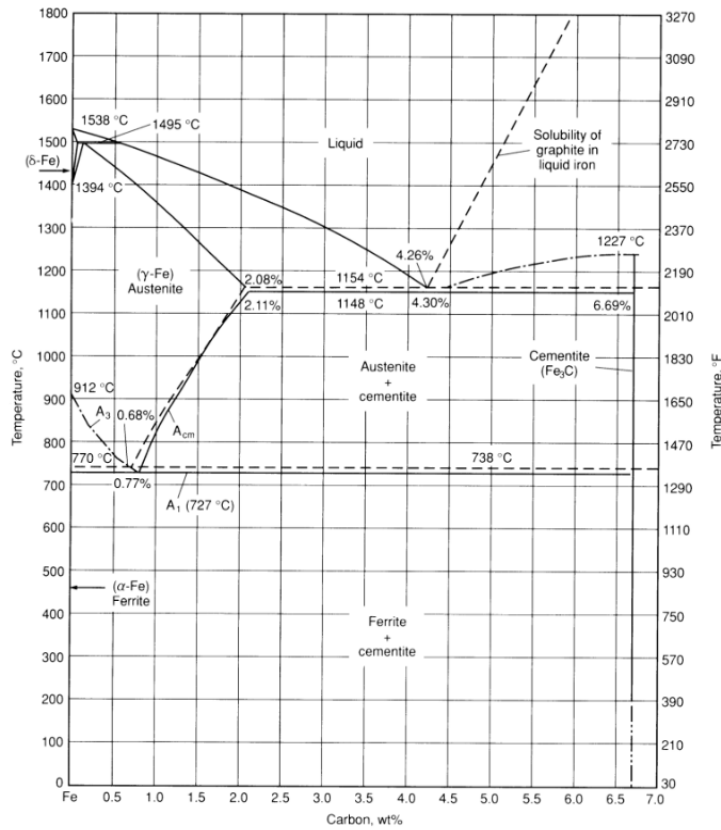


Figure 2 Iron carbon phase diagram [13]

The binary phase diagram can exist in two states- the Stable system where the carbon forms graphite and the Metastable system, where cementite is formed. This is solely differentiated based on the form in which carbon occurs, the graphitization potential, and the cooling rates involved during the solidification. However, this diagram is designed under an infinite cooling rate (under equilibrium thermodynamic conditions), hence making it difficult to implement this accurately from an industrial point of view.

2.1.3 Stable and Metastable System

Cast iron usually solidifies in two systems, depending primarily on the cooling rate during the solidification and the melt composition. They are the thermodynamically metastable Iron-Iron carbide (Fe-Fe₃C) system or the thermodynamically stable Iron-Graphite system. The carbon phase in the eutectic is the iron carbide for the metastable path and graphite for the stable phase [7]. Free graphite is the solid phase rich in carbon, which is produced under an infinitely slow cooling rate (the equilibrium condition). This is the stable Fe-C system. If the solidification occurs outside the equilibrium conditions, the carbon dissolves with the iron, in the solid phase, producing cementite (Fe₃C). this is the metastable system [14].

The formation of each kind of system is susceptible to several factors, namely the nucleation potential of the liquid melt, the cooling rate, and the chemical composition. The nucleation potential and the chemical composition of the melt determine the graphitization potential of the resulting cast, which is an important factor that determines if the solidification happens in the stable or the metastable form. Higher graphitization potential increases the chances of getting graphite in the eutectic, meaning it solidifies in a stable

form. These two forms of eutectic have wide differences in mechanical properties like hardness, strength, and ductility [7]. Graphite is an allotrope of carbon with a stratified hexagonal structure and cementite is an iron-carbon interstitial compound, that is hard and crystallizes with an orthorhombic structure. [2]

The main differences between both the systems are as follows:

- The stable system has lower solubility of carbon in the ferrite and the austenite.
- The eutectic and eutectoid transformations happen at a higher temperature in the stable system.
- The percentage of carbon at the eutectic and eutectoid points are lower in the stable system. [14]

2.1.4 Different phases in the Cast Iron Solidification

Traditionally, cast iron solidifies in two forms- white cast iron, where the carbon phase is as cementite, and grey cast iron, where the carbon-rich phase solidifies as graphite. The most common phases that could be present are Ferrite(α), Austenite(γ) and free graphite (when solidifying in the stable condition), as opposed to the cementite (formed when solidifying in the metastable condition).

- Ferrite (α): This is one of the most common phases present in cast irons and steels. Ferritic grains have a Body Centred Cubic (BCC) lattice structure, hence accounting for the lower amount of carbon that can dissolve in them (0,021 wt% at 723⁰C) [14]. This form of iron is formed below the eutectoid temperature, after cooling proceeds from the austenitic phase-field [13].
- Cementite: This is iron carbide, a compound with iron and carbon as Fe₃C. Cementite usually exists as a precipitate in ferrite in steels (as a grain boundary constituent) and hence is not present as 100% of the microstructure [13]. In cast irons, they usually exist as pearlite, formed by the eutectoid reaction of the decomposition of austenite into ferrite and cementite. It is formed in the metastable system and has an orthorhombic crystallographic lattice structure, leading to its high hardness and brittle nature. They are usually formed when the cooling rates are quite high and prominent, but breakdown into graphite and ferrite when the cooling rates aren't enough or too slow [14].
- Pearlite: This is a eutectoid mixture of ferrite and cementite and is formed below the eutectoid temperature. This phase exists generally in a lamellar structure, with alternating cementite and ferrite phases. This structure arises from the coupled growth of these two phases during its transformation from austenite. The transformation further depends on the amount of carbon diffused in the austenite (or the movement of the carbon in the iron lattice structure). Usually, they grow at a prior austenitic grain boundary [13]. Smaller spacing between two respective lamellae results in a higher strength [14].

- Austenite (γ): This is a solid solution of iron with a Face Centred Cubic (FCC) structure. This is the parent phase of ferrite, cementite, and pearlite, although cementite can be formed directly from the liquid, as in the case of white irons. This is generally a high-temperature phase and exists well above the eutectoid temperature, around 700 °C. This is stable at room temperature if there is a considerably high amount of carbon content and other alloying elements in the melt [13]. The alloying elements added to stabilize it usually includes manganese or nickel [14]. Austenite is usually characterized by its toughness at low temperatures and excellent weldability [13].
- Graphite: this is the stable form of carbon existing in cast irons. The morphology of this determines the kind of cast iron formed as well as helps to determine the thermal and mechanical properties of the casting [15]. Graphite crystals are faceted and bound by low index layers. Atoms within the same plane or layer are linked by strong covalent bonds but the different planes are bound by weak Van der Waals forces. The growth of the crystal happens in two axes, namely, the a-axis and the c-axis [2]. In LGI, the graphite is flaky, and its growth is along the dominant direction, along the a-axis. Hence, it has very good thermal conductivity. CGI has no preferential growth direction and can orient along both the a-axis and the c-axis. SGI has the graphite layers growing in the c-axis, hence yielding the nodular shape and lower thermal conductivity.

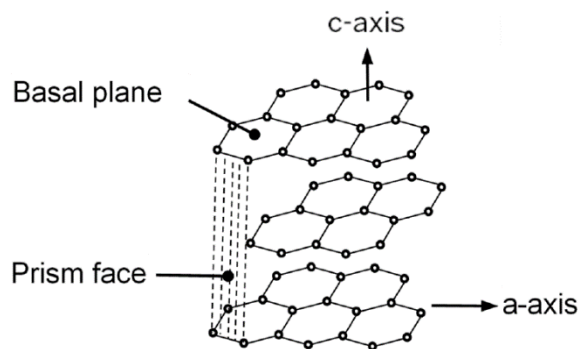


Figure 3: Graphite structure and growth direction [1]

2.1.5 Carbon Equivalent

Generally cast irons contains more alloying elements other than carbon, in order to control the solidification process and the matrix properties. The influence of these alloying elements on the solidification properties are represented in the binary Fe-C diagram, where, the carbon content is substituted with a carbon equivalent. The. Moreover, it is also used to understand how other alloying elements influence the cast iron during the solidification [14]. The general formula used to calculate the carbon equivalent is given below:

$$CE = \% \text{Total Carbon} + 1/3(\% \text{Silicon} + \% \text{Phosphorus}) \quad [16]$$

From the above equation represents that the Fe-C-Si-P alloy and the Fe-C alloy with carbon equivalent 4.3% solidify more or less approximately.

Another important factor is that the same Carbon equivalent value can lead to different properties which are due to the presence of other alloying elements and the different cooling conditions. [1]

2.2 Classification of Cast Iron

Cast irons are generally classified depending upon the carbon equivalent and graphite morphology.

2.2.1 Classification Based on the Carbon equivalent

Cast iron with carbon equivalent more than 4.3% is called Hypereutectic which are suitable for heat shock application such as ingot mold. Whereas iron with less than 4.3% is known as Hypoeutectic. Finally, the iron with carbon equivalent near to 4.3% are near-eutectic. [16]

2.2.1.1 Hypoeutectic

Cast iron with less than 4.3% of carbon equivalent. This composition begins with the nucleation and growth of the austenite as the primary phase. This primary phase grows dendritically. [17]

2.2.1.2 Eutectic

Eutectic temperature is 1148 °C, below this temperature the eutectic reaction occurs. In this reaction the liquid will transform into austenite and a rich carbon phase, where graphite is precipitated in the rich carbon phase. However there is chance for the metastable cementite (Fe_3C) to precipitate if there is no sufficient time for carbon to migrate. Eutectic alloys are with approximately 4.3% of carbon equivalent. [18]

2.2.1.3 Hypereutectic

Cast iron with more than 4.3% of carbon equivalent. This composition begins with the nucleation of the graphite as the primary phase. This is due to the rich carbon content, as a result, hypereutectic alloys are generally weak compared to hypoeutectic alloys. [19]

2.2.2 Classification Based on Graphite Morphology

The solidification of cast iron through the stable way results in a graphitic microstructure of carbon and not cementite. Depending on the solidification of graphite and the morphology of this form of carbon results in the following kinds of cast irons.

2.2.2.1 Lamellar Grey Iron (LGI)

This is a form of graphitic cast iron where the graphite morphology exists as inclusions. This iron is a widely used engineering alloy due to its good machinability and lower costs. This is a result of the graphite flakes being able to lubricate the cut. The graphite in this type exists as flakes and hence they are called Lamellar Grey Iron (LGI) [15]. The lamellae can be arranged in different orientations, shapes and scales as shown in Figure 4 below.

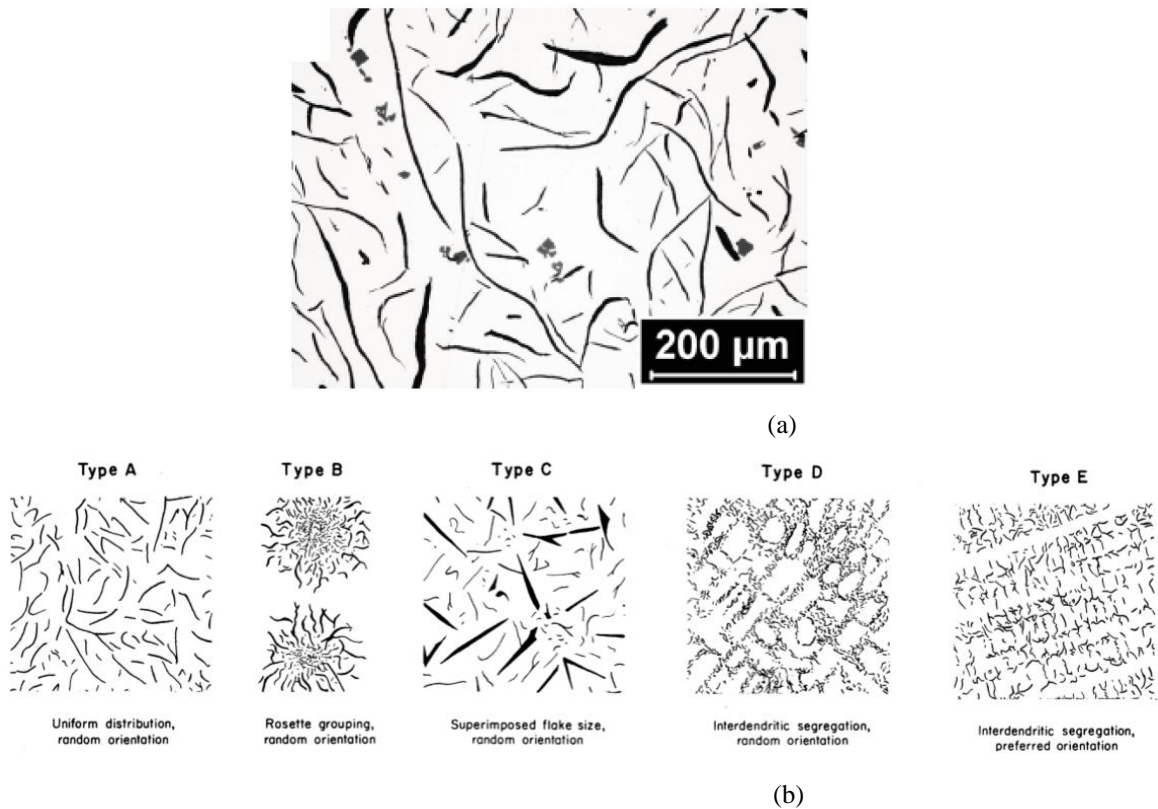


Figure 4:(a) Lamellar Graphite Iron(LGI) and (b) Different orientations of graphite in LGI [15]

LGI has lower tensile strength, since the graphite flakes function as notches, hence propagating cracks through the length of the flake. However, higher graphite content results in good thermal properties like good thermal conductivity and higher specific heat capacity [15].

2.2.2.2 Compacted Graphite Iron (CGI)

This form of graphitic iron is also called Vermicular Graphite Iron, as the graphite particles here have a wormlike appearance [15]. This form is a transition from LGI and the Spheroidal Graphite Iron (SGI). The graphite grows in both the C and the A-axis, giving it a wormlike appearance. CGI usually has better mechanical properties than LGI and better thermal conductivity than SGI. Owing to this fact, CGI is most suited for components that are prone to both thermal and mechanical stresses [15].

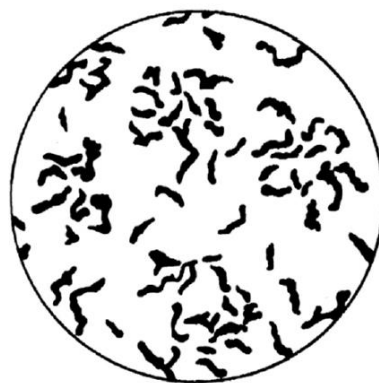


Figure 5: Compacted Graphite Iron (CGI) morphology [1]

2.2.2.3 Spheroidal Graphite Iron (SGI)

This form of Iron is also called Ductile cast iron or Nodular Cast Iron. The graphite morphology, in this case, is spherical or as nodes, hence giving it excellent flexibility, elasticity, and Ductility [15]. However, the thermal conductivity of SGI is the least compared to CGI and LGI, due to the nodular nature of graphite.

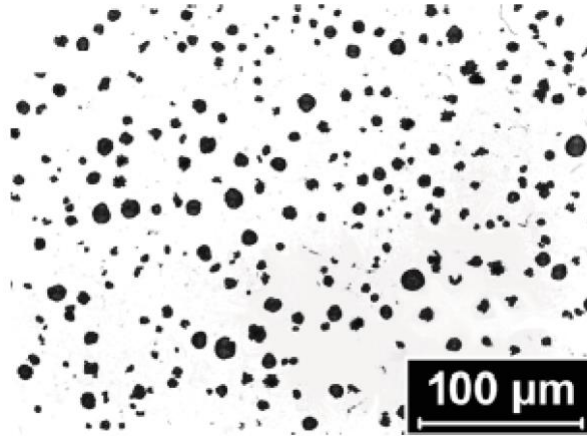


Figure 6: Spheroidal Graphite Iron (SGI) morphology [15]

2.3 Solidification of Cast Iron

One of the most important factors of the casting process is the solidification process, which helps to determine the final microstructure and hence the physical and mechanical properties. The solidification process is a transformation phenomenon in which liquid is transformed into a solid state, where the atoms in the short-range order of the liquid phase rearranged into a regular position in the solid-state [20].

Cast iron can solidify either in a stable Fe-Gr system or metastable Fe-FeC₃ system depending upon the chemical composition and cooling rate. When the cast iron is solidified in the stable system, the rich carbon phase in the eutectic is graphite, whereas in the metastable system the rich carbon phase in the eutectic is iron carbide [21].

2.3.1 Solidification of Hypoeutectic Cast Iron

The solidification process of hypoeutectic LGI consist of two steps, the first step initiates the nucleation and growth of primary austenite, while the second step contains the growth of both graphite and austenite at the eutectic [22]. The basic microstructure formed during the solidification of hypoeutectic cast iron is shown below Fig (7).

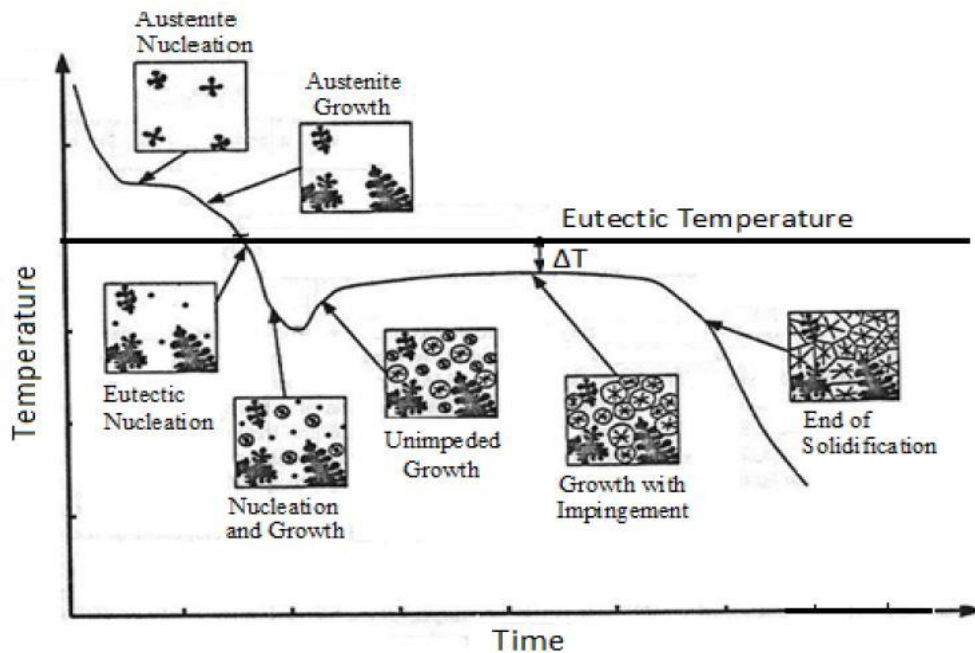


Figure 7: Solidification mechanism of hypoeutectic cast iron [23]

2.3.1.1 Nucleation of Primary Austenite

The first stage of solidification is the nucleation of primary austenite that occurs below the liquidus temperature. During nucleation, there is sufficient undercooling required to form the nuclei of the critical radius. The nuclei will only grow and become stable once this sufficient undercooling is reached, otherwise the nuclei would dissolve in the melt [3]. There are two types of nucleations, namely homogeneous and heterogeneous nucleation. In homogeneous nucleation, it is difficult to obtain certain undercooling essential for the nucleation to start, due to its high interfacial energy. Whereas, in heterogeneous, maximum undercooling can be observed as it has lower interfacial energy. Due to this fact, the nucleation in cast iron is considered as heterogeneous nucleation [24].

The favorable spots for the nucleation of primary austenite are the surface of the mold wall and the impurities present in the melt [24]. Other factors which promote the nucleation of primary austenite is the nucleating agents, pure iron is the most effective inoculant since it has the same crystal structure as primary austenite. Other inoculants include Silicon carbide, Graphite, and Silicon dioxide powder [3].

2.3.1.2 Growth of Primary Austenite

During solidification the impurities present in the metal will be rejected to the liquid interface, this is because only pure metal will solidify. As a result, it will lower the melting point of the liquid and cause the liquid-solid interface to become unstable. Due to this, the solid interface becomes rough with sharp points extending into the liquid called dendrites [25].

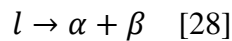
In the hypoeutectic solidification, the growth of primary austenite is usually in the form of dendrites [26]. The growing dendrites consist of three arms namely the primary arm (main arm), secondary and tertiary arms. The primary arms grow along with the orthogonal direction, whereas the secondary and the tertiary arms branch off from the tip of the main arm [27]. If the thermal gradient of the mold is higher from outside wall to

inside wall, then the dendrites will grow perpendicular to the wall of the mold, this type of growth is called columnar growth, and the region is known as the columnar zone [25]. On the other hand, the second type of growth known as equiaxed which has similar dimensions in all directions and grows in six orthogonal directions due to its face-centered cubic structure [25]. Moreover, the columnar and equiaxed growth will continue to grow until it collide with each other and block their growth respectively which leads to the dendrite coherency and this region is known as the columnar to equiaxed transition (CET) [3].

2.3.1.3 Eutectic Reaction

In the previous section, it stated that only a single solid phase (primary austenite) was nucleated either in the form of columnar or equiaxed dendrites under the liquidus temperature. As the solidification process continues to take place, the impurities in the liquid will get higher and at this point, there is a necessity for a second phase (Graphite) to nucleate and develop simultaneously with the first phase (Austenite) to continue the process without any variations [28].

Eutectic reaction is a process in which the liquid is directly converted into two solid phases (α & β)



Primary austenite is the first solid phase to nucleate in the hypoeutectic composition, as it starts to grow, a segregation process takes place in which the carbon present in the austenite will be rejected into the liquid. As a result, the amount of carbon in liquid tends to increase and lower the melting point. When it reaches the eutectic composition, the carbon present in the liquid starts to precipitate as graphite (Second solid phase) and comes in contact with the already nucleated austenite (first solid phase), then it begins to grow simultaneously to form the eutectic cell [2].

2.3.2 Solidification of Hypereutectic Cast Iron:

Hypereutectic cast irons are those whose Carbon concentrations exceed the eutectic concentration. The solidification begins with the crystallization of a carbon-rich phase, due to its abundance. As the temperature falls below the eutectic, the liquid converts to austenite and the carbon-rich phase. In the stable system, graphite is the carbon-rich phase which solidifies. However, in the metastable system, cementite (Fe_3C) may form as a substitute for graphite, if there isn't enough time for the carbon to dissipate in the melt [27]. For most applications, the stable γ +G eutectic is preferred as the Fe_3C is hard and brittle.

2.3.2.1 Nucleation and Growth of Primary Graphite:

Owing to the higher carbon content in the melt, the carbon starts nucleating heterogeneously and solidifies as the primary phase, below the Liquidus temperature. The hypereutectic compositions of cast irons are characterized solely by the carbon-rich phase being more stable than the γ .

The density of the carbon is relatively lower than the rest of the iron melt. This tends to raise the carbon in the melt due to buoyancy. This phenomenon, usually called floatation, unnecessarily causes the graphite to pile up in specific areas of the casting or on the melt

surface [29]. Primary graphite is usually undesirable for castings as this solid-phase tends to reduce the mechanical properties of the casting.

Literature suggests that the graphite nucleates around sulfide cores encompassed with oxide shells. However, the graphite morphology after solidification depends on the melt conditions, ranging from plate-like morphologies to spheroidal morphologies [29]. However, the procedure to obtain lamellar morphologies for the graphite depends on the addition of impurities like MnS, as previous studies have shown that nodular morphology is the usual common form to solidify for hypereutectic compositions [29].

2.3.2.2 Growth of the Graphite-Austenite Eutectic:

The solidification of primary graphite in the melt increases the equilibrium temperature of γ as the carbon is segregated from the liquid melt. This allows the melt to reach a certain temperature and concentration which allows the solidification and growth of both the solid phases in it. Both phases nucleate and grow with stability, by exchanging the solute through the liquid [27]. Both the phases grow simultaneously supporting each other. The growth of the graphite depends on the segregation of carbon at the interface and the growth of the austenite depends on the expulsion of the carbon from the liquid melt [27]. This is the eutectic phase in hypereutectic cast irons, where both phases grow at distance from each other in the melt, but proceed with the growth simultaneously. This form of growth is referred to as a divorced eutectic or off-eutectic growth [27].

2.3.3 Factors Affecting Solidification

Several factors influence the solidification of the cast iron, which in turn helps to predict the final microstructure of the material.

2.3.3.1 Cooling Rate

The cooling rate largely depends upon the size of the mold used for the solidification of cast irons. As the size increases, the cooling rate will be lower, whereas the size is smaller, the cooling rate will be higher. The casting which is cooled rapidly will have the highest undercooling, which results in the growth of a large number of nuclei in the melt [30]. The cast which has the highest cooling rate will refine graphite size and matrix structure and at the same time, the cast will show high strength and hardness [31].

Another important factor to be considered is the pouring temperature, the cooling rate can be varied by varying the pouring temperature, and it can be noticed that higher pouring temperature can lead to slow cooling of the casting, which in turn leads to a smaller number of nuclei

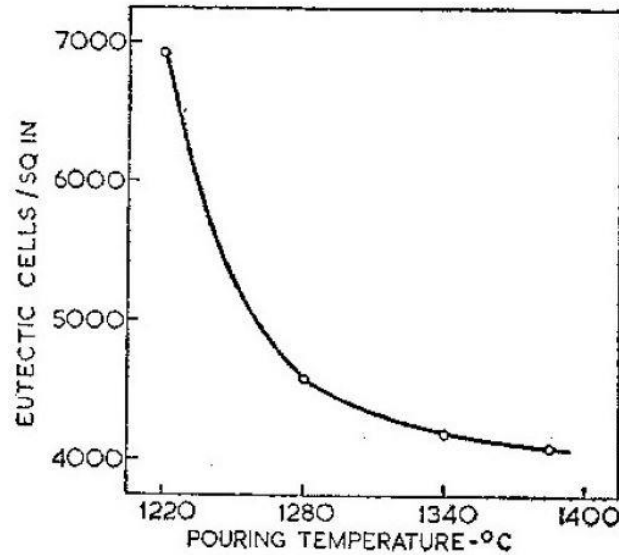


Figure 8: Curve showing the relation between Pouring temperature and the Eutectic cells formed [30]

2.3.3.2 Composition

The chemical composition has a great influence on the solidification of cast iron. Carbon and silicon are the most important alloying elements, high content of carbon and silicon leads to high graphitization potential as well as castability [21]. C, Si, Ni, Cu, and Al are the graphitizing alloying elements that promote the formation of the graphite and tend to follow the stable diagram. Whereas the alloying elements which promote the growth of cementite such as V, Cr, Mo, and Co are known as the whitening alloys and tends to follow the metastable diagram [32].

2.3.3.3 Undercooling

In foundry practice the solidification does not proceed when the thermodynamic equilibrium condition takes place, this is because the equilibrium condition requires constant temperature and a relatively slow cooling rate, which is difficult to obtain. As a result, the solidification of alloy starts below the liquidus temperature, for which it requires a certain level of undercooling [33]. Undercooling is referred to as a condition when the pure liquid subjected to a higher cooling rate, then the freezing will begin to start at a temperature below the real solidification temperature, undercooling is also known as supercooling. The difference between the freezing point temperature and the temperature at which the solidification starts is known as the degree of undercooling [34].

There are several factors which affect the undercooling in cast iron, some of them are as follows:

- The amount of silicon, lower the amount higher will be the undercooling.

- Proper inoculation, which leads to nucleation.
- The solidification rate, the faster the solidification rate the higher the undercooling.
- Size of the cast, thinner size has high undercooling compared to the large size cast samples.
- Carbon equivalent, high undercooling is generally observed in the hypoeutectic composition of grey irons [34].

2.4 Heat transmission in Lamellar Cast Iron

The thermal properties play a very important role in many cast iron parts, especially those which function at higher temperatures like engine blocks and cylinder heads of vehicles. This feature of transferring heat can prove beneficial to the components as it can reduce thermal fatigue and distortion [35].

Increasing the temperature in the material results in dimensional changes. The material expands when subjected to heating and contracts when cooled. If a component is subjected to non-uniform heat, some areas expand and others contract, owing to the different exposures to heat. These uneven expansions and contractions would result in thermal stresses, both tensile and compressive, within the same component [2]. These stresses can be subsequently decreased if the material has low values of stiffness, coefficient of thermal expansion, and also thermal gradients [35].

Increasing the temperature in the material results in dimensional changes. The material expands when subjected to heating and contracts when cooled. If a component is subjected to non-uniform heat, some areas expand and others contract, owing to the different exposures to heat. These uneven expansions and contractions would result in thermal stresses, both tensile and compressive, within the same component [2]. These stresses can be subsequently decreased if the material has low values of stiffness, coefficient of thermal expansion, and also thermal gradients [35].

2.4.1 Thermal Conduction

From a microscopic perspective, when the heat is provided to the material, this causes the atoms to vibrate rapidly, causing them to collide with the neighboring particles and thus transfers or conducts the heat through to these neighboring atoms. The heat is therefore transferred as internal energy [15].

In a solid material, there are namely two forms of heat transmissions:

- The most common way of heat conduction being that by electrons, as predominantly seen in the case of metals [2].
- Conduction by phonons, which are caused by the vibrations in the lattice of the crystal, which transmits the heat as waves through the entire crystal. This is predominantly seen in the case of graphite) [36].

Fluids, mostly gases have the least conductive nature among all types of materials. Heat always flows from a region of higher temperature to a region of lower temperature till a thermal equilibrium is attained. In most cases of study, the difference in temperature which

favors the conduction is considered a constant. This form of conduction is called the Steady-state Conduction, where after thermal equilibrium is attained, the spatial distributions of temperature always remain the same. Moreover, the amount of heat entering the domain is equal to the amount of heat leaving the considered domain [15].

The conducted heat is perpendicular to the heat flow and it can be determined using Fourier's law of heat conduction,

$$\frac{q_x}{A} = -k * \frac{dT}{dx} \quad [2]$$

Where:

$\frac{q_x}{A}$ is the heat conducted per unit area, which is perpendicular to the heat flow.

k is the thermal conductivity of the material.

$\frac{dT}{dx}$ is the temperature gradient in a particular direction (the x-direction in this case).

The negative sign in the equation takes into consideration the fact that the temperature gradient and the direction of the heat transfer are opposite to each other, as abided by the second law of thermodynamics.

2.4.2 Thermo-physical Properties:

The major property considered for observing the thermal behavior is the thermal conductivity and this could be measured only by understanding correlated properties namely the thermal diffusivity, the specific heat, and the thermal expansion of the cast iron samples considered.

2.4.2.1 Thermal Conductivity:

The thermal conductivity is the capacity of the material to conduct heat through a medium which has a temperature gradient [36]. Thermal conductivity (usually denoted by λ or k) can be defined as the heat required per unit area to produce a temperature difference of 1°C between two faces of a homogenous material, in unit time. The International System of Units (SI unit) of measuring the thermal conductivity is expressed as W/(m. K).

The thermal conductivity can be directly measured for steady-state heat conduction (through Fourier's law of conduction). However, for a transient flow where the conduction of heat is not uniform, the λ is quite hard to calculate directly. Hence, in these cases, the thermal diffusivity (α_D) is also considered [35].

$$k = \rho * Cp * \alpha_D \quad [37].$$

Where:

k is the thermal conductivity of the material.

ρ is the density of the material considered

C_p is the Specific heat capacity

α_D is the thermal diffusivity of the material considered.

2.4.2.2 Thermal Diffusivity:

The thermal diffusivity is another major property related to heat conduction. This measures the speed at which heat propagates through the medium at a particular change in temperature with time. Thermal diffusivity can thus be defined as the quantity of heat that is conducted through the unit volume of a material with a temperature difference of 1°C between its end faces [38]. This property is directly proportional to the thermal conductivity, meaning that a material that conducts a high amount of heat (good thermal conductivity) propagates more heat from one end face to the other end face of the material (hence having good thermal diffusivity). Thermal diffusivity is represented by α_D and its SI unit is mm^2/s .

2.4.2.3 Specific Heat Capacity:

This property describes the capacity of the material to store heat and is the measure of the material's internal energy. It is denoted by C_p and its SI unit is $\text{J}/(\text{kg K})$. It shows the relationship between heat deposited and the increase in temperature [38] and is hence defined as the amount of heat necessary to raise the temperature of a unit mass of a substance by 1°C.

2.4.2.4 Coefficient of Thermal Expansion (CTE):

This is a property of the material which indicates how much the material expands on exposure to heat. The thermal expansion coefficient is linearly and directly proportional to the temperature changes when it is measured over small ranges of temperature. The coefficient of thermal expansion is defined as the elongation of the material measured over an increase of temperature by 1°C. The SI unit of this measure is K^{-1} and is often expressed as α [39].

$$\alpha = \frac{dl}{L_0} * \frac{1}{dt} \quad [39]$$

Where:

α is the coefficient of thermal expansion

$\frac{dl}{L_0}$ is the elongation of the material (change in length by the original length of the material)

dt is the temperature change in the material.

As far as thermal conductivity measurements are considered, the density of the material varies with temperature elevation and hence the thermal expansion coefficient is an important term that determines the density at elevated temperatures. The density is usually inversely proportional to the increase in temperature, the reason being that the mass of the material remains constant but the volume increases, hence reducing the density. The density at elevated temperatures can be calculated by the equation

$$\rho_T = \frac{\rho_0}{1+3\alpha\Delta T} \quad [40]$$

Where:

ρ_T is the density at elevated temperature

ρ_0 is the original density at room temperature

α is the thermal expansion coefficient.

The density of the sample at room temperature is obtained using the Archimedes principle, which considers the effect of buoyancy on the sample. The sample is first weighed in air and then immersed in distilled water at the same known room temperature [41]. The difference fractioned by the density of water at room temperature gives the volume of the sample. Thus, by the general calculation, the mass of the sample at room temperature divided by the calculated volume of the sample at room temperature gives the resultant density of the sample at room temperature, ρ_0 .

$$\rho_0 = \frac{m_{air}}{m_{air}-m_{H2O}} \rho_{H2O} \quad [15]$$

Where:

ρ_0 is the density of the sample at room temperature

m_{air} is the mass of the sample measured in air

m_{H2O} is the mass of the sample measured in distilled water

ρ_{H2O} is the density of water at room temperature.

2.4.3 Influence of Microstructure on the Heat Conduction:

The heat conduction in lamellar graphite iron is mainly due to the graphitic carbon flakes. This is also since carbon has high thermal conductivity. The heat diffusion is more rapid along the a-direction, which is also the axis along which the graphite flakes grow. Graphitic carbon has a thermal conductivity of 130 W/(mK) [42]. When the structure of graphite is considered, the hexagonal growth direction (along the a-axis) has stronger covalent bonding than the prism planes (c-axis) which are bonded by weak Vander Waals bonding. Hence, the heat conduction is significantly higher along the hexagonal growth direction rather than along the prismatic plane [40]. Furthermore, graphite flakes grow and orient themselves along the a-axis, hence making lamellar graphite iron the best for applications requiring good thermal properties.

The eutectic cells of Lamellar graphite iron comprise an intricately interconnected network of graphite flakes, which means that the mean free space between each flake is reduced. This allows a larger scope for the conduction of heat between the flakes and the heat is conducted over greater distances, hence increasing the thermal conductivity over compacted and ductile irons. The thermal conductivity of graphite in the iron is anisotropic. Previous literature has also suggested that the longitudinal alignment of the base planes of the graphite morphology proves beneficial for heat propagation. As the

carbon equivalent is increased, the corresponding graphite fraction also physically increases, owing to better thermal conductivities.

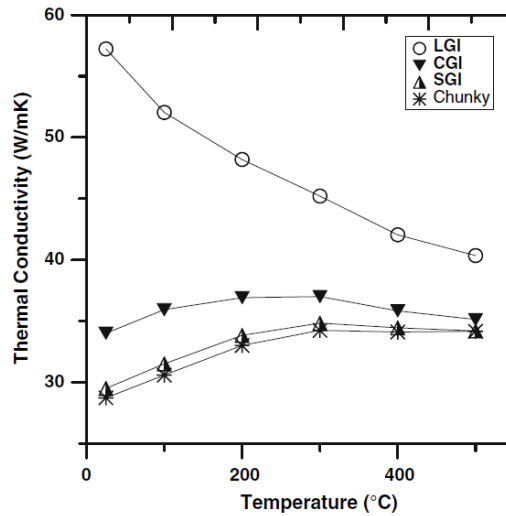


Figure 9: Curve showing the thermal conductivity v/s temperature for Lamellar graphite iron, Compacted graphite iron, and Spheroidal graphite iron. [41]

Although the conductivity of LGI is greater than the other forms of cast iron, the values of thermal conductivity steadily decrease with temperature increase, as seen from figure (9). SGI and CGI however have less dependency to the temperature. Previous investigations have shown that the curves could sometimes show an increasing trend till a maximum is attained and then a steady decrease, or a constant increase or a constant decrease for SGI and CGI, similar to the trend seen in LGI. Hence it is not entirely wise to depend on previous literature for determining the general trends for the thermal conductivity curves, rather the trend depends on the material composition [36]. There is a scarce discussion on the reduction in thermal conductivity with increasing temperatures, although the same trend has been seen in many reports [4].

Previous literature has observed that the thermal conductivity is more for grey irons with A-type graphite flakes as they are longer and have more paths for heat conduction. This is also because the presence of type-A graphite ensures a better interconnection between the graphite flakes. The thermal conductivity and the thermal diffusivity seem to reduce appreciably when there is the presence of undercooled type-D graphite as they are finer and scattered around the austenite grains [35].

A recent experiment conducted by the Department of Mechanical Engineering and Component Technology, Jönköping University, compared four different carbon equivalents for grey cast irons, with three different cooling rates. These dissimilar cooling rates along with the varied carbon content affected the thermal transport properties of the grey irons. A difference of 30 W/(mK) was observed between the thermal conductivities of high carbon samples cooled at a medium and slow rate and then rapidly cooled sample with a low content of carbon, as shown in figure (10). As the carbon content reduces, the conductivities seem to be less dependant on the temperature owing to the higher influence from the matrix. For low carbon grey irons (Chill_4 in the figure (10)), the undercooling results in an increased fraction of the primarily solidified austenite dendrites. Thus, in this case, the propagation of heat seems to correspond more with the primary dendritic matrix rather than the graphite flakes. The thermal conductivity seems to increase to roughly

400°C and then reduces [40]. Similar behavior has also been observed for compacted graphite iron and spheroidal graphite iron [41], from figure (9) owing to the fact that matrix influences heat conduction largely.

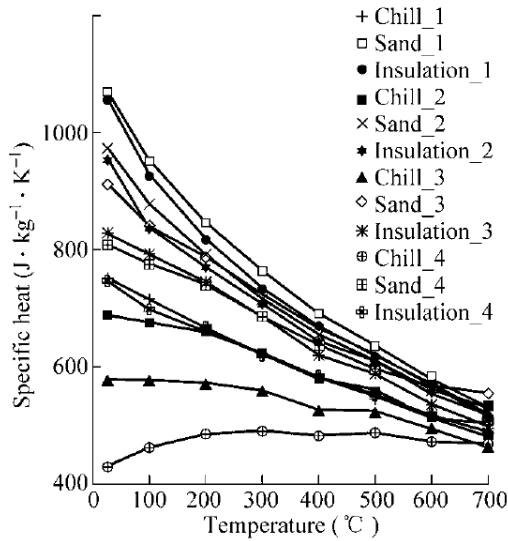


Figure 10: thermal conductivity trends in cast irons with different carbon contents and cooling rates [40]

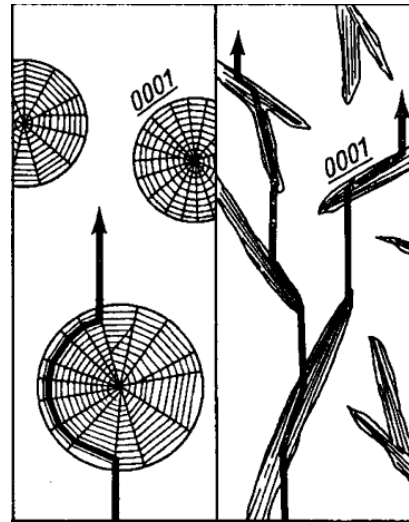


Figure 11 : Heat transmission in LGI and SGI depending on the graphite morphology [35].

2.5 Static Mechanical Properties Of Lamellar Graphite Iron

The mechanical properties of grey cast iron are greatly influenced by the matrix structure formed (perlite or ferrite), the formation of the graphite. The cast irons with perlitic matrix structure are generally used in industrial applications because of their good surface finish, high modulus of elasticity, high strength, and good damping properties. On the other hand, the irons with a ferritic matrix structure are not used significantly in industrial applications due to its low strength. Another fact which should be considered is that the machining ability of the irons and it is found that the high strength perlitic irons are a bit difficult to machine compared to the ferritic irons, this is because of its matrix hardness [43].

Generally, the grey cast irons are brittle in nature, and due to the presence of multiple cracks at the tip of the lamellae graphite its shows a non-linear mechanical behavior [44]. The other important elements that distinguish the mechanical properties are tensile strength.

2.5.1 Tensile Strength

Tensile strength is defined as the maximum strength used to break a tensile specimen in a unit area of cross-section [45].

$$\text{Tensile strength} = \frac{\text{Maximum force used}}{\text{Original area of cross - section}}$$

The tensile strength primarily depends upon the chemical composition, inoculation, and cooling rate. The tensile strength is inversely proportional to the carbon equivalent, as more graphite in structure (high carbon equivalent) the strength decreases. The reason for the decrease in strength is that the graphite in the grey iron acts like void discontinuity or like an internal notch which thus limits the ductility and strength [46].

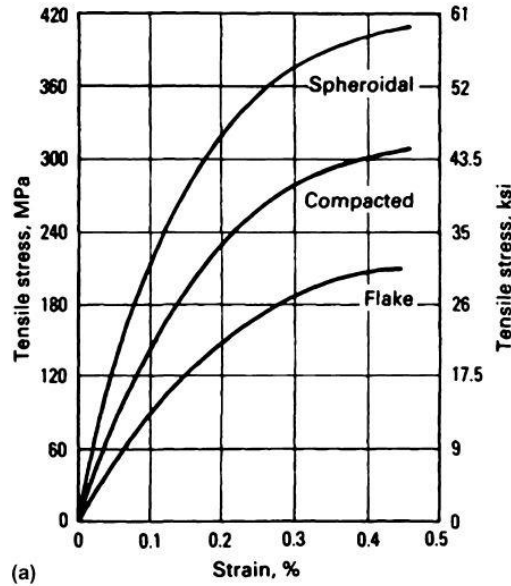


Figure 12: Influence of graphite in tensile strength [46]

Hypereutectic irons are those with more than 4.3% of carbon equivalent and they have very low strength because they contain coarse graphite and ferrite, while the irons with less than 4.3% are known as hypoeutectic and they have high strength compared to the hypereutectic irons because of the number and the size of the carbon decrease with decrease in carbon equivalent [46]. The relationship between the carbon equivalent and the tensile strength is shown in figure (13).

The introduction of alloying elements also influences the tensile strength like the addition of nickel increases the tensile strength and at the same time, it decreases the effect of section thickness. Another fact which is to be noted that only a slight increase in tensile strength can be achieved through the addition of the graphitizing elements, whereas the tensile strength can be enhanced remarkably by the introduction of carbide-stabilizing metals but it will have a negative impact on the machining ability [46].

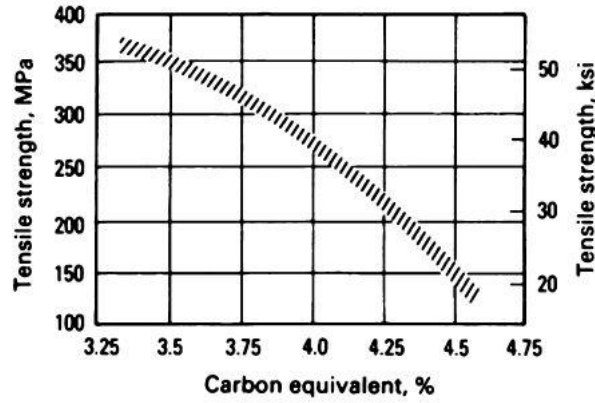


Figure 13: Effect of carbon equivalent on tensile strength [46]

2.5.2 Hydraulic Diameter

It is generally used to understand the dendrite-interdendritic morphology in hypoeutectic lamellar cast iron and as well as to examine the coarseness of the interdendritic space. [44]. The D_{IP}^{HYD} is defined as the ratio of the specific volume of the interdendritic phase which is denoted by V_{IP} to the specific area of the dendrite- eutectic interface denoted by S_{γ} , the equation is demonstrated below [8].

$$D_{IP}^{HYD} = V_{IP} / S_{\gamma} \quad [8]$$

from the above equation, the volume of the interdendritic phase is the difference between the total volume of the entire area and the volume of the primary austenite(dendrites). So the above equation can be rewritten as:

$$D_{IP}^{HYD} = V_{total} - V_{\gamma} / S_{\gamma} \quad [8]$$

The area fraction of the primary austenite is directly proportional to the volume of the primary austenite. Figure (14) shows the typical random distribution of the dendrites in a cubic domain [8].

To calculate the D_{IP}^{HYD} it is required to measure certain parameters such as the fraction of the primary austenite f_{γ} , area of primary austenite A_{γ} , and the periphery of the primary phase P_{γ} [44].

From the above mentioned parameters, the hydraulic diameter equations can be written as:

$$D_{IP}^{HYD} = \frac{L_0^2 - A_{\gamma}^{mean}}{P_{\gamma}^{mean}} \quad [8]$$

Where L_0 is the total length of the cubic domain, A_γ^{mean} is the mean dendritic area and P_γ^{mean} is the mean perimeter of the primary dendrites.

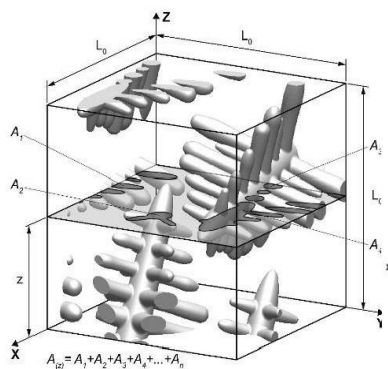


Figure 14: Random distribution of dendrites in cubic domain [44]

3 Method and implementation

This section gives a detailed overview of the methodology used to carry out the thesis. All the samples were prepared and cast at JU CAST and the equipment used for the tests was also a property of the Department of Materials and Manufacturing, Jönköping University.

The experimental work was carried out in the following stages as seen in the flowchart below, in figure (15).

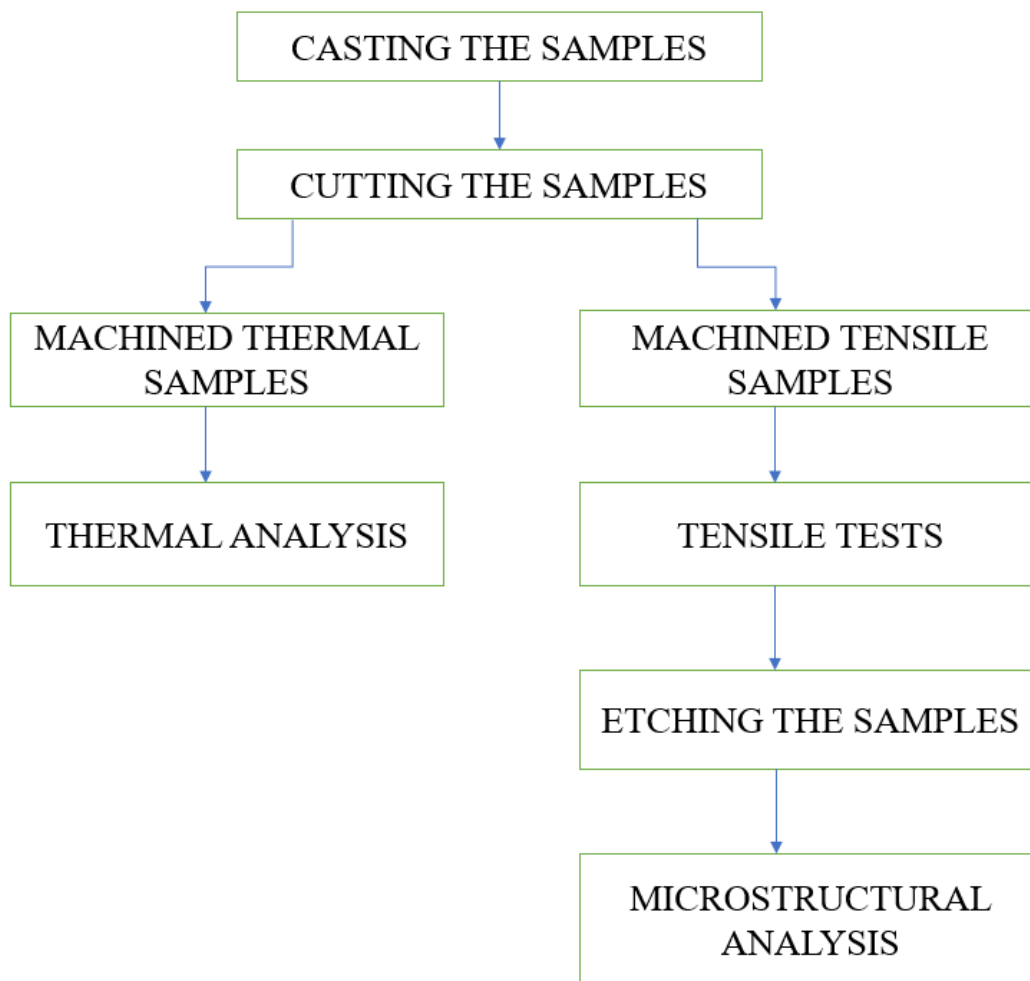


Figure 15: Flowchart showing the method implemented in steps

3.1 Casting the Samples:

The goal of the thesis is to identify the tensile and thermal properties of Lamellar grey Iron under varying cooling conditions and also varying carbon contents. Hence, different compositions were discussed to carry out the experiments. The Silicon content was fixed to a constant value of 4% by weight, and each had six varying Carbon contents, as shown in table 1.

CE	C	Si	P	Mn	S	Cu	Label
5.264667	3.93	4	0.004	0.4	0.058824	0.8	Si4C1
4.764667	3.43	4	0.004	0.4	0.058824	0.8	Si4C2
4.264667	2.93	4	0.004	0.4	0.058824	0.8	Si4C3
3.864667	2.53	4	0.004	0.4	0.058824	0.8	Si4C4
3.464667	2.13	4	0.004	0.4	0.058824	0.8	Si4C5
3.064667	1.73	4	0.004	0.4	0.058824	0.8	Si4C6

Table 1: The expected chemical compositions with different levels of carbon.

However, after the casting was carried out, the compositions of all the casts made were analysed by Volvo Group Trucks Technology AB and the concentrations of all the elements seem to vary a little from the expected values, as seen from Table 2 below.

CE	C	Si	P	Mn	S	Cu	Label
5.16	3.91	3.72	0.02	0.41	0.053	0.8	Si4C1
4.64	3.35	3.86	0.02	0.44	0.054	0.8	Si4C2
4.28	2.96	3.93	0.02	0.51	0.073	0.8	Si4C3
4.03	2.68	4.04	0.02	0.56	0.097	0.8	Si4C4
3.85	2.44	4.20	0.02	0.62	0.118	0.8	Si4C5
3.66	2.23	4.25	0.01	0.68	0.113	0.9	Si4C6

Table 2: The observed chemical compositions after casting, with different levels of carbon

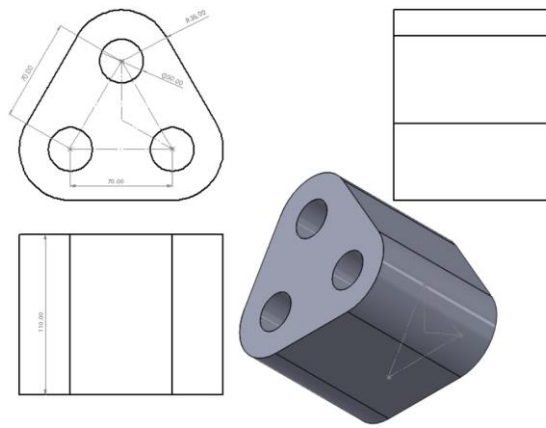
Phosphorous (P) must be kept low to avoid the promotion of steadite formation [47]. Mn and Cu are added to promote pearlitic matrix [48]. The amount of S is balanced with Mn according to :

$$\text{Mn} = 1.7 * \text{S} + 0.3 \text{ [48]}$$

This is to promote MnS near the onset of eutectic solidification. MnS plays a role in the nucleation of graphite [48].

Three different molds were used to achieve different cooling rates for the casts. They included cylindrical molds of 30mm, 55mm, and 80mm in diameter. The molds were made from 3D printed Silica sand.

There are three cylinders each for the 30 mm diameter molds, as seen from figure (16a) meaning each pouring can give three cylinders each of 30mm diameter, for each composition of Carbon. The thickness of the mold is 5mm and the height of the mold is 110mm. This cast cools the fastest. However, the initial design was altered to implement a pouring cup at the centre of the mold to uniformly distribute the melt into the three cylinders while pouring, as shown in figure (16b).



(a)



(b)

Figure 16:(a) 30mm Silica sand mold drawing and (b) 30mm mold with the implemented pouring cup in the middle.

As for the 55mm and the 80mm diameter molds, there is one cylinder each which could be cast for each composition, from figure (17). The 55mm diameter cylinder has a thickness of 60mm (given an outer diameter of 115mm). The height of the cast is 90mm, though the total height of the mold is 120mm. An allowance of 30mm has been given from the bottom end as seen from the figure, to allow for good heat dissipation. This cast has an intermediate cooling rate.

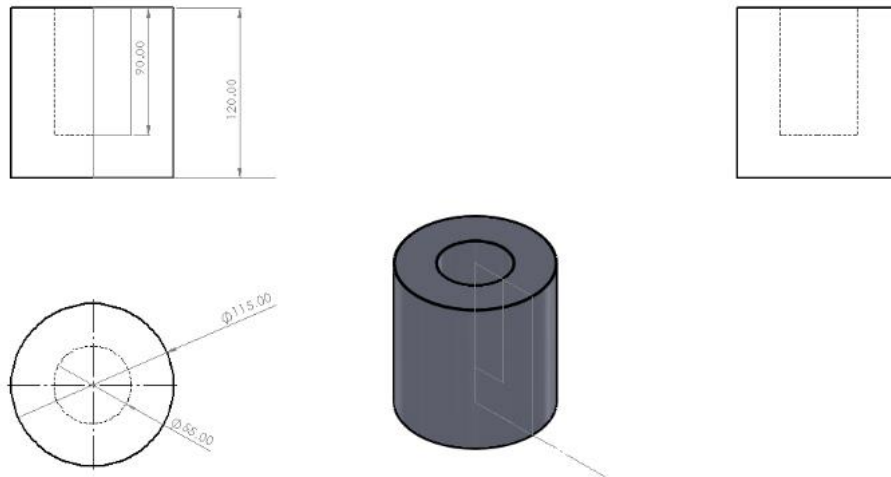


Figure 17: 55mm Silica sand mold drawing

The 80mm diameter mold has the slowest cooling, given the biggest mold size, from figure (18). The total outer diameter of the mold is 180mm, meaning a thickness of 100mm is provided for the sufficient transfer of heat from the inner wall of the mold to the outer wall and then to the surroundings. The height of the cast is 90mm, although the total height of the mold is 130mm. This means that an allowance of 40mm is given from the bottom, as seen in fig. This is to compensate for the proper heat dissipation from the bottom of the cylinder as well.

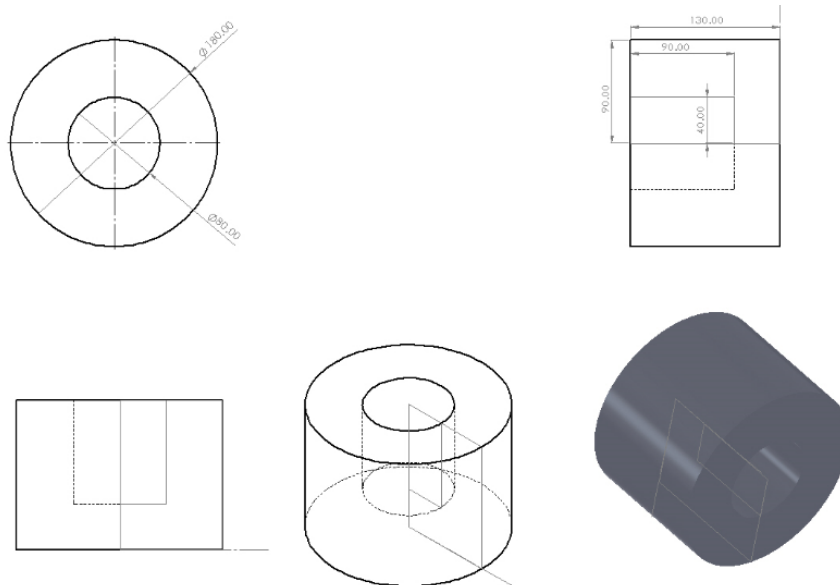


Figure 18: 80mm Silica sand mold drawing

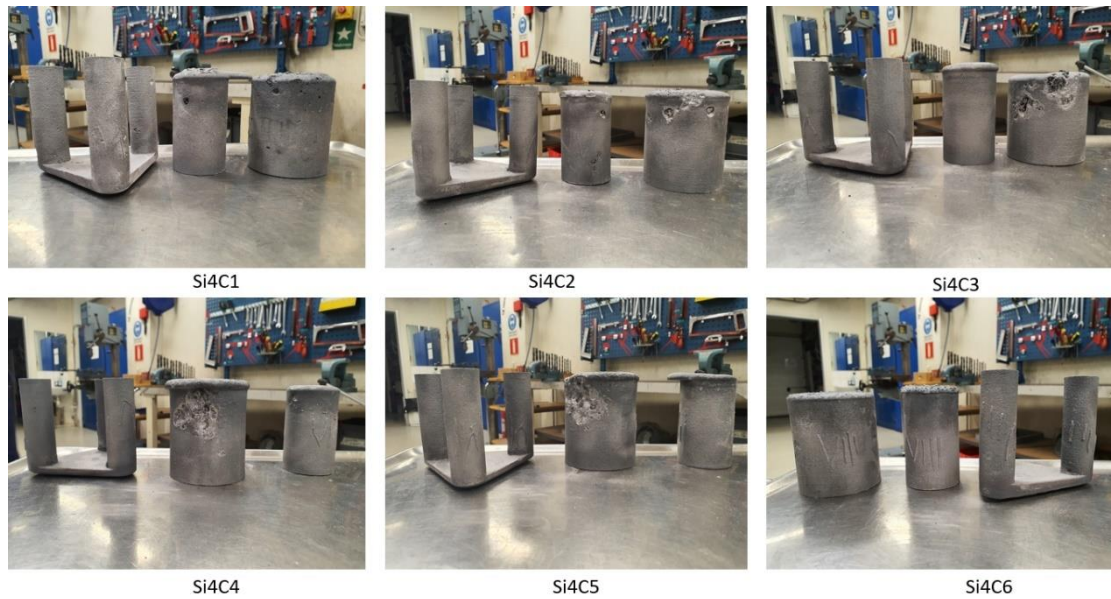


Figure 19: Casted samples for 4% by weight of Silicon.

The casted samples are as shown in figure (19). There are surface porosities in the cast, from figure (19), which might be due to the cracks formed on the mold during casting, as shown in figure (20). However, these porosities were fortunately not seen after cutting the samples. They are not favoured as they act as potential stress concentrators during tensile testing and they prevent the continuous flow of heat during thermal testing.



Figure 20: Cracks Generated in Molds

3D printed Silica sand is used to make the sand molds, preferably over Greensand. Binded silica sand is dry as opposed to green sand, which has a high amount of moisture. An increased amount of moisture content in the sand mold can affect and alter the melting or freezing temperature of the melt, hence increasing the rate of solidification [34]. This is not preferred as the casts are meant to be air-cooled naturally without being affected by moisture in the mold.

3.2 Cutting of the Samples:

Once the samples were casted and air-cooled, they were ready to be cut the thermal and tensile tests. The cutting tools used for the samples were namely the saw cutter to cut the samples and the lathe to shape the samples accordingly to the different tests.



Figure 21: Harrison Model M390 Gap Bed Lathe used



Figure 22: Proline 320.280H semiautomatic bandsaw used to cut the cylinders for the thermal and tensile tests

Once the casts were made, they were cut and machined separately for the tensile bars and the thermal samples. The samples for both the tests were machined from the same cast, for the 55mm and the 80mm diameter. However, the 30mm samples were in abundance, so the samples were made from the same cast, but from different cylinders. CAD models were designed to appropriately cut the tensile and the thermal samples from the same cast. Favorably, the casts had only superficial porosities, which could be machined out.

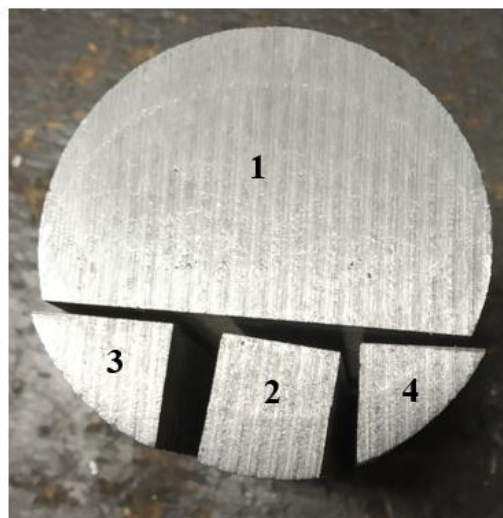


Figure 23: separated cut parts of the same cylinder for the different tests

From Figure (23), the part of the cylinder marked 1 is for the tensile tests and 2 is for the thermal tests. 3 and 4 are scrap material which is used for microstructural analysis to determine the thickness of the tensile samples. The surface porosities seen across the crosssection of the cylinders were removed after machining. The samples were machined from the mid-section of the casts, as the top and bottom were cut out owing to further porosities, which can be seen in figure (24).



Figure 24: Porosities seen on the top section of the cylinder

3.3 Machined Thermal Samples:

After cutting the samples, they were machined separately for both tests. For the thermal tests, three different samples were required for each composition respectively. They were for the Differential Scanning Calorimetry (DSC) apparatus, which measured the specific heat, the Dilatometer, which measured the thermal expansion coefficient, and the Laser Flash (LF) apparatus, which measured the thermal diffusivity. The samples for 30mm cast was machined from one whole cast. But, due to the availability of single casts for 55mm and 80mm diameter, the samples for these were machined from individual parts cut from the same cylinder (as seen as part 2 from the figure (23)).

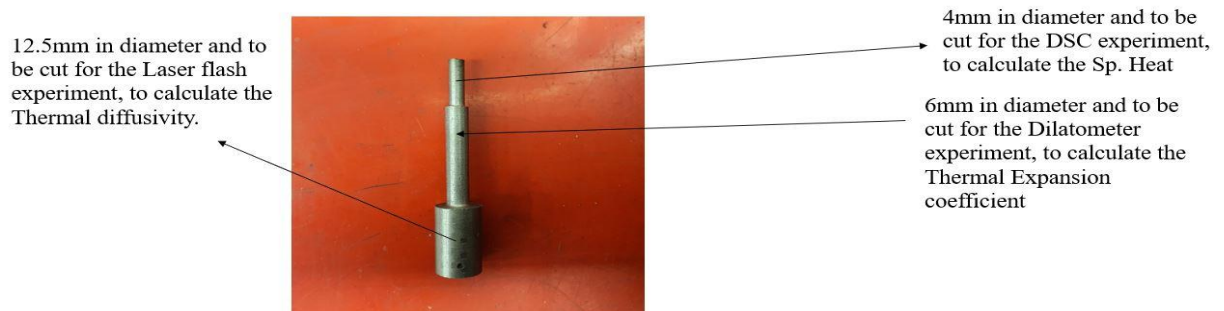


Figure 25: Machined thermal sample

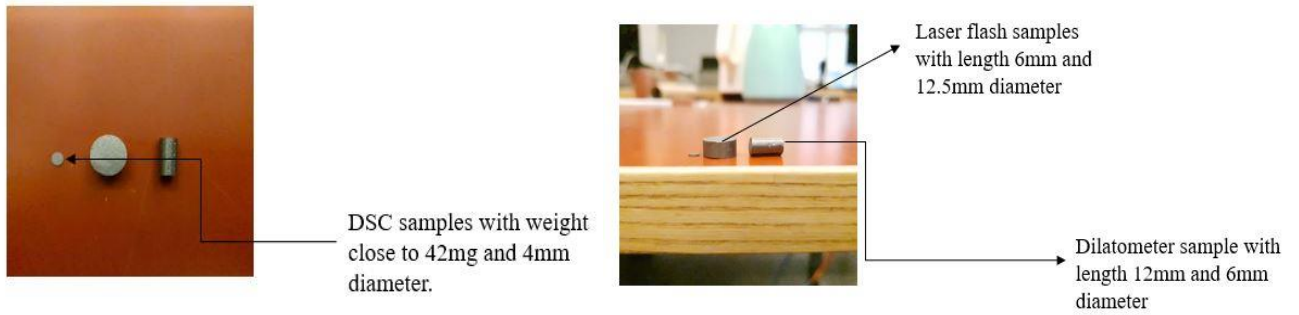


Figure 26: DSC, Dilatometer, and LF Samples For Thermal Test

The specifications and required dimensions of the machined samples can be seen in figure 18 and figure 19. No porosities were visibly seen after lathing and machining the sample, as seen, in contrast to the casts which had innumerable damages on the surface when cast. This proved very favorable while carrying out the tests as there was scope to machine out many samples. Once all the samples for the different tests were lathed as seen, they were cut out individually using a diamond cutter for hard materials. The disc for cutting was made at a constant rpm of 30rpm-40rpm, which was found ideal for grey iron. It was observed that cutting and lathing the samples became more difficult with decreasing carbon content, meaning Si4C1 was easier to cut than Si4C5 (from table 1 of compositions).

3.4 Thermal Analysis:

The thermal analysis involves the calculation of the thermal conductivity of the sample. This is done by measuring the Specific heat, the Thermal Expansion coefficient, and the Thermal Diffusivity of the samples separately and use these parameters to calculate the thermal conductivity. The Specific heat capacity is measured using the Differential Scanning Calorimetry (DSC) apparatus, the Thermal Expansion Coefficient is measured using the Dilatometer and the thermal Diffusivity is measured using the Laser Flash (LF) apparatus. The thermal conductivity is then measured manually from the data collected from the three tests.

3.4.1 Differential scanning calorimetry (DSC):

The Differential Scanning Calorimetry (DSC) is used to measure the specific heat capacity of a material (Cast Iron). Other analyzing possibilities that can be carried out in DSC are Transition and Reaction enthalpies, Temperature of melting and Phase Transformation, etc. The type of DSC machine used while experimenting is shown in figure (27). [49]



Figure 27: DSc Netzch 404 C pegasus [49]

The tests are performed in one chamber shared by a reference crucible, which remains empty, and another crucible where the sample is placed. Both the sample and the reference are exposed to the same heating conditions and then the specific heat is measured. This instrument cannot handle cases that include the decomposition of the sample and thus shouldn't be used for those samples which are reactive [49].

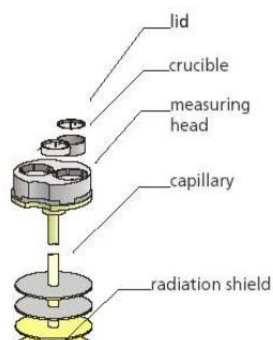


Figure 28: Differential Scanning Calorimetry set up to hold the sample [49]

This apparatus was susceptible to thermal lag. In the same heated environment, the difference in the heating rates between the two materials is called the thermal lag. This apparatus uses two crucibles prone to the same amount of heat, meaning both the crucibles should heat up simultaneously. However, as one of the crucibles is mounted with the sample to be tested, the heating properties get altered and hence does not maintain an equilibrium relationship. Thus data that is measured over a larger range of temperature seems to be less reliable due to an accumulated thermal lag [49].

The samples used in the DSC experiment are of 4mm diameter with a weight close to that of the selected reference sapphire standard. The initial weight of the sample cut from the cylinder was more than the required weight. The sample was polished and ground down till a weight close to that of the sapphire standard was attained. The sapphire standard has a measured weight of 42.5mg. The experiment begins by setting the atmosphere in the furnace and this is done by evacuating the furnace first, then filling it with argon. This step is repeated 3 times to ensure that a pure and uncontaminated gas environment is achieved in the furnace and it is also important to ensure the continuous flow of argon gas until the end of the measurement at the rate of 50- 70 ml/min. The flow of the purge (Argon gas) is controlled by a manual control system. The cast iron samples used in this experiment are heated up to 500°C, at a rate

of 10K/min and finally, it is cooled down to room temperature. The result obtained in this measurement was analyzed by using proteus analyzing software. The weights of the various samples used for the experiment are given in the table (3).

Labels	30mm diameter	55mm diameter	80mm diameter
Si4C1	41.3	41.4	41.4
Si4C2	40.7	41.1	41.7
Si4C3	41.4	40.9	42
Si4C4	41.8	41.3	41.4
Si4C5	41.7	41.1	41.6
Si4C6	41.2	40.5	41.4

Table 3: Weights of each DSC sample for different cooling rates. All weights are in mg

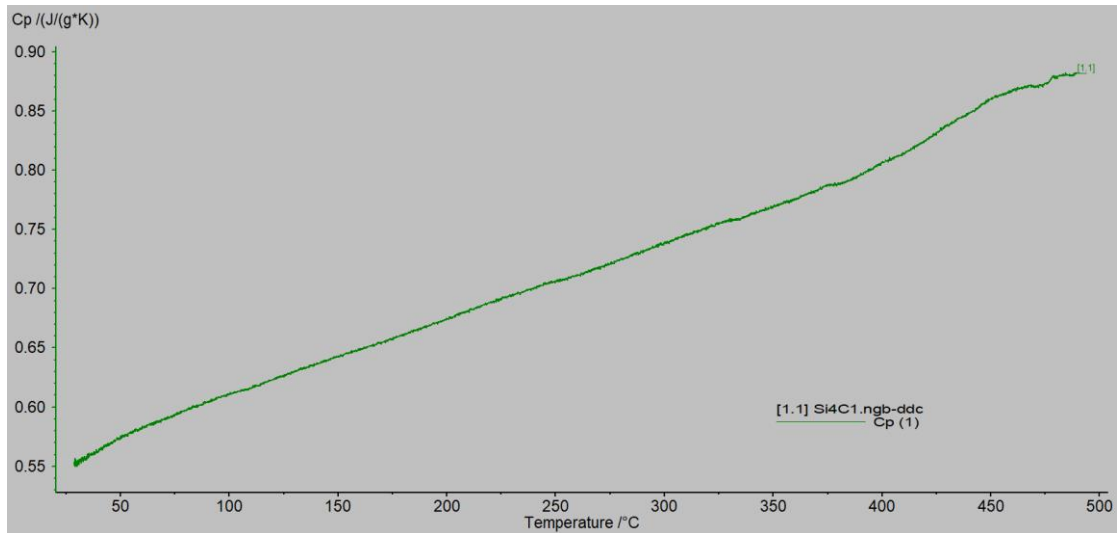


Figure 29: General trend of the Specific heat curve of the samples, considering only the heating part of the curve. The curve observed here is of Si4C1, for 30mm diameter. The reference standard is sapphire with a weight of 42.5mg.

3.4.2 Dilatometer:

The Dilatometer is an apparatus used to measure the length change phenomenon, the Thermal Expansion Coefficient, for the cast iron samples. Every time the material is exposed above a certain temperature limit, it undergoes a change in dimension. The substance either elongates or shrinks and this is a measure of the Thermal Expansion Coefficient [50]. Mechanical Dilatometry is the technique of placing a specimen in a closed environment of an inert gas (Helium) and heating up to a certain temperature range. The displacement of the specimen in the environment (expansion or contraction) is measured from one end of the specimen using a pushrod, connected to sensors. This test is generally approximate for materials with a general thermal expansion coefficient above $5 \times 10^{-6} \text{ K}^{-1}$. The general linear thermal expansion coefficient of grey cast iron is $10.5 \times 10^{-6} \text{ K}^{-1}$ [51], which makes it suitable to use this method. The pushrods are usually made of the vitreous silica type, the alumina type, or the isotropic graphite type. The most common one (as also used in the dilatometer in this experiment) is the Alumina type as they can withstand temperatures up to 1600°C [52].

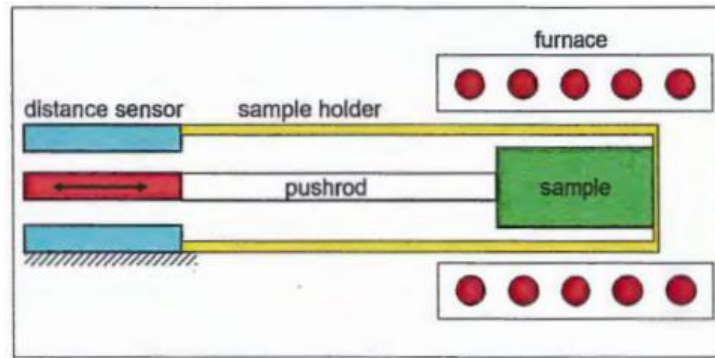


Figure 30: Principle of the Dilatometry [53]

As seen from figure (30) , the sample is placed in a sample holder, against an arrester on one end of the instrument. The pushrod touches the other end of the sample, which detects the mechanical displacement of the sample when heated and then transmits this displacement to a sensor, which measures it. The temperature in the furnace and of the sample is measured by thermocouples [53].



Figure 31: Dilatometer 402 C

The samples used in this experiment are of 6mm diameter, with an initial length close to that of the selected reference Al₂O₃ (Alumina) standard. The standard has a measured length of 12.5mm. hence the tolerance given for the length of the samples was ± 1 mm. The experiment starts by setting the atmosphere in the furnace and this is done by evacuating the furnace first, then filling it with Helium. This step is repeated thrice to ensure that the atmosphere is correctly secured in the furnace. The difference from DSC is that the atmosphere here is closed, meaning that there is no continuous flow of Helium, rather the chamber is filled with helium and the flow is stopped when the atmosphere is set inside the chamber. The flow of the purge (Helium gas) is controlled by a manual control system. The cast iron samples used in this experiment are heated up to 500oC and finally, it is subjected to cooling up to room temperature. The result obtains in this measurement was analyzed by using proteus analyzing software. The lengths of the various samples used for the experiment are given in the table (4).

Labels	30mm diameter	55mm diameter	80mm diameter
Si4C1	11.9	11.9	11.6
Si4C2	11.9	11.9	11.6
Si4C3	12	11.9	11.7
Si4C4	11.5	11.1	11.7
Si4C5	11.8	11.9	11.6
Si4C6	11.85	11.6	11.9

Table 4: Lengths of each Dilatometer sample for different cooling rates. All lengths are in mm.

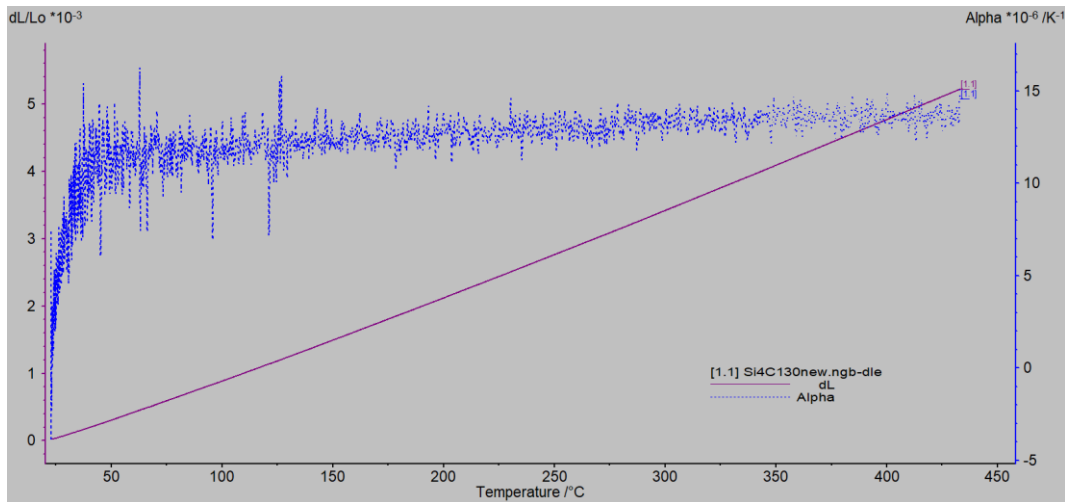


Figure 32: General trend of elongation v/s temperature of the samples. The scale of alpha (CTE) values is on the right axis. The curve observed here is of Si4C1, for 30mm diameter. The reference standard is Al_2O_3 with a length of 12.5mm.

3.4.3 Laser Flash

The laser flash methodology is widely used for accurately measuring the thermal diffusivity of the cast iron [50]. Two methods are generally used to measure the thermal diffusivity of a material- namely the guarded heat flow meter and the laser flash method. The Laser flash method is widely used owing to its non-contact, non-destructive methodology which requires no additional safety regulations [15]



Figure 33: Netzsch LFA 427 [15]

The samples have a diameter of 12.5mm and the accepted thickness range is 5mm to 6mm. The sample is first spray-coated with graphite, to enhance the emission or absorption capability of the sample and optimize the signal to noise ratio [54]. Then the atmosphere is set by evacuating the furnace and filling it with Argon gas. The atmosphere here is open, meaning a continuous flow of argon gas is required. The flow of argon is set to 125ml/min. Once the atmosphere is set, the voltage and number of laser pulses for each temperature rise is determined. Initially, the laser flashes of 480V are given at 25°C and 50°C. The rest of the temperatures are subjected to laser flashes of 450V. There are five shots fired for each specified temperature. The samples are heated up to 500°C and then subjected to cooling normally up to room temperature. The various thickness of the samples is provided in table (5).

Labels	30mm diameter	55mm diameter	80mm diameter
Si4C1	5.55	6.09	5.8
Si4C2	5.12	5.97	5.75
Si4C3	5.72	4.97	5.43
Si4C4	6.34	5.55	6.03
Si4C5	5.17	5.74	5.91
Si4C6	5.85	5.3	5.57

Table 5: Thickness of each Laser Flash sample for different cooling rates. All thicknesses are in mm

The increase of the temperature on the rear end face of the sample is observed and carefully measured using an Infrared detector and sensor. This temperature increase is correlated as a function of time. The software uses an Improved Cape-Lehman model, which considers multi-dimensional heat loss [55], to compute the thermal diffusivity. For an ideal case where there is no heat loss from the apparatus during any measurement, the thermal diffusivity can be correlated and calculated as:

$$\alpha = 0.1388 \cdot \frac{l}{t_{50}} [56]$$

where: l is the thickness of the sample

t_{50} is the time at which the temperature increase is 50%

α is the thermal diffusivity.

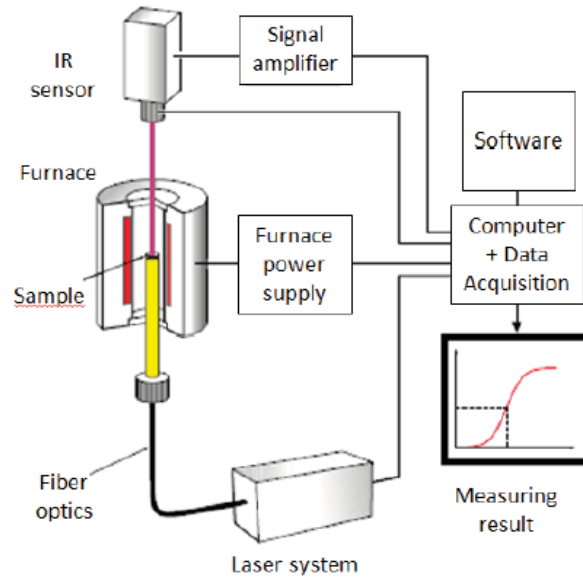


Figure 34: The Laser flash system and procedure [15]

After the values for the specific heat, thermal expansion coefficient, and thermal diffusivity were calculated and tabulated, the thermal conductivity was calculated for a temperature range from 25⁰C to 500⁰C, with an interval of 50⁰C.

3.5 Machined Tensile Samples:

The samples for the tensile tests were machined from one complete cylinder, for the 30mm diameter casts, and it was cut from the 55mm and the 80mm diameter casts (part 2 from figure (23)). The samples were of I-shape and they were milled using CNC controlled milling machine. The specifications are as shown in the figure (35). The thickness of each sample was determined depending on the eutectic cell size of each composition. For efficient determination of the mechanical properties, the thickness of each sample should be at least thrice the maximum eutectic cell diameter. However, for the 4% Si compositions, it was hard to distinguish and determine the eutectic cell boundaries. An alternative method adopted was to measure the length of the largest graphite flake. This was because the eutectic matrix structure basically is the eutectic surrounded by the graphite flakes around the border, making up one eutectic cell. The largest graphite flakes were around 700 μ m to 1000 μ m. Hence the thickness of the tensile samples was decided to be around 3mm each. The milled extruded piece was cut into the desired samples with an EDM cutter, which were performed outside the limits of the University. Once the samples were milled and machined, they were polished and grinded using the flat grinding machine. This is done to prevent the presence of any stress concentrators which may act as active sites for the breakage of the sample during the tensile tests. These unnecessary sites of crack do not give the original tensile

characteristics of the sample as the crack propagates and breaks due to these stress concentrators and not due to the morphology of the sample. The samples are expected to break by the neck area, which is the gauge area of length 12mm. The two ends are grips provided to support the samples onto the tensile rig.

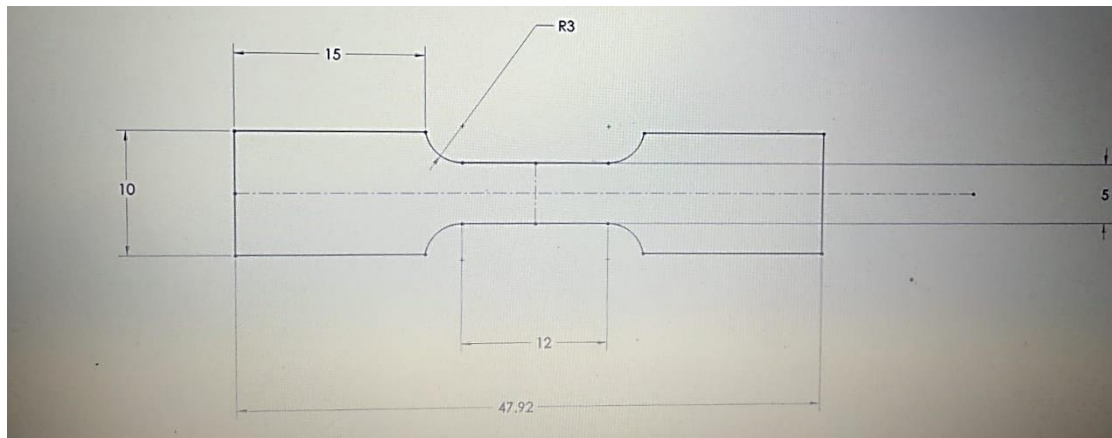


Figure 35: Specifications of the Tensile sample



Figure 36: Machined Tensile sample

3.6 Tensile Tests:

The tensile tests are carried out in the Zwick/Roell Proline Z100 Ultimate tensile rig. . This is a good alternative as the force is transmitted through a central ball-lead screw, meaning that there is a good flow to the force. Moreover, the grips are aligned axially and linearly, ensuring a straight flow of force while pulling the samples, avoiding the effect of torsion or skewing on the samples [57]

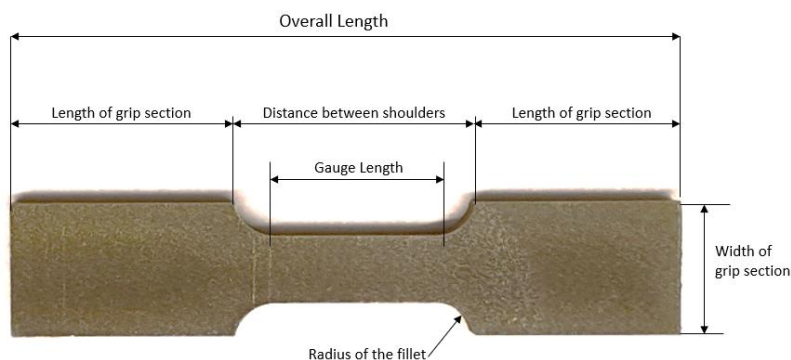


Figure 37: Nomenclature for an I shaped tensile sample

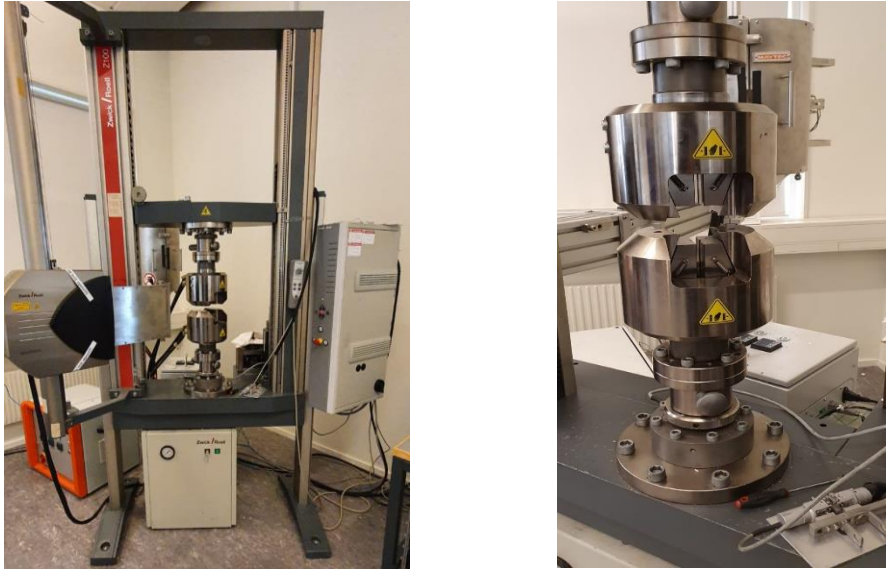


Figure 38: the Zwick/Roell Z100 Ultimate Tensile rig and the hydraulic grips to hold the sample

The samples were I-shaped, with a thickness of 3mm, and were originally machined to be tested in the miniaturized tensile rig (MTS). However, due to the increased sample count and the high sensitivity of the MTS rig, the Zwick/Roell Proline Z100 Ultimate tensile rig was chosen as the alternative. The MTS was thus kept as a standard to compare the results obtained from the ultimate tensile rig. However, the results from the ultimate tensile testing rig deemed satisfactory when compared to those obtained from the miniaturized tests. The table (9) shows the maximum tensile strengths obtained from the UTS and the MTS for one sample from the highest and lowest cooling condition. The ends were placed between grooved wedged grips for samples of thickness between 0mm to 9.5mm, as seen from figure (40). the pulling rate was set to 0.01mm/s and the grip pressure was placed at 50 bar. Six samples were cut for each composition, and at least three of them were broken to get a good consistency in the results. There isn't much variance between the values calculated. All the specimens were checked primarily for surface porosities which could act as potential sites for stress concentration before mounting them onto the rig. Once the samples were placed in position after making sure that the samples were aligned parallel to the force axis, the external forces were set to equilibrium or zero and then pulled to avoid unnecessary addition of pull to the sample. The tensile strength for consecutive pulling is recorded on a graph which shows the force to the elongation. The maximum tensile strength was measured and from all six samples which were broken for each composition, the most consistent of them were chosen as the optimal value.



Figure 39: Sample after tensile testing.



Figure 40: The groove wedge used to hold the samples in grip

3.7 Sample Etching:

The final properties of a cast material are solely determined by its microstructure. Hence, to further understand the thermal and mechanical properties of the samples, selective color etching (also called Tint etching) was used. This was the preferred method as the samples have 4% Si, which segregates, and a reagent sensitive enough to reveal this segregation in the microstructure is used [58]. Color etching gives an accurate distinction between the phases and shows the segregation more clearly. This report uses an etching reagent which produces a film on the surface of the specimen, which tints the different phases in different colors enabling a good metallographic analysis. The different shades produced depend on the film thickness and are due to the light interference effect [58]. The film formed on top of the surface is usually between 0.04-0.5 μm , and they mainly consist of oxides, sulfides, complex molybdates, which give different hues depending on the amount of interference [59].

The silicon that segregates reveals the austenite pattern in the microstructure. The etchants used to form silicon oxide films, which by the light interference effect, is used as the medium to view the microstructure of the austenite produced before the eutectoid transformation. The film produced doesn't affect the polished surface of the specimen [58]. The samples were hot mounted, ground and polished, then etched and viewed through the microscope.

3.7.1 Sample Mounting:

This is the first step that is carried out before the samples are etched. The tensile samples which were broken from the tensile tests were used to observe the microstructure. The samples were hot mounted using the Multifast black resin. The apparatus used for this operation is the Struers Citopress-1. Multifast black is a thermosetting black bakelite mounting resin with wood filler [60]. This resin was chosen as it has a medium shrinkage rate and a medium removal rate after the embedding is done. This resin is used for medium to hard materials and is suitable for etching and microscopic evaluation [60]. The mounts were 50mm in diameter. According to the process parameters specified by Struers, 70ml of multifast resin is used to mount one sample. The heating time is set to 7 minutes at a temperature of 180°C, with a pressure of 250 bar. The cooling time after the resin is set is for 6 minutes, and the cooling rate is high. The total time thus required to mount one sample is 13 minutes.



Figure 41: Struers Citopress used to embed the specimen [61]

3.7.2 Grinding and Polishing:

After the samples are embedded, they are ground and polished to attain a polished mirror surface that is subjected to etching. The mounted samples were grinded using a Mecapol P 310 VV machine, which uses SiC foils, with a PET foil backing for the grinding. These are the best for wet grinding operations. Grit 80, grit 220, grit 500, grit 800, grit 2000, and grit 4000, each foil with a diameter of 250mm. Caution must be taken to reduce the number of grinding and polishing stages as excess exposure to these processes could pull out the graphite flakes from the microstructure. Rough abrasives could often remove the matrix material close to the graphitic interfaces, which may further rupture the graphite itself. This usually results in cavities where the graphite flakes had been in. Hence, SiC papers are preferred owing to their improved grinding properties and less damage [62].

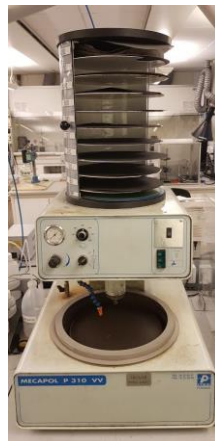


Figure 42: Mecapol P 310 VV apparatus used for the wet grinding

After the coarse wet grinding is performed, automated polishing of these specimens is carried out with the Struers Tegramin-30. This is done to remove any small debris present on the sample during the coarse grinding and obtain a mirror surface for etching. The steps followed for performing this automated polishing are shown in the figure (44). The suspension used for the initial step is the DiaPro Dac3, which is a stable water-based diamond suspension having diamond particles of $3\mu\text{m}$. This is used with MD-Dac, the polishing cloth which can be used for polishing all materials using diamond particles between $3\mu\text{m}$ and $9\mu\text{m}$. This polishing is carried out for 5 minutes. The next step uses the MD-Nap polishing cloth, which is used for the final polishing of all materials. The suitable suspension used is the DiaPro Nap-B1, which is commonly used for the metallographic polishing of hard materials, with diamond particles of $1\mu\text{m}$ [60].

This polishing step is carried out for 2 minutes. The surface after these steps seemed to be well polished, with very few scratches. Care was taken to observe the surface of the specimen under an optical microscope after each step to see if the graphite flakes were not pulled off.



Figure 43: Struers Tegramin-30 used for the fine polishing [63]

Surface	Suspension	Lub.	Time/ μm
1 Dac	DiaP. Dac3		5:00 min
2 Nap	DiaP. Nap-B1		2:00 min
3 New step			

Figure 44: steps used for the automated polishing in Struers Tegramin-30

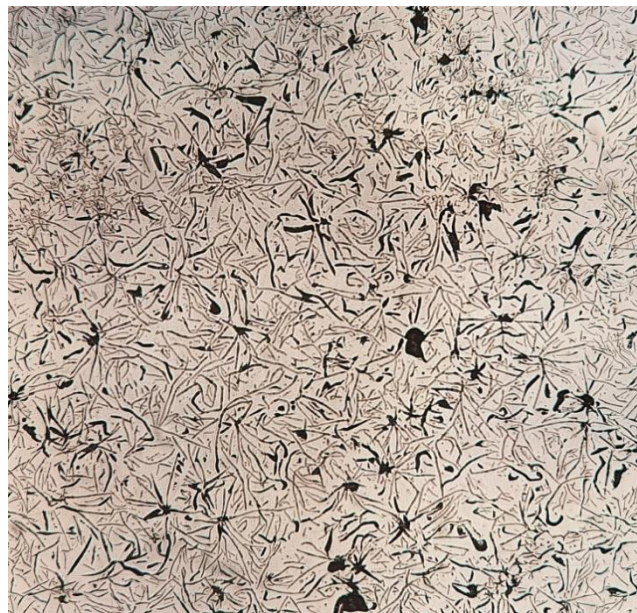


Figure 45: The graphite flakes as seen after the grinding and polishing of the sample. The flakes are very visible and no cavities were seen because the flakes were not ripped off.

3.7.3 The etchant used and Procedure for Etching:

The method used for color etching is the picric etching method. The etchant used is a solution of 10g picric acid, 10g sodium hydroxide (NaOH), 40g potassium hydroxide (KOH), and 50ml of picric acid. The process of etching is carried out between 90°C and 110°C. The effective etching was seen at 110 °C and the etching time required was around 2 minutes, at this temperature. There was a lag during the heating, and it was difficult to hold the temperature of the picric etchant at 110 °C. Thus, after initially attaining the required maximum temperature, the rest of the samples were etched on an average of 4 to 6 minutes, at a temperature of 104 °C to 106 °C. The etching was carried out in steps of 1 to 2 minutes to prevent over-etching on the surface. A perfectly etched surface has a visible color film that is in the blue region when viewed with the eye. An over etched surface tends to have a greenish-blue hue to the film produced and an under-etched surface has a yellow tinge on it. If perfect etching was not observed, the samples were once again ground and polished for consequent etching, taking care not to damage the graphite flakes in the microstructure. The solution needs to be stirred continuously and a thermocouple introduced in the solution records the temperature. High care and attention must be taken while handling picric acid as it is toxic if inhaled, has any



contact with the skin, or if consumed. It is highly explosive if subjected to friction fire or any kind of spark or ignition [58].

Figure 46: The broken tensile sample after mounting, polishing, and etching. This is well etched as the hue of the film on top of the surface is blue.

3.8 Microstructural Analysis:

The microstructure of the specimen was viewed and observed using the Olympus GX71F optical microscope. All the micrographs required for the analysis was taken with a 10x magnification. The color etched micrographs were used to analyze the fraction of primary austenite and the hydraulic diameter of the interdendritic region. This was made possible by converting the micrographs to binary images. This was done using the software Adobe Photoshop and a Wacom Cintiq interactive display to draw over the micrographs and create the ternary image. This operation was performed manually. From the binary image drawn, the red area is the dendrites seen and the white region is the interdendritic area. The fraction of primary austenite was quantitatively

calculated using the Olympus Stream Motion Desktop software 1.9.1, from the binary images. The perimeter (P_γ) and the area (A_γ) of the primary dendrites were measured to calculate the hydraulic diameter ($D^{\text{HYD}}_{\text{IP}}$) and the mean area fraction of the dendritic region.

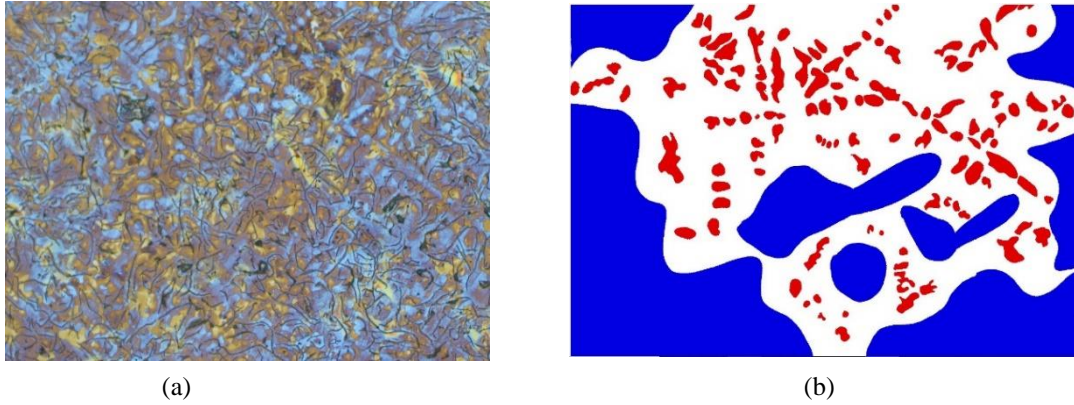


Figure 47: (a) Micrograph obtained after color etching and (b) its corresponding binary image. The sample considered is Si4C6, for the 55mm diameter cast.

4 Findings and Analysis

4.1 Thermophysical Properties

This section gives a detailed overview of the results obtained from the thermophysical tests. The thermal conductivity of the samples was calculated manually for each chemical composition, after calculating the specific heat capacity, thermal expansion coefficient, and thermal diffusivity of each sample.

4.1.1 Specific Heat Capacity:

The specific heats for the different samples with the three different cooling rates are as seen in figures (48), (49) and (50).

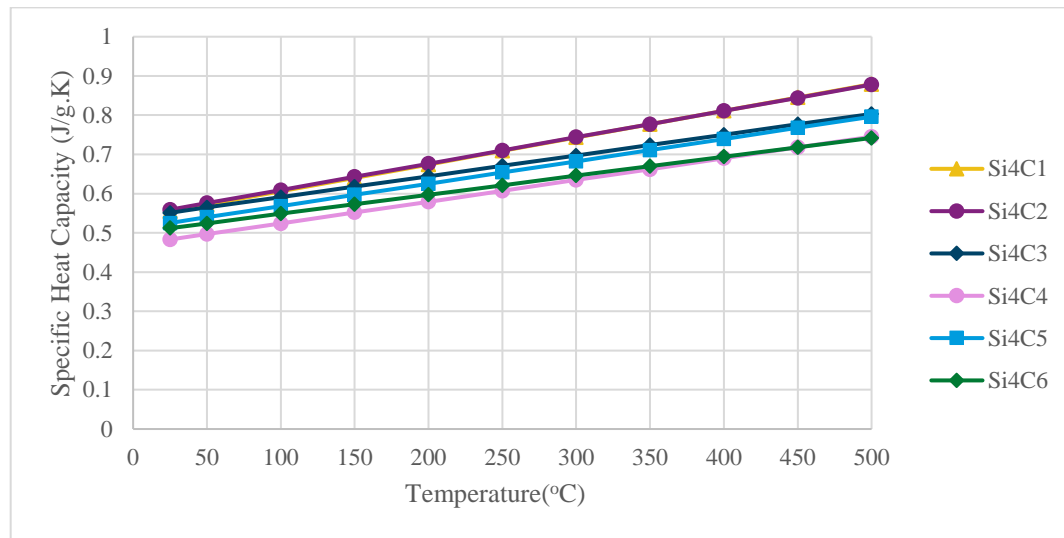


Figure 48: Specific heat capacity v/s temperature for highest cooling rate (30mm). Si4C1 follows the same trend as Si4C2 and is hidden behind the curve for Si4C2.

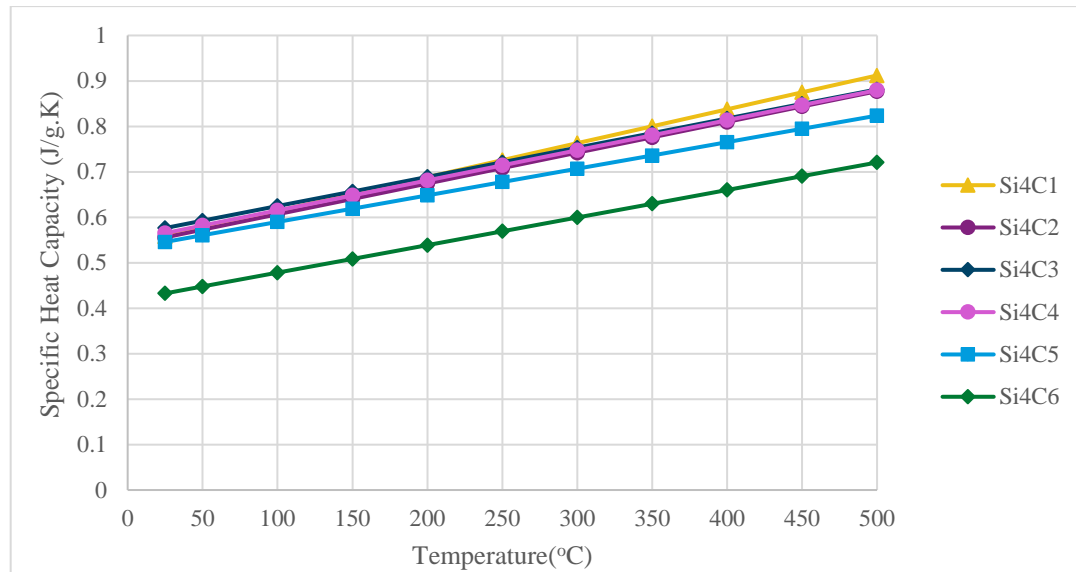


Figure 49: Specific heat capacity v/s temperature for moderate cooling rate (55mm). Si4C2, Si4C3 and Si4C4 follows the same trend and hence they overlap.

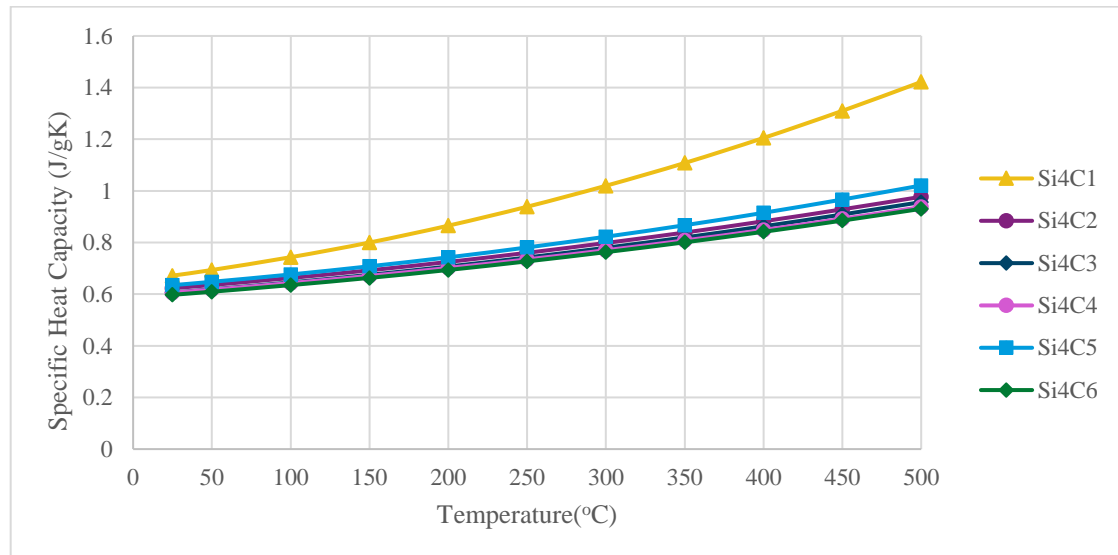


Figure 50: Specific heat capacity v/s temperature for slow cooling rate (80mm). Si4C2, Si4C3, Si4C4, Si4C5 and Si4C6 seems to overlap each other.

Observing the curves from figures (48), (49) and (50), the specific heat capacity increases with an increase in temperature, for all cooling rates. The hypereutectic composition Si4C1 has the highest specific heat capacity of all the compositions, which maybe due to the highest carbon content. The specific heat is highest for the casts with the slowest cooling rate (the 80mm diameter casts). However, the 30mm and 55mm diameter casts have more or less similar values for the specific heat at room temperature and it remains consistently similar even when the temperature is increased to 500°C (as seen from table 1 in Appendix 1). There is a difference of at least 0.1 J/ (g.K) between the slowest cooling rate and the medium and high cooling rates. The hypereutectic composition Si4C1, with the slowest cooling rate, has the highest specific heat at 500°C.

4.1.2 Thermal Expansion Coefficient:

The thermal expansion coefficients for the different compositions with varying cooling rates are as seen from figure (51), (52) and (53).

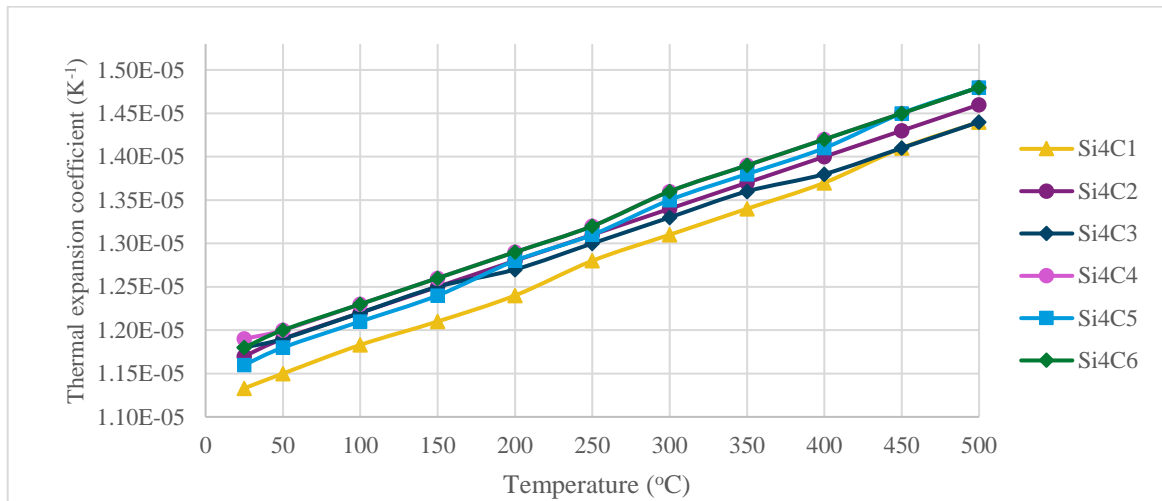


Figure 51: Thermal expansion coefficient v/s temperature for high cooling rate (30mm). All the curves are observed to be very close to each other or overlap, making it difficult to differentiate between each trend.

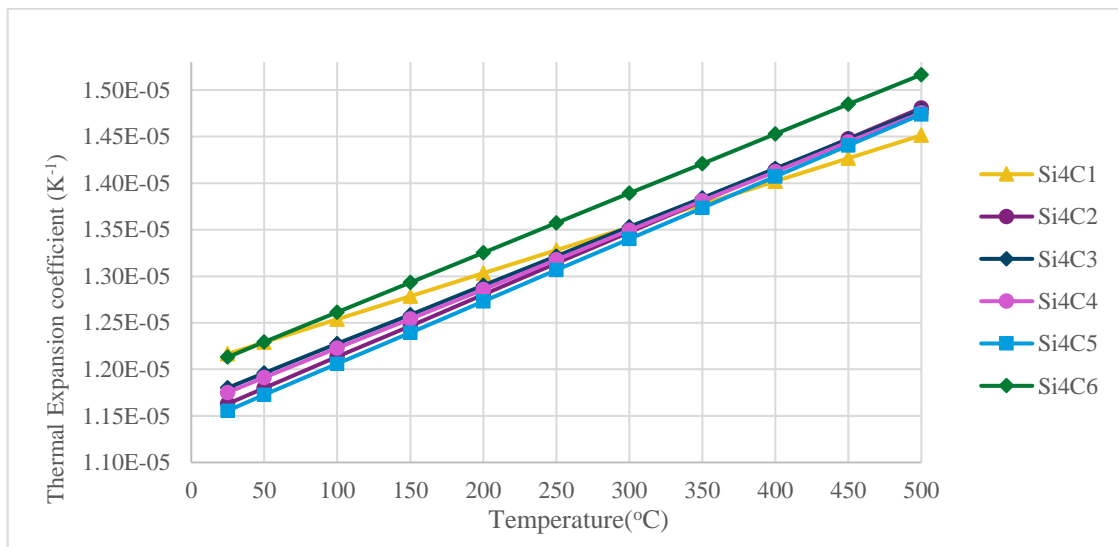


Figure 52: Thermal expansion coefficient v/s temperature for medium cooling rate (55mm). All the curves are observed to be very close to each other or overlap, making it difficult to differentiate between each trend.

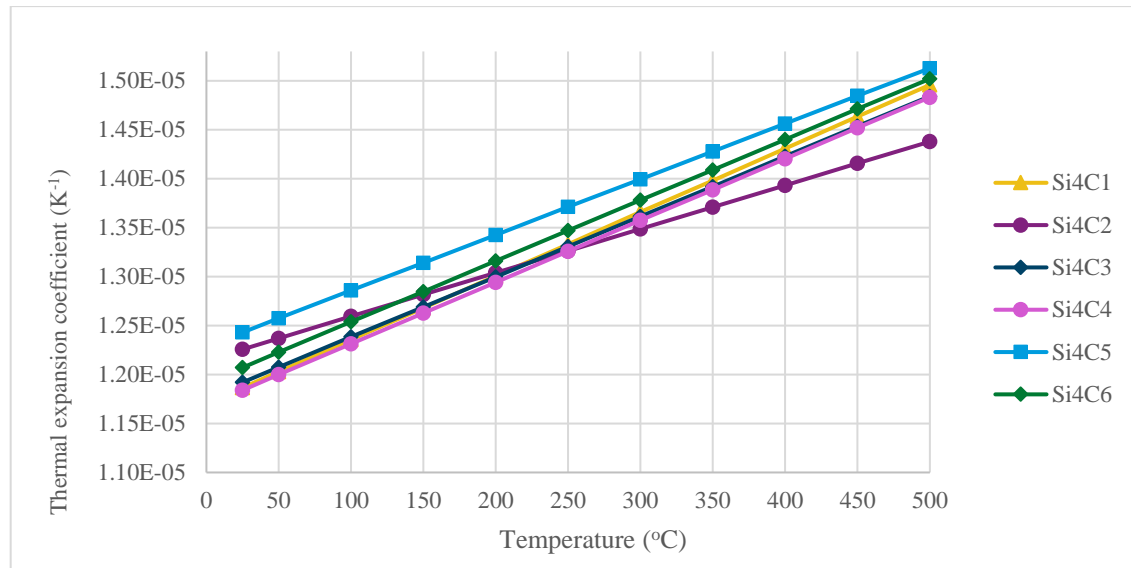


Figure 53: Thermal expansion coefficient v/s temperature for slow cooling rate (80mm). All the curves are observed to be very close to each other or overlap, making it difficult to differentiate between each trend.

It can be noticed from the curves that for all the cooling rates, the thermal expansion coefficient values show an increasing trend with an increase in temperature. Moreover, for all the cooling rates, the alpha values seem to lie between $1.13E-05$ and $1.52E-05$ K^{-1} , as seen from table (2) from Appendix 1. It can be concluded from the figures (51), (52) and (53) that the chemical compositions and the varied cooling conditions have little or no effect on the thermal expansion coefficient. At the elevated temperatures, there is a maximum difference of ± 0.02 K^{-1} .

4.1.3 Thermal Diffusivity:

The thermal diffusivity of each composition at varying cooling rates is as shown in figure (54), (55) and (56).

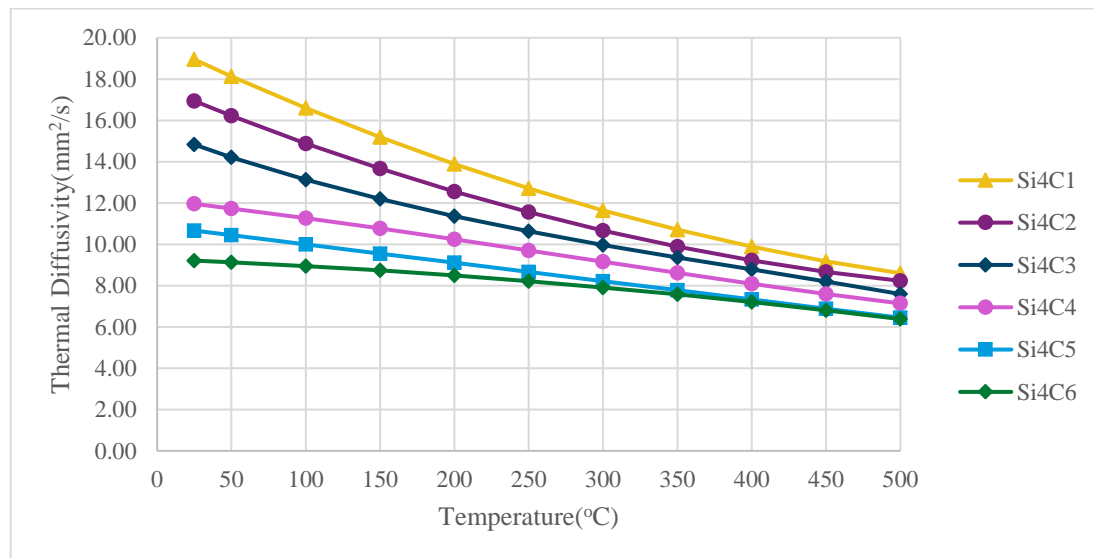


Figure 54: Thermal diffusivity v/s Temperature for high cooling rate (30mm)

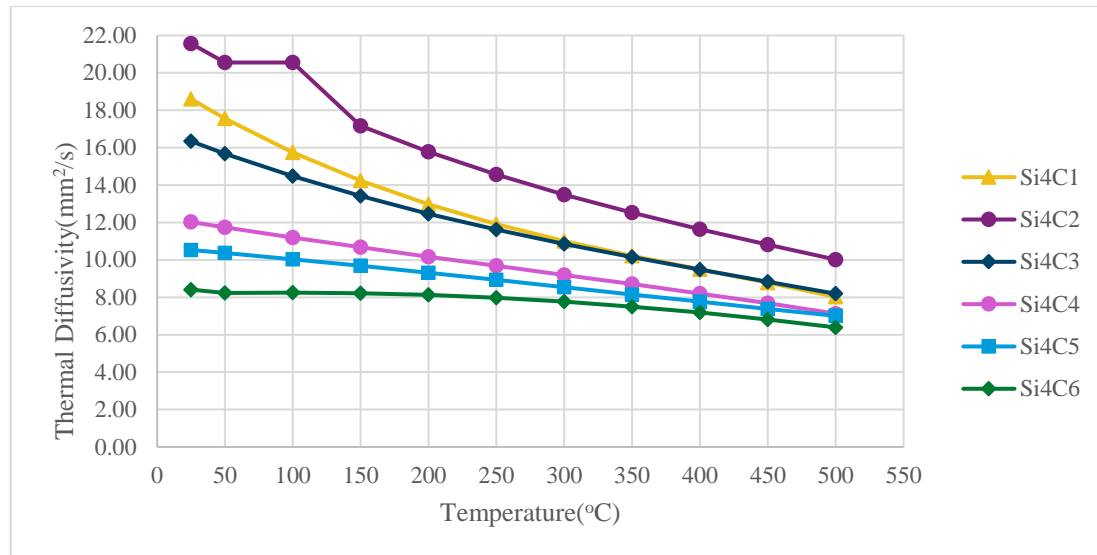


Figure 55: Thermal diffusivity v/s Temperature for medium cooling rate (55mm)

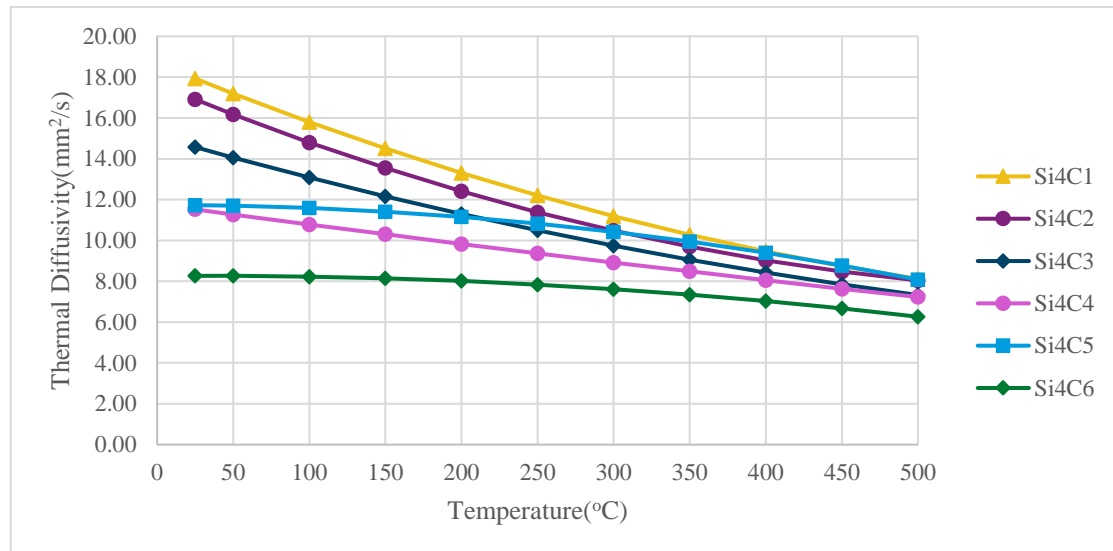


Figure 56: Thermal diffusivity v/s Temperature for slow cooling rate (80mm)

The thermal diffusivity is calculated for the discrete temperatures between 25 °C and 500 °C, with an interval of 50 °C. The values plotted are the average of the five shots that were fired at the specified temperatures. The tabulated values of the thermal diffusivity at all three cooling conditions can be seen from tables (3), (4) and (5). The standard deviations seem to be quite low, meaning that the thermal diffusivity values measured from all five shots at a certain temperature seemed to have little variations with each other. As seen from the curves from figures (54), (55) and (56), there is a steady decrease in the thermal diffusivity with increasing temperature. This decrease also seems to be larger when the carbon content is higher. The composition with the lowest carbon content have the lowest value of thermal diffusivity. The range of values for thermal diffusivity is more or less the same for all the cooling rates. However, as opposed to the usual trend, comparing the hypereutectic compositions Si4C1 and Si4C2 for the medium cooling rate, Si4C2 has a higher value of thermal diffusivity than C1 (figure(55)), although C2 has a lower carbon content than C1. A similar anomaly has been observed in the slow cooling rate samples Si4C4 and Si4C5. It can be added that

the chemical composition seems to have a greater effect on the thermal diffusivity at lower temperatures.

4.1.4 Thermal Conductivity:

The summarized thermal conductivity for the 4% Si compositions for all three cooling rates are as shown in figure (57), (58) and (59).

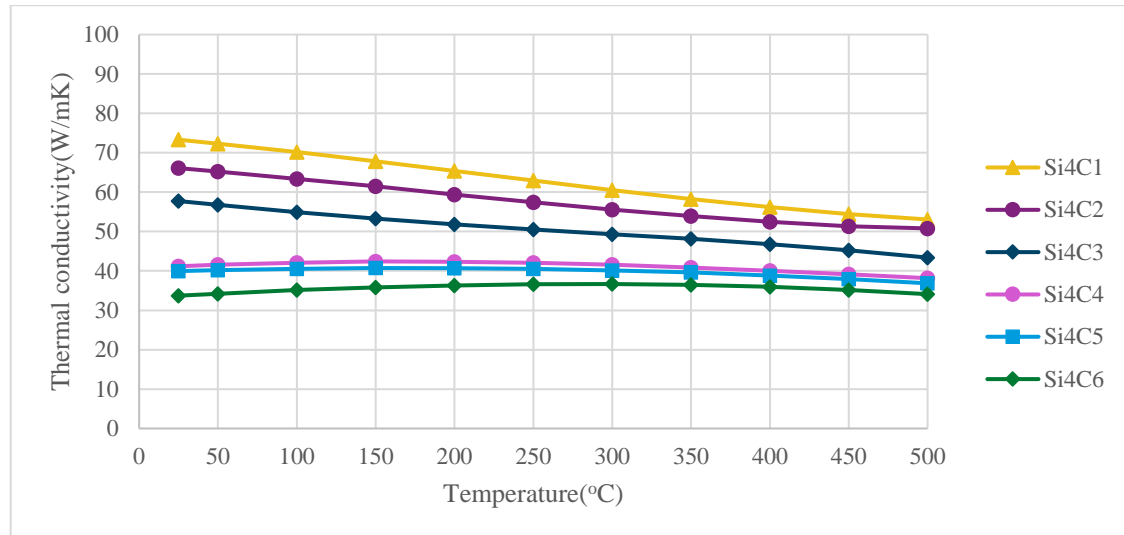


Figure 57: Thermal conductivity v/s temperature curve for high cooling rate (30mm)

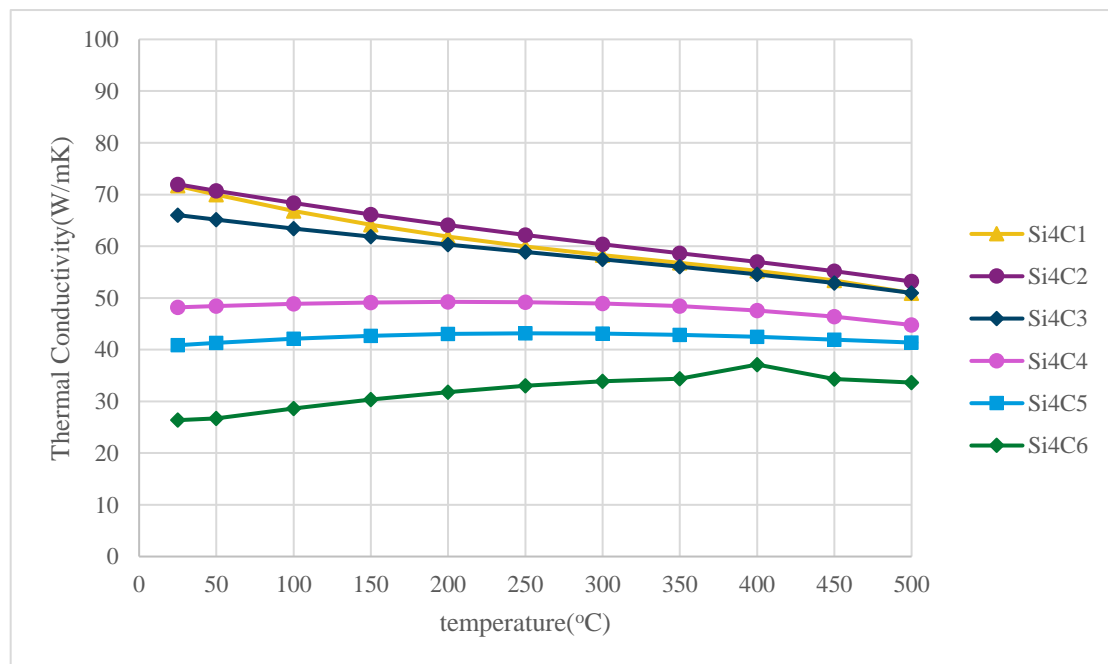


Figure 58: Thermal conductivity v/s temperature curve for medium cooling rate (55mm)

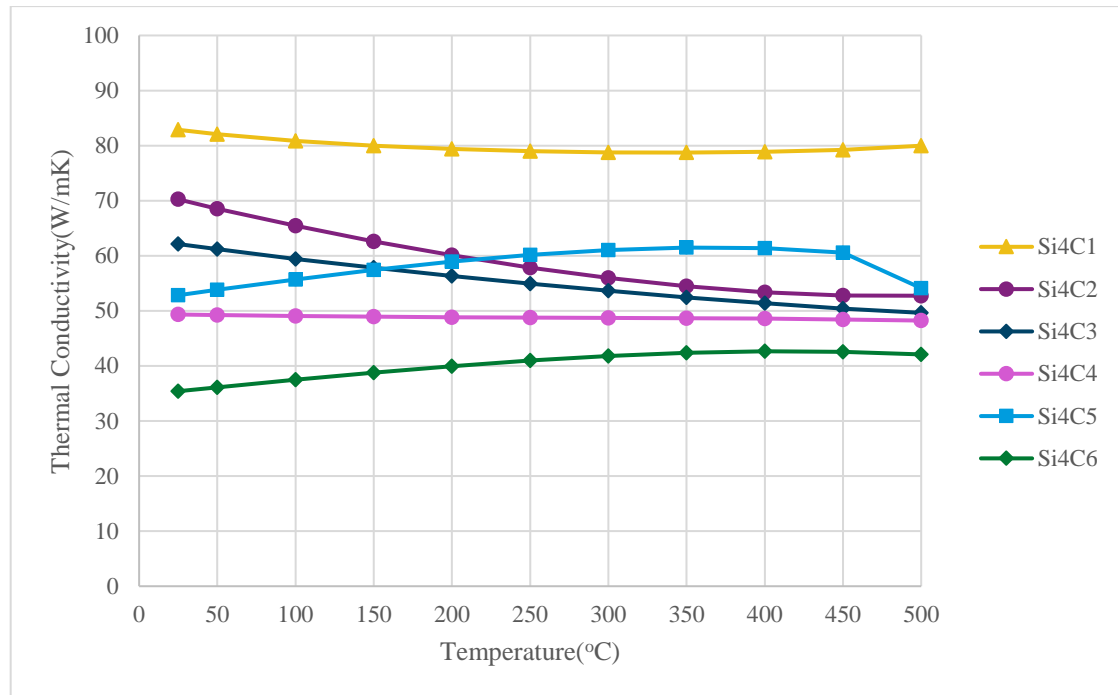


Figure 59: Thermal conductivity v/s temperature curve for slow cooling rate (80mm)

For the high cooling rate cast, the hypereutectic samples (Si4C1 and Si4C2) seem to have a constant steady decreasing trend in the thermal conductivity with an increase in the temperature. The Eutectic sample (Si4C3) has the same decreasing trend, and the maximum conductivity was seen at room temperature, 25°C. The three hypoeutectic samples (Si4C4, Si4C5, and Si4C6) have a rather increasing trend till 150°C and then it slightly decreases. For the medium cooling rate casts, the thermal conductivity shows a general decreasing trend for the hypereutectic and the eutectic compositions. For the hypoeutectic samples, the thermal conductivity increases to a maximum and then decreases. The maximum thermal conductivity observed was between 200°C and 400°C. For the slow cooling rate, the thermal conductivity decreases with decreasing carbon content. However, Si4C5 has higher thermal conductivity than Si4C4, although there is lesser carbon content. The hypereutectic and the eutectic samples have the maximum thermal conductivity at room temperature, whereas the hypoeutectic samples have the maximum value between 350 °C and 400 °C.

Previous literature [40] showed that there was a difference of 30 W/(mK) between the high carbon casts with medium (sand casted) and low cooling (cast with insulation) rates and that with a high cooling rate (chill metal cast). However, the results here show a 10 W/(mK) difference between the same, which is not considerably much. Moreover, the trend of the hypoeutectic compositions to increasing to a maximum and then decreasing is similar to the general trend of the thermal conductivity for hypoeutectic casts with 1 to 3% Si, where the thermal conductivity reaches a maximum at about 400 °C and then drops [40].

4.2 Ultimate Tensile strength:

This section will give a brief analysis of the results obtained from the tensile test and examine its relationship with other parameters like carbon equivalent and hydraulic diameter.

4.2.1 Tensile strength as a function of Carbon Equivalent:

Table (6) show the measured values of engineering tensile strength for six different carbon equivalent and three different cooling rates of diameter 30mm (Highest cooling condition), 55mm (Moderate cooling condition), and 80mm (Lowest cooling condition).

Compositions	Silicon Content	Measured Carbon equivalent	Tensile strength for 30mm Dia (Mpa)	Tensile strength for 55mm Dia (Mpa)	Tensile strength for 80mm Dia (Mpa)
Si4C1	4%	5.16	113.15	103.21	99.45
Si4C2	4%	4.64	129.50	90.90	82.49
Si4C3	4%	4.28	166.77	147.16	119.53
Si4C4	4%	4.03	203.95	188.05	133.12
Si4C5	4%	3.85	232.95	201.28	151.81
Si4C6	4%	3.66	242.48	232.92	145.38

Table 6: The measured value of tensile strength for six different C.E and three different cooling conditions

According to the tabulated values, a graph was plotted between the carbon equivalent and the tensile strength shown in figure (60). From the graph, it can be observed that it follows the general trend in which the tensile strength increases with a decrease in carbon equivalent. However, the composition Si4C2 does not follow the general trend, it shows a lower strength compared to the composition Si4C1 even though Si4C2 has a lower carbon equivalent than the composition Si4C1. This trend can only be observed in 55mm diameter (Moderate cooling condition) and 80mm diameter (Lower cooling condition). Moreover, another important fact which can be observed is that the tensile strength decreases as the cooling condition gets lower. The diameter with 80mm (Lower cooling condition) has the least strength in all the six compositions compared to other cooling conditions.

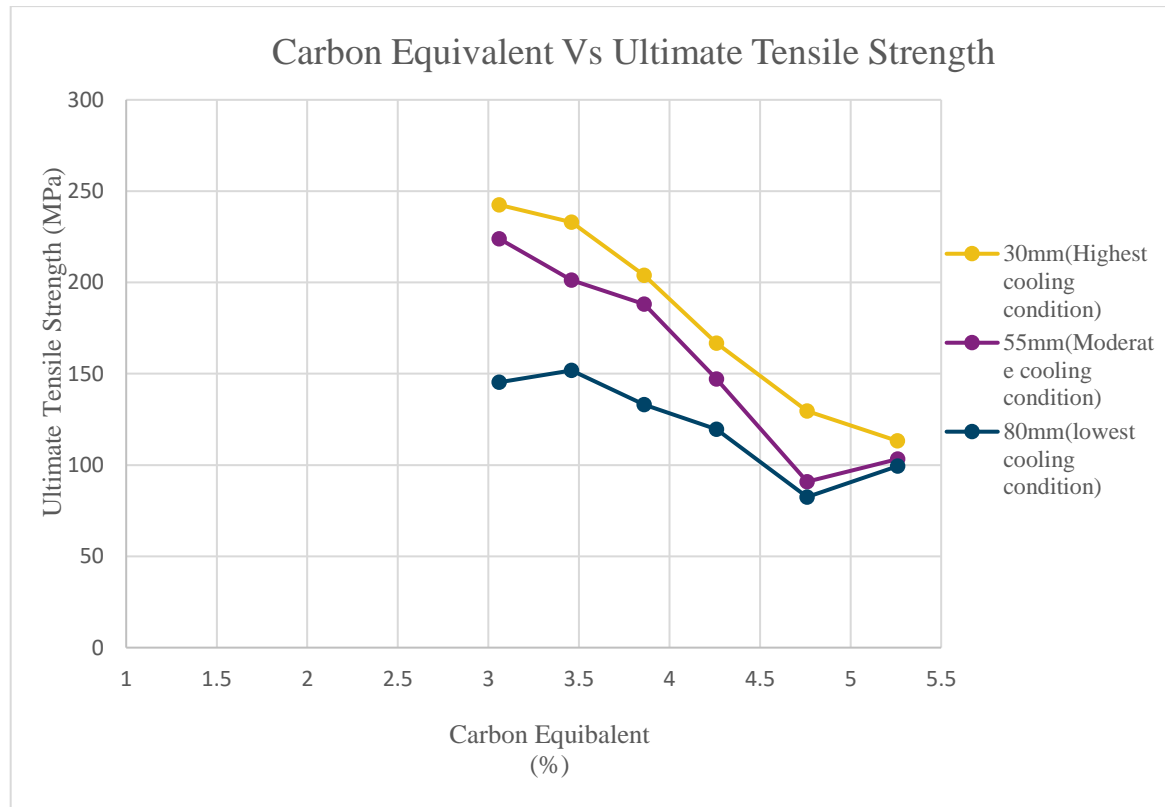


Figure 60: Influence of carbon equivalent on tensile strength

The maximum tensile strength achieved in the 4% silicon is close to 250 Mpa for the hypoeutectic cast of higher cooling rate with carbon equivalent 3.66% shown in figure (60). But the previous literature (High carbon equivalent) reveals that the maximum strength obtained for the hypoeutectic cast with carbon equivalent 3.34% is 350 to 400 Mpa when the silicon content is between 1-3%, which shows that the measured tensile strength in the present work with 4% silicon is lower than the strength observed in the previous literature.

4.2.2 Correlation between Tensile Strength and Hydraulic Diameter

This section will give a detailed analysis of how hydraulic diameter influences the ultimate tensile strength and how its related to the area fraction of dendrites.

Table (7) shows the measured hydraulic diameter and the mean area fraction of dendrites for all the six compositions with the carbon equivalent varying from 5.26% to 3.06.

Casting Diameter	Compositions	Measured Carbon Equivalent (%)	Mean fraction of dendrites	Hydraulic Diameter (μm)
30mm	Si4C3	4.28	0.11	37.96
	Si4C4	4.03	0.21	16.04
	Si4C5	3.85	0.30	13.28
	Si4C6	3.66	0.35	7.27
55mm	Si4C1	5.16	0.24	17.75
	Si4C3	4.28	0.31	16.54
	Si4C4	4.03	0.45	11.19
	Si4C6	3.66	0.49	9.05
80mm	Si4C1	5.16	0.35	14.74
	Si4C3	4.28	0.46	12.36
	Si4C4	4.03	0.62	9.25
	Si4C5	3.85	0.70	7.65
	Si4C6	3.66	0.81	5.62

Table 7: Measured hydraulic diameter and mean area fraction of dendrites for all six compositions at three different cooling conditions

From table (7), it is evident that the reduction of carbon equivalent and the increase of the mean area fraction of dendrites contributes to an decrease of hydraulic diameter in all three cooling rates, this is because when the carbon equivalent reduces (lower carbon content) the amount of dendrites formed will be higher leading to reduced interdendritic space, hence the hydraulic diameter decreases. Moreover, another fact that can be observed is that the cooling condition has linear relationship with the hydraulic diameter. Another observation is that the dendrites were difficult to differentiate from the eutectic found in hypereutectic samples Si4C1 and Si4C2 for the 30mm dia (highest cooling condition) which is shown in figure (61). As a result, it was difficult to measure the hydraulic diameter and the area fraction of austenite in those samples.

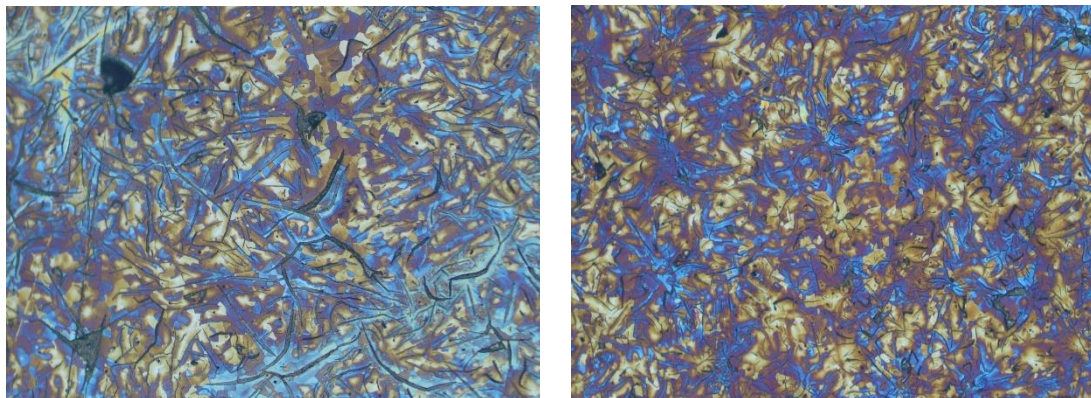


Figure 61: Hypereutectic composition of 30mm diameter (high cooling rate) with no dendrites observed

Figure (62) shows the relationship between the ultimate tensile strength and the hydraulic diameter, and it also shows the type of graphite flakes formed in all three cooling conditions. It is found that there is an inverse relationship between the ultimate tensile strength and the hydraulic diameter. For the highest cooling condition (30mm dia), the eutectic sample Si4C3 has the highest hydraulic diameter which in turn contributes to the less tensile strength of the sample. This indicates that it follows the general trend which is discussed in the literature [8]. Moreover, there is a difference of 17 (μm) in hydraulic diameter between the eutectic sample Si4C3 and hypoeutectic

sample Si4C4 of casting diameter 30mm (high cooling condntions). While for the reaming cooling conditions the difference in the hydraulic diameter is not that prominent. On the other hand, for the 80mm casting diameter (lowest cooling condition), it is evident that it has the lowest tensile strength compared to other cooling conditions. The measured values of hydraulic diameter and the tensile strength for different cooling conditions are tabulated and shown in table (8).

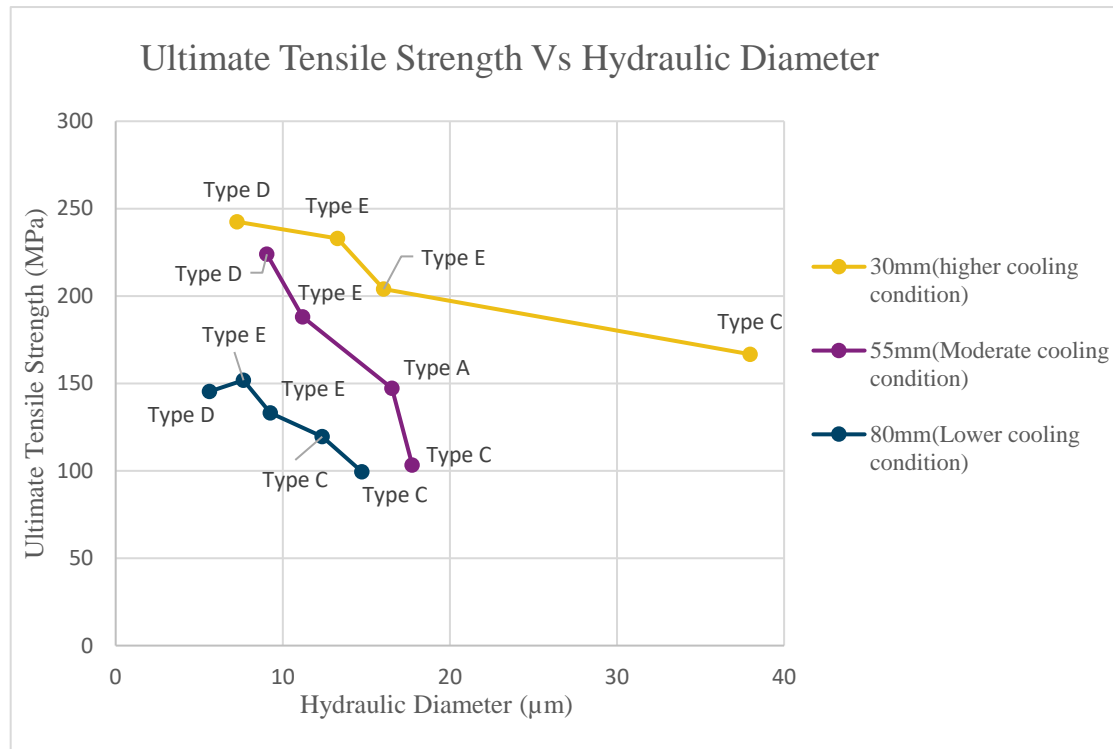


Figure 62: Influence of Hydraulic diameter on tensile strength

Casting Diameter	Compositions	Measured Carbon Equivalent (%)	Hydraulic Diameter (µm)	Tensile Strength MPa
30mm	Si4C3	4.28	37.96	166.7
	Si4C4	4.03	16.04	203.95
	Si4C5	3.85	13.28	232.95
	Si4C6	3.66	7.27	242.48
55mm	Si4C1	5.16	17.75	103.21
	Si4C3	4.28	16.54	147.16
	Si4C4	4.03	11.19	188.05
	Si4C6	3.66	9.05	223.92
80mm	Si4C1	5.16	14.74	99.45
	Si4C3	4.28	12.36	119.53
	Si4C4	4.03	9.25	133.12
	Si4C5	3.85	7.65	151.81
	Si4C6	3.66	5.62	145.38

Table 8: Measured values of hydraulic diameter and tensile strength for varying C.E at three different cooling conditions

4.3 Color Etched Micrograph Analysis

The etched microstructure images of three different cooling conditions such as 30mm (Higher cooling conditions), 55mm (Moderate cooling conditions), and 80mm (Lower cooling conditions) are shown in figures (63), (64), and (65). From the microstructure, in all the cooling conditions, as the carbon equivalent decreases it can be observed that the graphite morphology changes from type A to type E, and the flakes became finer with reduced carbon content. Moreover, the flakes for the low carbon content seems to be present and concentrated in the inter dendritic space, owing to the higher fraction of primary dendrites.

Another common trend we observed in the microstructure for all the three different cooling conditions is the color of the dendrites, in samples with high carbon equivalent the color of the dendrites found to be blue. While dendrites with yellowish-brown color with blue colored boundaries are observed in the low carbon equivalent samples and it is predominantly seen in hypoeutectic composition with a very low carbon equivalent.

The type of graphite flakes formed in all three cooling conditions can also be observed in Figures (63), (64), and (65). From the microstructure, it is evident that the hypereutectic and eutectic composition in all the three different cooling conditions contains type A and type C graphite flakes. While the hypoeutectic composition in all the three different cooling conditions exhibits the type E and type D graphite flakes. Moreover, type D graphite flakes are predominantly observed in hypoeutectic composition with very low carbon content. In order to get an overview about the type of graphite flakes formed in all the compositions at all the three cooling conditions are shown in appendix table ().

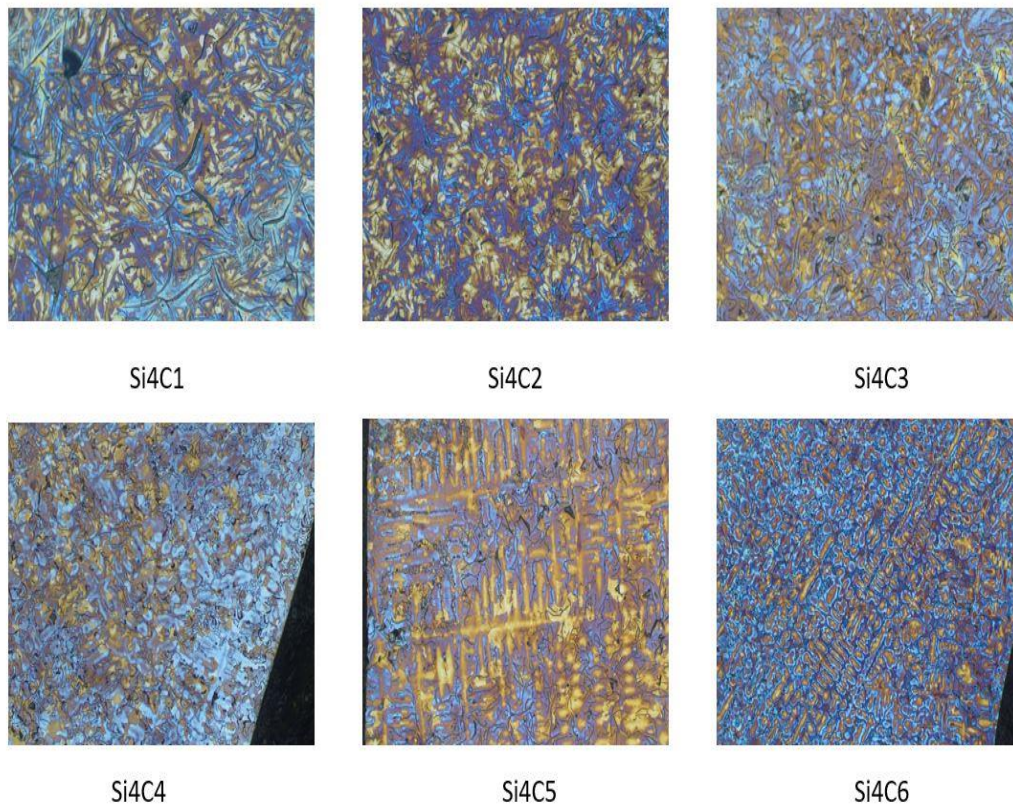


Figure 63: Color etched microstructure images of 30mm diameter (high cooling condition)

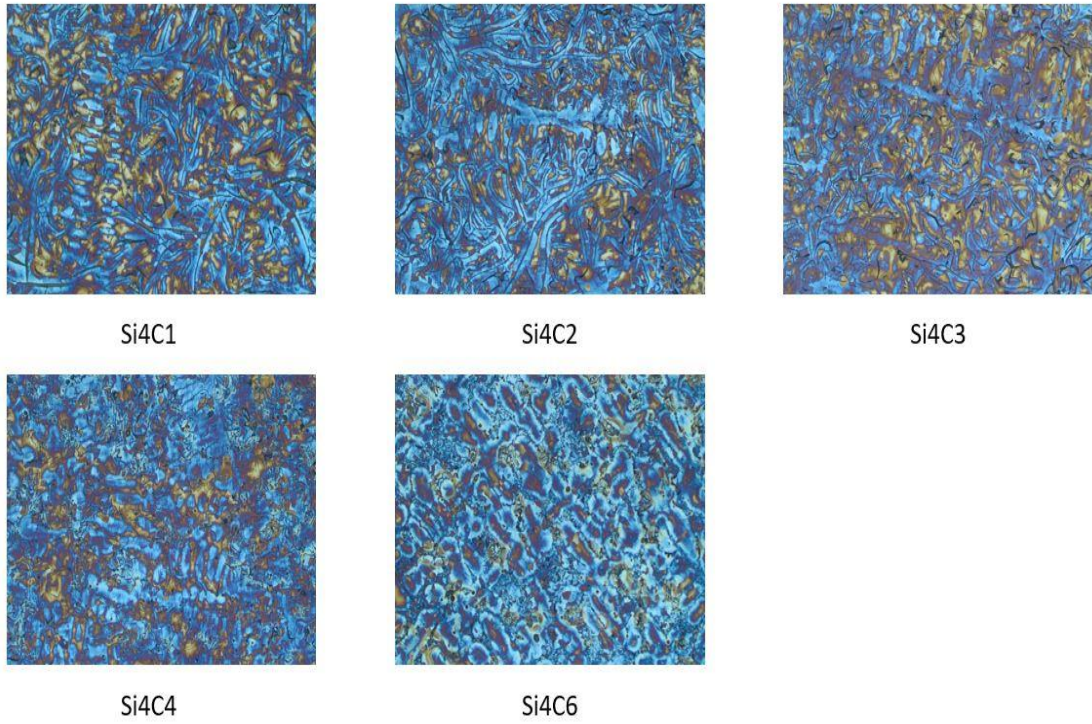


Figure 64: Color etched microstructure images of 55mm diameter (Moderate cooling condition)

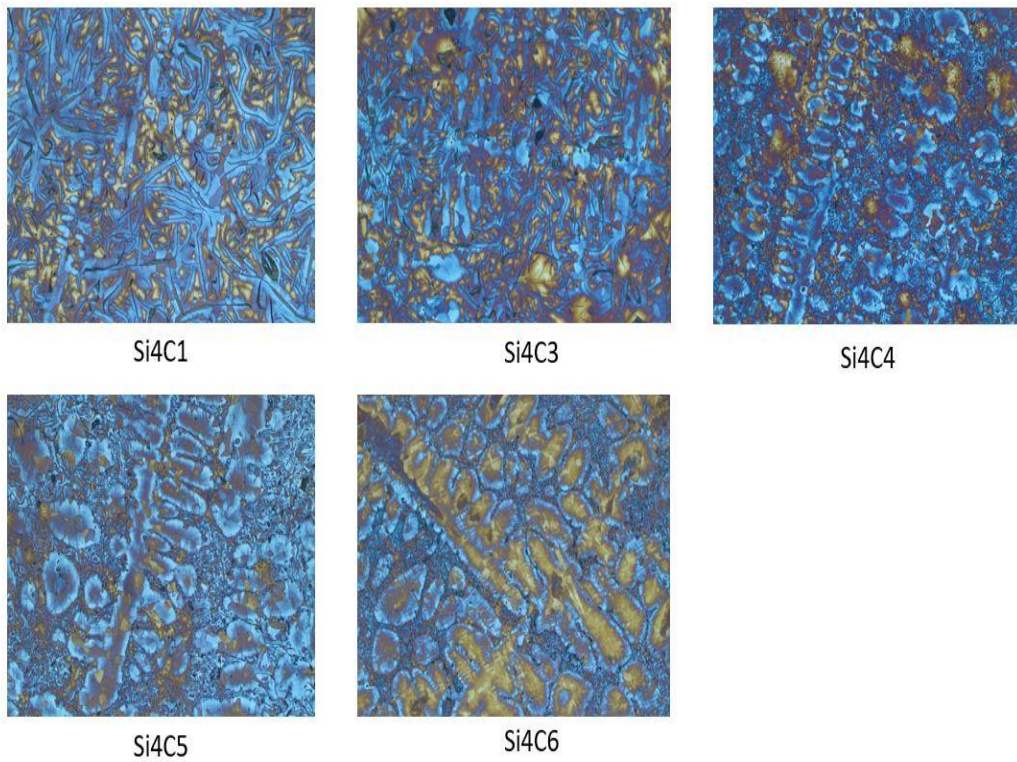


Figure 65: Color etched microstructure images of 80mm diameter (lowest cooling condition)

5 Discussion and conclusions

5.1 Discussion of the method:

The methodology used for this work can be viewed from the flowchart in figure 12. The different casts were made using 3d printed Silica sand molds. Due to the drier nature of the silica sand compared to green sand molds, some cracks were developed on the sides and surfaces, which eventually lead to surface porosities. Moreover, the method of pouring the melt is of utmost importance while casting the samples as that also determined the shrinkage and porosities which may be produced. However, the cracks on the mold were overcome by tying steel wires around them which helped to keep the mold intact while pouring the melt. Another problem that was encountered during the method for casting the samples was the floatation of the primary graphite phase onto the top of the melt as slurry, as seen from figure (66). This was visible while casting hypereutectic compositions, and the graphite precipitated on the top as lumps, which had to be consecutively removed. But the charge required for making the casts was calculated considering this perspective and the composition remained quite good.

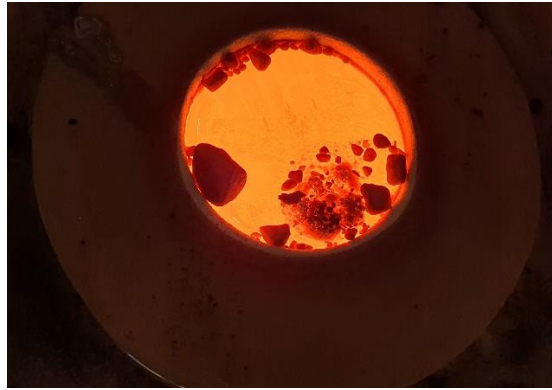


Figure 66: Graphite Lumps are seen in the melt during the casting

The cutting and machining of the samples were not difficult because lamellar graphite iron is not ductile and breaks easily. However, the low carbon casts (Si4C5 and Si4C6) were more difficult to cut and machine as it has more fraction of dendrites and hence more strength.

The same issue was faced while performing tensile tests. The specifications provided for the specimen were intended for miniaturized tensile testing. The ultimate tensile rig was chosen because it could handle a higher number of tests, as the sample count was big. The miniaturized tensile rig (MTS) was thus kept as a standard to compare the results obtained from the ultimate tensile rig. However, the results from the ultimate tensile testing rig deemed satisfactory when compared to those obtained from the miniaturized tests. The table (9) shows the maximum tensile strengths obtained from the UTS and the miniaturized tensile rig.

Various support systems were considered while performing the tests in the UTS rig. Owing to the small size of each specimen, the grips designed for the UTS rig seemed to crush the grips on the sample. Hence aluminum sheets were used in between the wedges to hold the specimen without crushing them, as shown from figure (67a). Moreover, the grooves on the wedges in between the grips were not fine enough to hold the samples. The sheets provided good protection from the grooves as well. The

samples with higher carbon contents were easier to break as they have more graphite flakes of type A and type C distribution. As the carbon content decreased, the samples were harder to break. Hence, for this purpose, a load cell of 20kN was initiated into the tensile rig to help break the samples, as seen from figure (67b). The load cell was also attached to a grip as shown in figure (67b), which held one end of the sample. As seen from the table (6), (7) and (8) from the appendix 1, the standard deviation of the hypoeutectic samples for all three cooling rates was higher as it was harder to attain consistent results for the tensile strength. More samples of the same composition had to be subjected to tensile testing to get more consistent results.

Composition	Cooling Condition	MTS (MPa)	UTS (MPa)
Si4C1	30mm (Higher cooling condition)	111.53	113.18
Si4C5	80mm (Lower cooling condition)	144.90	146.77

Table 9: Comparison of tensile strengths obtained from the MTS and UTS for Si4C1 and Si4C5

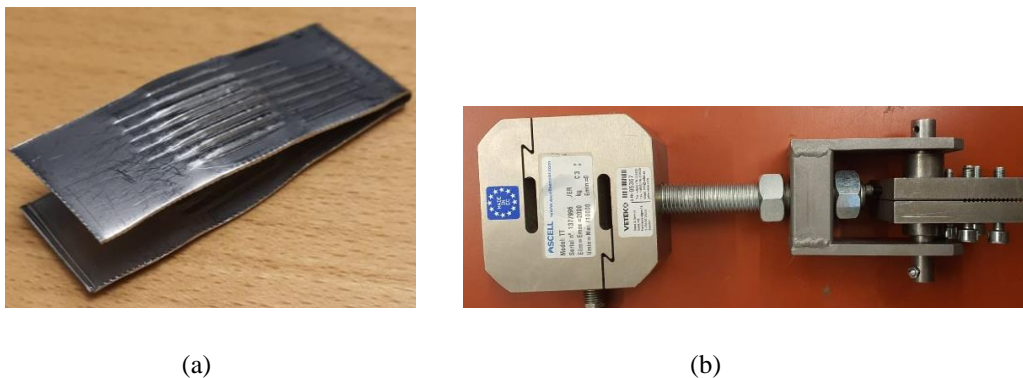


Figure 67: the supports used in the UTS rig. (a) shows the aluminum sheet employed within the grips and (b) shows the 20kN load cell with the supportive grip employed to break the samples of low carbon contents.

The etching of the samples was more than satisfactory. All the samples subjected to etching had good color micrographs. The over etched samples were grinded and polished again, and then subjected to color etching till the right shade of the film was observed.

5.2 Discussion of findings:

- What is the effect of a higher content of silicon on the microstructure of the studied alloy?

On observing the microstructure of the casts from figures (63), (64) and (65), for the hypereutectic samples Si4C1 and Si4C2, with higher carbon content, the dendrites are blue, while for the compositions Si4C3 and Si4C4, there seems to be a yellowish-brown

hue for the dendrites. However, for the low carbon casts (Si4C5 and Si4C6), the micrographs showed the dendrites to have a yellowish-brown center and blue corners that shape these dendrites. According to previous literature [64], elements that enhance the growth of a stable graphite-austenite eutectic tends to segregate into the austenite. For a Fe-C-X alloy grey iron, for high C content compositions, the alloying element X tends to segregate into the austenite, while it crystallizes from the liquid. The reverse happens for low carbon samples, where the element X tends to be expelled from the austenite into the melt. It is also a widely accepted fact that Si is a good graphitizer and a graphite stabilizer, meaning that it promotes the growth of free graphite flakes rather than promote carbides and helps the solidification process to follow the stable system [65]. Hence a higher wt percentage of silicon may promote more fraction of graphite flakes to precipitate freely. Thus the segregation of Si does play an important role in understanding the microstructure of the selected alloy in the present study. By looking into previous studies [58], it could be understood that the etchant used helps study the microsegregation of Si, from the color scheme obtained in the dendrites. The SiO₂ layer formed due to the etching helps study this segregation from the dendrites. A blue-tinged dendrite corresponds to a higher amount of Si in the dendrite and a yellowish-brown hue corresponds to the segregation of Si around the dendrites.

Hence, from the present work considered, the hypereutectic samples had blue dendrites, which maybe owing to the segregation of a higher concentration of Si in them. Furthermore, the yellowish-brown tint observed for the dendrites of Si4C3 and Si4C4 maybe because of the microsegregation of the Si and exclusion of it from the dendrites, into the melt. The hypoeutectic compositions had a more pronounced difference than the usual segregation pattern observed for 1-3% Si. This may be because of the high concentration of the Si in the present work. The usual trend could have been followed by rejecting the Si from the dendrites, into the melt. However, it may be due to this high content of Si that reverse segregation of Si happens back into the dendrites during the solidification. Hence this may allow the segregation of Si around the corners of the dendrites formed, as seen from the figure (63), (64) and (65), giving rise to yellowish-brown dendrites with blue around the ends.

- What is the effect of carbon content and microstructure on the thermal conductivity and the tensile strength of the studied alloy?

On thermal conductivity:

From the figures (57), (58) and (59), it can be seen that the carbon content has a direct influence on the thermal conductivity, for all three cooling conditions. From tables (6), (7) and (8) from the appendix 1, the hypereutectic composition Si4C1, for the high, moderate, and low cooling rates, have thermal conductivities of 73.31 W/(mK), 71.68 W/(mK), and 82.87 W/(mK) respectively, at room temperatures. This may possibly be due to the influence of the graphite flakes of C-type morphology, as shown in the table (12) from Appendix 1, owing to the high carbon content. This trend is similar to that observed in literature [40]. According to previous literature [4], the thermal conductivity of grey cast iron generally depends on the morphology of the graphite inclusions and these flakes are responsible primarily for increasing the thermal conductivity. The general thermal conductivity of grey iron for increasing temperatures from 100°C to 500 °C is between 40 W/(mK) and 52 W/(mK) [4]. However, the results

obtained in the present work are quite higher than the generally observed values of thermal conductivity of grey iron, as seen in literature [4]. This may also be because the heat flux of the graphite is greater than that of the matrix, hence making it a preferential passage for heat [40].

Moreover, it can also be observed that the thermal conductivities for all the compositions for all three cooling conditions become more consistent as the temperature rises. The same trend can be observed in previous study [40] and it was concluded that this could be because of more influence from the metal matrix on the thermal conductivity, with increasing temperature. It can be seen from the microstructure of Si4C1 for 80mm cast (lowest cooling condition) that the matrix is fully ferritic, as seen from figure(65). It has been stated in literature [42] that the ferritic matrix has the second-best conductivity after graphite in the microstructure. This may explain why the thermal conductivity of Si4C1 at a lowest cooling condition is seen to be maximum. Moreover, the thermal conductivity decreases dramatically on the influence of pearlite [42]. Some colonies of pearlite had been observed in the high carbon composition of the 30mm and the 55mm diameter cylinders, which may explain its lower values of thermal conductivity when compared to the 80mm casts. The influence of the metal matrix also increases with decreasing carbon contents [40]. This may explain the behavior of the hypoeutectic compositions for all the cooling conditions, of having increased thermal conductivity till about 300°C to 400 °C and then a decrease. The results show that the increased thermal conductivity at room temperature and the consistent but steady decrease at elevated temperatures may depend on the differences in heat conduction between the graphite flakes and its morphology and the metal matrix. However, it is quite difficult to determine the differences in thermal conductivity with the graphite orientation as graphite here is oriented anisotropically, as can be observed from figures (63), (64) and (65).

On Tensile Strength :

The tensile strength of grey cast iron is highly dependant on the carbon content and the graphite morphology. In the present work, Si4C6 for all three cooling conditions has the maximum tensile strength and it is also generally seen from table (5), that the tensile strength has an inverse correlation with the carbon content. Moreover as the carbon content decreases, the graphite morphology changes from type C in hypereutectic samples to type E and type D, in the hypoeutectic samples as shown in table (12) from appendix 1. As stated in the previous literature [66], type C graphite are very coarse and long needle like flakes, while type D and type E exhibits short and randomly oriented flakes. Previous literature [8] states that the length of the graphite flake is inversely proportional to the tensile strength, so type D and E flakes have good tensile strength compared to type C graphite flakes. This may be the possible reason for the decrease in tensile strength as it changes from hypereutectic to hypoeutectic samples.

The fraction of primary dendrites have a linear relationship with the carbon content which is shown in table (6). As suggested in the literature [8] the effect of graphite flakes is controlled by the hydraulic diameter which expresses the space between the dendrites. It has also been concluded that as the dendritic network gets denser the material strength increases. From the table (7), for low carbon content the fraction of primary dendrites increases, which in turn leads to the decrease of hydraulic diameter. Furthermore, it can be seen from figure (63), (64), (65) that the inter dendritic space

becomes smaller as the carbon content decreases. This is in accordance with the previous literature [8]. Hence this may be a possibility behind the reduction of tensile strength as carbon content increases.

- How does the high content of silicon affect the thermal conductivity and the tensile strength of the studied alloy ?

On thermal conductivity:

As observed from table (6), (7) and (8) in appendix 1, the hypereutectic composition have higher thermal conductivity than the hypoeutectic compositions. It is a widely accepted fact that Si is a good graphitizer, meaning that it promotes the growth of free graphite flakes rather than promote carbides [65]. As the present work uses a higher fraction of Si, which is generally not observed in any previous literatures, it may allow a higher fraction of graphite flakes to precipitate freely, owing to the increased thermal conductivity. The maximum thermal conductivity in the present work is higher than that observed from previous literature [4] and is increased by almost 30 W/mK. It can also be seen from figure (63), (64) and (65) that the metal matrix is mostly ferritic. As mentioned earlier, the ferritic matrix has the second-best conductivity after graphite in the microstructure, which has been stated in literature [42]. Previous literature [67] shows that increasing the concentration of silicon in the composition increases the fractions of ferrite in the metal matrix as opposed to pearlite. The solidification of the free graphite reduces the concentration of carbon in the liquid, increasing the concentration of ferrite in those regions. Hence, the promotion of free graphite growth, along with the growth of a ferritic matrix may be the reason behind the higher thermal conductivity of the hypereutectic samples for the 80mm diameter cast.

It can be observed from the figures (57), (58) and (59) the conductivity becomes more consistent at higher temperatures. This aligns with past research [40] and this may be the influence of the ferritic matrix, which is enhanced due to the excess concentration of Si. But as for the low carbon samples at high cooling condition, the presence of pearlite colonies was encountered which may be the reason for the small drop in the thermal conductivity after about 400 °C, in accordance with previous literature [42]. The presence of these colonies may also be due to the segregation of Si from the austenite into the melt, for the low carbon samples. It has been reported in [68] that pearlite occurs at the ferrite-austenite interface and it proceeds to grow from inside the remaining austenite, during its eutectoid transformation. The ferrite can still grow even after the pearlitic reaction has started, but the growth rate of the pearlite is much higher than the ferrite. So for the low carbon samples where the Si is expelled from the austenite, there may be more chances that pearlite colonies start to nucleate and grow in competition with the ferritic growth actuated by the excess Si.

On tensile strength:

In the present work, 4% of Si is used and the maximum tensile strength obtained is close to 250Mpa as can be seen in table (6) and it is predominantly seen in hypoeutectic composition of high cooling condition with very low carbon content (Si4C6). As stated in the previous literature [5], the maximum tensile strength obtained at 1-3% Silicon is between 350 to 400 Mpa. It is known that Si is the enhanced promoter of ferrite [42]

and a good graphitizing agent [65]. Hence it can be suggested that higher concentration of silicon can allow more free graphite to precipitate in the inter dendritic region. This may be a possibility for the free graphite to act as stress concentrators, reducing the tensile strength. Moreover, higher content of silicon increases the volume of free graphite flakes meaning the grain size increases, reducing both hardness and tensile strength [65]. So this may also be the reason why the hypoeutectic samples were hard to break and have more tensile strength. Previous literature [69] states that ferritic surrounding the graphite flakes is softer than pearlite. Hence higher percentage of silicon may develop more ferritic grains which could reduce the tensile strength.

- What is the effect of cooling condition on the Thermal conductivity and Tensile strength of the studied alloy?

On thermal conductivity:

The cooling condition plays an important role in the properties of the grey iron cast. This influences the graphite morphology and the growth of the metal matrix- whether pearlitic or ferritic [70]. Previous literature [71] and [70] proves that at higher cooling conditions, the austenite tends to disintegrate to pearlite at the eutectoid and at slower cooling, into ferrite. Increasing the cooling conditions seem to reduce the growth of ferrite below the eutectoid. The micrographs obtained from the samples of this study also show the same trend, as seen from figures (63), (64) and (65). For the higher cooling conditions, there were small fractions of pearlite colonies in the matrix. But for the slow cooling, the matrix was fully ferritic and this may influence the thermal conductivity positively. Moreover, at a reduced cooling, the solidification time is more which could possibly allow better segregation of Si and may also allow more carbon to enter the melt and precipitate as free graphite. Thus, the thermal conductivity seems to be maximum for the slowest cooling rate which could be due to the above-mentioned factors. This is also according to previous literature [71] and [70].

On tensile strength:

It can be observed from table (6), that the tensile strength is highest for the cast with diameter 30mm (high cooling condition). Previous literature [71] suggest that, the reduction of casting thickness increases the cooling rate. So this may be the reason why the cast with diameter 30mm has the higher cooling condition compared to the cast with diameter 55mm and 80mm. Moreover, literature [71] indicates that, the increase cooling rate lead to the reduction of eutectic cell diameter. However previous studies [8] have also suggested that the maximum graphite flake length has direct relationship with the eutectic cell diameter. This may also be the reason why the casts with highest cooling condition has greater tensile strength as they may have shorter graphite flake length. On the other hand, cast with 80mm diameter has the lowest tensile strength. This may be due to the presence of more ferrite grains which is in accordance with previous literature [10] where it suggest that decrease in cooling condition could increase the amount of free ferrite.

5.3 Conclusions and Future work

The results obtained from the present work of study can be concluded as follows:

- The thermal conductivity seems to be more than the studies conducted previously. The maximum thermal conductivity obtained in the present work is between 70 W/mK and 80 W/mK and has a difference of approximately 30 W/mK from that of previous literature observed.
- The tensile strength seems to be reduced by 150 Mpa when compared to the previous literature studies. The maximum tensile strength obtained in the present work of study is close to 250 MPa.
- Other studies states that Si promotes the growth of free graphite flakes and also promotes the growth of a ferritic matrix. Both graphite and ferrite are known to be good conductors of heat but also have an inverse relationship with the tensile strength. This may be the possible reason why the present work shows an increased thermal conductivity and reduced tensile strength. Moreover, previous works have studied hypoeutectic samples whereas the current work deals with both hypoeutectic and hypereutectic compositions, which may also confirm the results in the present work.
- At the higher cooling conditions small colonies of pearlite was observed from the microstructure. While the matrix was fully ferritic at lower cooling conditions.
- Graphite morphology tends to change from type C to type E as carbon content decreases and moreover, the hypoeutectic samples had type D graphite flakes predominantly for all the three cooling conditions.
- For hypereutectic samples, the dendrites appear to be blue and for Si₄C₃ and Si₄C₄, they appear yellowish brown. However, for the hypoeutectic samples the dendrites appears to have a yellowish brown center with blue hue at the ends.
- Tensile strength was found to be higher for samples having low hydraulic diameter and high fraction of dendrites.

Due to the limitations encountered within the scope of this thesis, there is room for future work. These are summarized below:

- The work has been conducted for just 4% Si. Better understanding of the thermal and the mechanical behavior can be made if the range of Si is also extended from 1% to 3%.
- The ferrite and pearlite fractions have a direct impact on the thermal and tensile properties. However, this study has only observed the visible fraction of ferrite or pearlite matrix from the microstructure and has not studied its fraction in detail. This gives scope to get a better understanding of the effects of cooling rates and percentage of Si on the thermal and tensile properties.

6 References

- [1] J. C. Hernando, "Morphological Characterization of Primary Austenite in Cast Iron," Department of Materials and manufacturing, Jonkoping university, 2017.
- [2] P. A. Muela, "Effect of graphite morphology on the thermo-physical properties in cast iron," Material and Manufacturing Engineering, Jonkoping University, Jonkoping, 2019.
- [3] j. C. H. Sanz, The role of primary austenite morphology in cast iron, jonkoping: school of engineering, jonkoping university, 2019.
- [4] I. M. E. M. e. a. W. Guesser, "Thermal conductivity of gray iron and compacted graphite iron used for cylinder head," *Revista Matêria*, vol. 10, no. 2, pp. 265-272, 2005.
- [5] J. S. A. L. R. S. P. Larrañaga, "Gray Cast Iron with High Austenite-to-Eutectic Ratio Part III – High Strength, Low Hardness , High Carbon Equivalent Gray Iron with Superfine Graphite," *Transactions of American Foundry Society*, vol. 120, no. 12-035, pp. 347-354, 2012.
- [6] R. Singh, "Cast Iron," in *Applied Welding Engineering-Processes, codes and Standards*, Elsevier, 2012, pp. 65-66.
- [7] J. Davis, ASM Specialty Handbook Cast Irons, ASM International, 1996.
- [8] V. Fourlakidis, "Dendritic Morphology and Ultimate Tensile Strength of Pearlitic Lamellar Graphite Iron," Materials and Manufacturing engineering, Jonkoping University, 2019.
- [9] R. H. W. Bolton, "Cast Iron," in *Materials for Engineers and Technicians*, New York, Routledge, 2014, pp. 205-217.
- [10] D. Sundaram, "The Effect of Cooling Rate and Solidification Time on the Ultimate Tensile Strength of Grey cast iron," School of Industrial Engineering and Management, KTH Royal Institute of Technology, Stockholm, 2018.
- [11] F.C.Campbell, "Metallic Structure," in *Elements of Metallurgy and Engineering Alloys*, Ohio, ASM International, 2008, pp. 14-17.
- [12] M. E. S. E. M. M. Hiroaki Okamoto, ASM Handbook Volume 3: Alloy Phase Diagrams, ASM International, 2016.
- [13] A. O. Bruce L.Bramfitt, Introduction to Steels and Cast Irons, United States of America: ASM International, 2002, pp. 1-21.
- [14] D. P. Colao, "Solidification of Graphite Cast Iron: Influence of the microstructure on the," Department of Materials and Manufacturing, Jonkoping, 2019.
- [15] A. G. Saro, "THERMAL CONDUCTIVITY IN HIGH SILICON," Materials and Manufacturing,Casting,, Jonkoping University, 2013.
- [16] C. F. Walton, The Grey Iron Castings Hand Book, Cleveland: Grey Iron Founders Society INC., 1958.
- [17] A. A. W. a. F. Y. T. Alp, "MICROSTRUCTURE–PROPERTY RELATIONSHIPS IN CAST IRONS," *The Arabian Journal for Science and Engineering*, vol. 30, 2005.
- [18] R. B. J. S. G.L. Rivera, "Solidification of gray cast iron," *Scripta Materialia*, p. 331–335, 2003.
- [19] A. Vadiraj, "Mechanical and wear behavior of quenched and tempered alloyed hypereutectic gray cast iron," Elsevier, 2010.
- [20] P. Svidró, Study of solidification and volume change in lamellar cast iron with respect to defect formation mechanisms, Stockholm: Department of Materials Science and Engineering, Royal Institute of Technology, 2013.
- [21] D. M. Stefanescu, "Classification and Basic Metallurgy of Cast Iron," *Properties and Selection: Irons, Steels, and High-Performance Alloys*, no. February 1990, pp. 3-11, 2018.

- [22] L. A. D. a. P. S. Elmquist, "Influence of primary austenite on the nucleation of eutectic cells," *Key Engineering Materials*, vol. 457, pp. 61-66, 2011.
- [23] N. Arab, "Competitive Nucleation in Grey Cast Irons," *Archives of Foundry Engineering*, vol. 17, no. 4, pp. 185-189, 2017.
- [24] S. Carlsson, Grain refinement of aluminium by titanium diboride particles, STOCKHOLM: SKOLAN FÖR INDUSTRIELL TEKNIK OCH MANAGEMENT, 2019.
- [25] M. C. Flemings, "THE SOLIDIFICATION OF CASTINGS," *Scientific American*, Vols. Vol. 231,, pp. 88-95, 1974.
- [26] K. Z. L. & I. L. S. A. Diószegi, "Inoculation of primary austenite in grey cast iron," *International Journal of Cast Metals Research*, vol. 20, no. 2, pp. 68-72, 2007.
- [27] B. Domeij, "On the Solidification of Compacted and Spheroidal Graphite Irons," School of Engineering, Jönköping University, Jönköping, 2017.
- [28] a. M. J.A.Dantzig, Solidification, CRC publisher, 2016.
- [29] B. Domeij, "Compacted graphite iron: On solidification phenomena related to shrinkage defects," School of Engineering, Jönköping University, Jönköping , 2019.
- [30] B. H. MORROGH and W. OLDFIELD, SOLIDIFICATION OF GREY CAST IRON, 1959.
- [31] E. Moumeni, Solidification of cast iron - A study on the effect of microalloy elements on cast iron, Denmark: Technical University of Denmark., 2013.
- [32] M. Tisza, Physical Metallurgy for Engineers, London: freund publishing house, 2002.
- [33] D. M. a. R. R. Stefanescu, "The Liquid State and Principles of Solidification of Cast Iron," *Cast Iron Science and Technology*, vol. 1, pp. 46-58, 2018.
- [34] V. H.patterson, "Some Basic Considerations in controlling the mechanical properties of cast iron," in *Foote Foundry facts*, Foote Mineral Company.
- [35] D. Holmgren, "Review of thermal conductivity of cast iron," *International Journal of Cast Metals Research*, vol. 18, no. 6, pp. 331-345, 2005.
- [36] D. I. L. Holmgren, "Thermal conductivity-structure relationships in grey cast iron," *International Journal of Cast Metals Research*, vol. 18, no. 6, pp. 321-330, 2005.
- [37] R. L. R. B. W. D. H. Hecht, "Thermal transport properties of grey cast irons," *SAE Technical Papers*, vol. 105, pp. 1699-1705, 1996.
- [38] A.Salazar, "On thermal diffusivity," *European Journal of Physics*, vol. 24, no. 4, pp. 351-358, 2003.
- [39] J. Bird and C. Ross, "Thermal expansion," *Mechanical Engineering Principles*, pp. 296-304, 2019.
- [40] A. D. I. S. D. Holmgren, "Effects of inoculation and solidification rate on the thermal conductivity of grey cast iron," *Institute of Cast Metals Engineers - 67th World Foundry Congress, wfc06: Casting the Future*, vol. 2, no. 2, pp. 993-1002, 2006.
- [41] R. K. I. S. D. Holmgren, "Influences of the graphite growth direction on the thermal conductivity of cast iron," *Metallurgical and Materials Transactions A: Physical Metallurgy and Materials Science*, vol. 38, no. 2, pp. 268-275, 2007.
- [42] Y. L. J. Y. Z. M. Z. Y. D. Y. T. L. M. Wu, "Computational Assessment of Thermal Conductivity of Compacted Graphite Cast Iron," *Advances in Materials Science and Engineering*, vol. 2019, 2019.
- [43] R. GHASEMI, The Influence of Microstructure on Mechanical and Tribological Properties of Lamellar and Compacted Irons in Engine Applications, JÖNKÖPING: JÖNKÖPING UNIVERSITY, SCHOOL OF ENGINEERING, 2016.
- [44] V. Furlakidis, "A Generic Model to Predict the Ultimate Tensile Strength in Pearlitic Lamellar Graphite Iron," *Materials Science and Engineering A*, 2014.
- [45] R. A. Higgins, Engineering Metallurgy, British Library Cataloguing, 1993.
- [46] D. Stefanescu, "Mechanical Properties of Gray Irons," *ASM Handbook, Cast Iron Science and Technology*, vol. 1, pp. 1-26, 2017.
- [47] M. B. A. H. H.R. Abbasi, "Effect of phosphorus as an alloying element on microstructure and mechanical properties of pearlitic gray cast iron," *Materials Science and Engineering*, pp. 314-317, 2007.

- [48] T. K. a. I. Kang, "Quantitative Relation between Mn and S for Mechanical Properties of Flake Graphite Cast Iron," *Japan Foundry Engineering Society*, vol. 55, no. 11, p. 1716 to 1721, 2014.
- [49] B. Sickler, "MATERIAL RESEARCH LABORATORY AT UCSB: AN NSF MRSEC," [Online]. Available: https://www.mrl.ucsb.edu/sites/default/files/mrl_docs/instruments/New%20DSC%20Guide%20v3B.pdf.
- [50] Netzsch, "Netzsch Thermal Analysis," Netzsch Groups, [Online]. Available: https://www.netzsch-thermal-analysis.com/media/thermal-analysis/brochures/DIL_Select_Supreme_en_web.pdf.
- [51] A. Technologies, "Linear thermal Expansion coefficients of metals and alloys," in *Material Expansion Coefficients*, 2002, pp. 17-1 to 17-12.
- [52] J. Bird and C. Ross, "Thermal expansion," *Mechanical Engineering Principles*, pp. 296-304, 2019.
- [53] F. Wohlfahrt and R. Theska, "Force-Controlled Measuring Cell in Dilatometry," vol. 93, no. 4, 2016.
- [54] F. Neidhardt, "When and how must Samples be coated during LFA Measurements," Netzsch, 2014.
- [55] Netzsch, "Laser Flash Apparatus LFA 427," Netzsch, 2018.
- [56] P. H. Jan Zajac, "Measurements of thermal diffusivity, specific heat capacity and thermal conductivity with LFA 447 apparatus," Aalborg University, Denmark, 2013.
- [57] Zwick-Roell, "Zwick Z100/ Z250 Materials Testing machine with central ball-lead screw," p. 2, 2005.
- [58] J. E. ., A. D. S. Vazehrad, "Study of microstructure and silicon segregation in cast iron using color etching and electron microprobe analysis," *Materials Characterization*, vol. 104, pp. 132-138, 2015.
- [59] I. K. Peter J. Szabo, "Correlation between grain orientation and the shade of color etching," *Materials Characterization*, vol. 61, no. 8, pp. 814-817, 2010.
- [60] Prep_Struers, "Consumables Catalogue," *Ref_Prep_Sample*, 2020.
- [61] R. Soeurs, "Citopress 1," 2008.
- [62] J. M. Radzikowska, "Effect of specimen preparation on evaluation of cast iron microstructures," *Materials Characterization*, vol. 54, no. 4-5, pp. 287-304, 2005.
- [63] Struers, Tegamin-25/30 Instruction Manual, Ballerup: Struers A/S, 2013.
- [64] U. K. D. B. D. A. Old Windsor, "Inferring the development of microsegregation and microstructure in Spheroidal and Compacted Graphite Iron using EPMA#WDS," *Solidification Processing 2017: Proceedings of the 6th Decennial International Conference on Solidification Processing*, no. July, pp. 455-458, 2017.
- [65] P. S. K. K. Singhal, "Effect of silicon addition on microstructure and mechanical properties of grey cast Iron: An overview," *Materials Today: Proceedings*, vol. 26, pp. 1393-1401, 2019.
- [66] J. Radzikowska, "Metallography and microstructures of cast iron," *cast iron and technology*, pp. 379-398, 2018.
- [67] B. C. R. F. M. A. B. M. L. W. C. E. C. Ribeiro, "Influence of different concentrations of silicon, copper and tin in the microstructure and in the mechanical properties of compacted graphite iron," *Materials Research*, vol. 23, no. 2, pp. 1-10, 2020.
- [68] J. Lacaze, J. Sertucha and L. Magnusson Åberg, "Microstructure of as-cast ferritic-pearlitic nodular cast irons," *ISIJ International*, vol. 56, no. 9, pp. 1606-1615, 2016.
- [69] V. F. a. i. L. s. attila dioszegi, "Microstructure and tensile properties of grey cast iron," Jonkoping university, 2004.
- [70] M. Górny and E. Tyrała, "Effect of cooling rate on microstructure and mechanical properties of thin-walled ductile iron castings," *Journal of Materials Engineering and Performance*, vol. 22, no. 1, pp. 300-305, 2013.

- [71] F. F. Lima, L. F. Bauri, H. B. Pereira and C. R. Azevedo, "Effect of the cooling rate on the tensile strength of pearlitic lamellar graphite cast iron," *International Journal of Cast Metals Research*, vol. 33, no. 4-5, pp. 201-217, 2020.
- [72] I. Hassan, "Effects of Austempering Process on Mechanical Behavior Properties of Compacted Graphite Iron," Materials and Manufacturing Department, Jonkoping Univetrnsity, Jonkoping , 2019.

7 Appendices

Appendix 1: List of tables

Cooling Rate	Label	Specific Heat, Cp (J/(gK))										
		25	50	100	150	200	250	300	350	400	450	500
30mm	Si4C1	0.555	0.572	0.606	0.64	0.674	0.709	0.743	0.777	0.811	0.845	0.879
	Si4C2	0.559	0.576	0.609	0.643	0.676	0.71	0.744	0.777	0.811	0.844	0.878
	Si4C3	0.551	0.565	0.591	0.618	0.644	0.671	0.697	0.724	0.75	0.777	0.803
	Si4C4	0.483	0.497	0.524	0.552	0.579	0.607	0.635	0.662	0.69	0.718	0.745
	Si4C5	0.525	0.54	0.568	0.597	0.625	0.654	0.682	0.711	0.739	0.768	0.796
	Si4C6	0.512	0.524	0.549	0.573	0.597	0.621	0.646	0.67	0.694	0.718	0.742
55mm	Si4C1	0.55758	0.57645	0.61385	0.65089	0.68829	0.72569	0.76309	0.80013	0.83753	0.87492	0.91196
	Si4C2	0.55561	0.57275	0.6067	0.64033	0.67429	0.70824	0.7422	0.77583	0.80978	0.84374	0.87737
	Si4C3	0.57628	0.59253	0.62473	0.65662	0.68881	0.72101	0.7532	0.78509	0.81728	0.84948	0.88137
	Si4C4	0.56511	0.58187	0.61506	0.64794	0.68113	0.71432	0.74751	0.78039	0.81358	0.84678	0.87965
	Si4C5	0.54567	0.56048	0.58981	0.61887	0.64821	0.67755	0.70689	0.73595	0.76529	0.79463	0.82369
	Si4C6	0.4325	0.44784	0.47824	0.50834	0.53874	0.56914	0.59953	0.62964	0.66004	0.69043	0.72054
80mm	Si4C1	0.6717	0.69367	0.74317	0.80003	0.86534	0.9386	1.0198	1.1081	1.2051	1.31	1.4218
	Si4C2	0.62291	0.63556	0.66268	0.69226	0.72484	0.76017	0.79825	0.83867	0.8822	0.92848	0.97703
	Si4C3	0.60617	0.61869	0.64555	0.67482	0.70708	0.74205	0.77974	0.81974	0.86283	0.90863	0.95667
	Si4C4	0.60578	0.61769	0.6432	0.67097	0.70153	0.73463	0.77028	0.80808	0.84878	0.89202	0.93734
	Si4C5	0.63483	0.6479	0.67629	0.70798	0.74263	0.78091	0.82249	0.86694	0.91511	0.96658	1.0208
	Si4C6	0.59749	0.60947	0.63512	0.66303	0.69374	0.72699	0.76277	0.80072	0.84156	0.88494	0.93041

Table 1: Specific Heat values of the different compositions for all three cooling rates

Cooling Rate	Label	Thermal Expansion Coefficient, Alpha (/K)										
		25	50	100	150	200	250	300	350	400	450	500
30mm	Si4C1	1.13E-05	1.15E-05	1.18E-05	1.21E-05	1.24E-05	1.28E-05	1.31E-05	1.34E-05	1.37E-05	1.41E-05	1.44E-05
	Si4C2	1.17E-05	1.19E-05	1.22E-05	1.25E-05	1.28E-05	1.31E-05	1.34E-05	1.37E-05	1.40E-05	1.13E-05	1.46E-05
	Si4C3	1.18E-05	1.19E-05	1.22E-05	1.25E-05	1.27E-05	1.30E-05	1.33E-05	1.36E-05	1.38E-05	1.41E-05	1.44E-05
	Si4C4	1.19E-05	1.20E-05	1.23E-05	1.26E-05	1.29E-05	1.32E-05	1.36E-05	1.39E-05	1.42E-05	1.45E-05	1.48E-05
	Si4C5	1.16E-05	1.18E-05	1.21E-05	1.24E-05	1.28E-05	1.31E-05	1.35E-05	1.38E-05	1.41E-05	1.45E-05	1.48E-05
	Si4C6	1.18E-05	1.20E-05	1.23E-05	1.26E-05	1.29E-05	1.32E-05	1.36E-05	1.39E-05	1.42E-05	1.45E-05	1.48E-05
55mm	Si4C1	1.22E-05	1.23E-05	1.25E-05	1.28E-05	1.30E-05	1.33E-05	1.35E-05	1.38E-05	1.40E-05	1.43E-05	1.45E-05
	Si4C2	1.16E-05	1.18E-05	1.21E-05	1.25E-05	1.28E-05	1.31E-05	1.35E-05	1.38E-05	1.41E-05	1.45E-05	1.48E-05
	Si4C3	1.18E-05	1.20E-05	1.23E-05	1.26E-05	1.29E-05	1.32E-05	1.35E-05	1.38E-05	1.42E-05	1.45E-05	1.48E-05
	Si4C4	1.18E-05	1.19E-05	1.22E-05	1.25E-05	1.29E-05	1.32E-05	1.35E-05	1.38E-05	1.41E-05	1.44E-05	1.48E-05
	Si4C5	1.16E-05	1.17E-05	1.21E-05	1.24E-05	1.27E-05	1.31E-05	1.34E-05	1.37E-05	1.41E-05	1.44E-05	1.47E-05
	Si4C6	1.21E-05	1.23E-05	1.26E-05	1.29E-05	1.33E-05	1.36E-05	1.39E-05	1.42E-05	1.45E-05	1.48E-05	1.52E-05
80mm	Si4C1	1.19E-05	1.20E-05	1.24E-05	1.27E-05	1.30E-05	1.33E-05	1.37E-05	1.40E-05	1.43E-05	1.46E-05	1.50E-05
	Si4C2	1.23E-05	1.24E-05	1.26E-05	1.28E-05	1.30E-05	1.33E-05	1.35E-05	1.37E-05	1.39E-05	1.42E-05	1.44E-05
	Si4C3	1.19E-05	1.21E-05	1.24E-05	1.27E-05	1.30E-05	1.33E-05	1.36E-05	1.39E-05	1.42E-05	1.45E-05	1.48E-05
	Si4C4	1.18E-05	1.20E-05	1.23E-05	1.26E-05	1.29E-05	1.33E-05	1.36E-05	1.39E-05	1.42E-05	1.45E-05	1.48E-05
	Si4C5	1.24E-05	1.26E-05	1.29E-05	1.31E-05	1.34E-05	1.37E-05	1.40E-05	1.43E-05	1.46E-05	1.48E-05	1.51E-05
	Si4C6	1.21E-05	1.22E-05	1.25E-05	1.28E-05	1.32E-05	1.35E-05	1.38E-05	1.41E-05	1.44E-05	1.47E-05	1.50E-05

Table 2 : Alpha values of the different compositions for all three cooling rates

Temperature(oC)	Si4C1		Si4C2		Si4C3		Si4C4		Si4C5		Si4C6	
	thermal diffusivity	Std Dev	thermal diffusivity	Std Dev	thermal diffusivity	Std Dev	thermal diffusivity	Std Dev	thermal diffusivity	Std Dev	thermal diffusivity	Std Dev
25	19.071	0.303	17.159	0.235	14.683	0.355	11.748	0.485	10.677	0.205	9.187	0.275
50	18.022	0.47	16.159	0.242	14.434	0.207	11.983	0.226	10.504	0.092	9.131	0.234
100	16.62	0.689	14.678	0.256	13.077	0.192	11.328	0.122	9.963	0.035	8.999	0.073
200	13.69	0.118	12.542	0.049	11.356	0.164	10.113	0.087	9.086	0.022	8.479	0.051
300	11.78	0.268	10.775	0.215	9.918	0.226	9.149	0.048	8.276	0.069	7.914	0.035
400	9.967	0.186	9.296	0.064	8.837	0.161	8.171	0.155	7.095	0.044	7.186	0.082
500	8.518	0.281	8.151	0.095	7.565	0.109	7.102	0.250	6.616	0.235	6.390	0.162

Table 3: Tabulated values of thermal diffusivity, for 30mm diameter cast, with the standard deviations

Temperature(oC)	Si4C1		Si4C2		Si4C3		Si4C4		Si4C5		Si4C6	
	thermal diffusivity	Std Dev	thermal diffusivity	Std Dev	thermal diffusivity	Std Dev	thermal diffusivity	Std Dev	thermal diffusivity	Std Dev	thermal diffusivity	Std Dev
25	18.515	0.451	21.4899	0.658	16.333	0.251	11.842	0.260	10.541	0.175	8.414	0.453
50	17.663	0.062	20.665	0.132	15.691	0.074	11.983	0.124	10.337	0.168	7.916	0.743
100	15.814	0.047	18.670	0.245	14.452	0.060	11.152	0.076	10.072	0.036	8.310	0.287
200	12.866	0.077	15.775	0.064	12.437	0.099	10.162	0.083	9.310	0.039	8.168	0.038
300	11.001	0.090	13.511	0.130	10.895	0.044	9.144	0.120	8.522	0.183	7.815	0.162
400	9.543	0.255	11.612	0.144	9.428	0.082	8.274	0.344	7.783	0.144	7.099	0.155
500	7.993	0.190	10.016	0.273	8.194	0.131	7.098	0.111	7.002	0.263	6.416	0.137

Table 4: Tabulated values of thermal diffusivity, for 55mm diameter cast, with the standard deviations

Temperature(oC)	Si4C1		Si4C2		Si4C3		Si4C4		Si4C5		Si4C6	
	thermal diffusivity	Std Dev	thermal diffusivity	Std Dev	thermal diffusivity	Std Dev	thermal diffusivity	Std Dev	thermal diffusivity	Std Dev	thermal diffusivity	Std Dev
25	17.718	1.910	16.930	0.394	14.531	0.566	11.499	0.549	10.985	1.476	8.216	0.312
50	17.385	0.067	16.266	0.198	14.158	0.188	11.315	0.120	12.315	0.298	8.289	0.174
100	15.890	0.078	14.661	0.177	13.054	0.096	10.743	0.107	11.944	0.103	8.274	0.101
200	13.171	0.046	12.250	0.051	11.188	0.074	9.794	0.123	11.079	0.061	7.999	0.056
300	11.171	0.076	10.591	0.088	9.716	0.138	9.030	0.052	10.216	0.089	7.588	0.050
400	9.523	0.066	9.131	0.117	8.590	0.126	7.946	0.263	9.327	0.216	7.037	0.091
500	8.083	0.214	7.947	0.338	7.232	0.287	7.257	0.498	8.176	0.230	6.261	0.127

Table 5: Tabulated values of thermal diffusivity, for 80mm diameter cast, with the standard deviations

LABEL	TEMPERATURE											THERMAL CONDUCTIVITY
	25	50	100	150	200	250	300	350	400	450	500	
Si4C1	73.31297	72.30219	70.14364	67.84417	65.37493	62.9655	60.51294	58.25464	56.16769	54.39928	53.05928	
Si4C2	66.10073	65.24365	63.33561	61.45773	59.38267	57.43306	55.58872	53.89428	52.50054	51.32064	50.79486	
Si4C3	57.73862	56.77927	54.87277	53.31432	51.81774	50.55204	49.29274	48.13289	46.77679	45.268	43.38135	
Si4C4	41.15309	41.57586	42.10552	42.4188	42.3451	42.07786	41.57641	40.84593	40.01759	39.10989	38.16163	
Si4C5	39.92176	40.20795	40.51732	40.73452	40.68737	40.52463	40.12043	39.61451	38.85086	37.95939	36.85848	
Si4C6	33.73061	34.22834	35.16233	35.85266	36.33207	36.59129	36.67168	36.45582	35.95628	35.17026	34.10393	

Table 6 : Tabulated values for the thermal conductivity, for 30mm diameter

LABEL	TEMPERATURE											THERMAL CONDUCTIVITY
	25	50	100	150	200	250	300	350	400	450	500	
Si4C1	71.67775	69.95394	66.82818	64.13577	61.84046	59.92539	58.28446	56.80031	55.24022	53.3787	50.94223	
Si4C2	71.98264	70.74533	68.37053	66.15466	64.07502	62.15092	60.35617	58.659	56.95638	55.16858	53.18647	
Si4C3	66.02523	65.13608	63.43653	61.84063	60.32385	58.87982	57.47874	56.07217	54.57375	52.90121	50.9693	
Si4C4	48.18373	48.43491	48.84173	49.11645	49.24816	49.19666	48.93268	48.41716	47.58828	46.39158	44.7779	
Si4C5	40.86502	41.34863	42.13305	42.68827	43.02937	43.16292	43.1018	42.86872	42.48207	41.96562	41.35796	
Si4C6	26.37223	26.7154	28.63795	30.33524	31.80603	32.9969	33.8737	34.40199	37.12107	34.3056	33.62474	

Table 7 : Tabulated values for the thermal conductivity, for 55mm diameter

LABEL	TEMPERATURE											THERMAL CONDUCTIVITY
	25	50	100	150	200	250	300	350	400	450	500	
Si4C1	82.86908	82.06779	80.84021	79.98731	79.39205	79.00513	78.78621	78.73617	78.86513	79.24523	79.96609	
Si4C2	70.24712	68.55474	65.43523	62.63099	60.09085	57.85906	55.96092	54.45159	53.3565	52.76164	52.74122	
Si4C3	62.12326	61.17963	59.43134	57.82685	56.32154	54.92514	53.63068	52.45101	51.37374	50.42552	49.63775	
Si4C4	49.33479	49.2151	49.04108	48.92639	48.84533	48.78802	48.73332	48.66559	48.569	48.42882	48.23552	
Si4C5	52.83019	53.81066	55.68153	57.41878	58.91383	60.16724	61.05206	61.4826	61.35806	60.55351	54.14484	
Si4C6	35.40386	36.1195	37.49385	38.77315	39.95066	40.97302	41.79781	42.37361	42.65647	42.58058	42.08916	

Table 8 : Tabulated values for the thermal conductivity, for 80mm diameter

Composition	sample no.	Tensile strength(Mpa)	Mean Tensile strength (Mpa)	Std Dev
Si4C1	6	113.2025192	113.1510899	0.282411
	1	113.4042517		
	2	112.8464988		
Si4C2	2	130.4216107	129.5092529	4.861161
	4	133.8495929		
	5	124.2565551		
Si4C3	2	160.7313549	166.7712191	7.531746
	3	175.2103045		
	4	164.371998		
Si4C4	1	203.434498	203.9595881	6.662736
	2	197.5749337		
	3	210.8693324		
Si4C5	1	232.7776693	232.9515577	9.009523
	2	242.0467665		
	3	224.0302373		
Si4C6	2	235.9521665	242.4817467	11.13675
	3	255.3408384		
	6	236.1522352		

Table 9 : Tabulated values for the Tensile strength, for 30mm diameter

Composition	sample no.	Tensile strength(Mpa)	Mean Tensile strength (Mpa)	Std Dev
Si4C1	1	104.1959364	103.2180715	1.158611648
	2	101.938433		
	5	103.5198451		
Si4C2	2	90.78939409	90.90145282	1.365025429
	5	89.59591083		
	6	92.31905354		
Si4C3	1	151.5080967	147.168816	3.771041813
	2	144.6849493		
	3	145.3134019		
Si4C4	1	181.4327775	188.056498	7.940559994
	2	196.8590083		
	3	185.8777082		
Si4C5	1	202.3180881	201.2847403	4.5821971
	2	196.2741066		
	3	205.2620262		
Si4C6	2	211.0686126	223.9292716	18.18771838
	6	236.7899306		

Table 10 : Tabulated values for the Tensile strength, for 55mm diameter

Composition	sample number	Tensile strength(Mpa)	Mean Tensile strength (Mpa)	Std Dev
Si4C1	3	99.84436487	99.45795959	0.744396704
	4	99.92969654		
	5	98.59981735		
Si4C2	1	86.96774472	82.49517623	6.915123284
	2	85.98741958		
	3	74.53036439		
Si4C3	1	116.8792318	119.5380739	2.30334805
	2	120.8097783		
	4	120.9252116		
Si4C4	1	136.1117736	133.1239663	2.604210058
	2	131.3356719		
	4	131.9244535		
Si4C5	1	153.082411	151.8132535	4.546742216
	2	155.5905671		
	3	146.7667824		
Si4C6	2	141.6504506	145.382654	12.14064344
	3	135.5476165		
	6	158.9522208		

Table 11 : Tabulated values for the Tensile strength, for 80mm diameter

Casting Diameter	Compositions	Type of Graphite Morphology
30mm	Si4C3	Type C
	Si4C4	Type E
	Si4C5	Type E
	Si4C6	Type D
55mm	Si4C1	Type C
	Si4C3	Type A
	Si4C4	Type E
	Si4C6	Type D
80mm	Si4C1	Type C
	Si4C3	Type C
	Si4C4	Type E
	Si4C5	Type E
	Si4C6	Type D

Table 12 : Type of graphite morphology formed in casts of all three cooling conditions